Impact Resistance of Masonry Walls:

Materials Characterisation
&
Numerical Modelling

Steven Burnett

Department of Civil and Structural Engineering

University of Sheffield

A thesis submitted to The University of Sheffield in partial fulfilment of
the requirements for the degree of Doctor of Philosophy

October 2003

Abstract

Structural masonry may often be required to resist out-of-plane dynamic loading. This loading may have been applied using an explosive means (e.g. a bomb blast or gas explosion) or, in the case of a masonry parapet, by a vehicle impact. So far, the dynamic response of masonry materials and structures has received little attention in the literature. The aim of the work described in this thesis is to: (i) investigate the dynamic tensile bond characteristics of masonry and (ii) develop a finite element methodology to investigate the response of masonry walls subject to out-of-plane car-like impacts.

A series of laboratory tests on masonry joints subject to dynamic tensile loading have been carried out using specially designed Split Hopkinson Pressure Bar apparatus. Results showed an apparent dynamic enhancement when specimens were loaded at strain rates of approximately 1 s^{-1}. Finite element modelling has been used to support a conjecture that this effect is probably caused by the inherent variability at the brick-mortar interface and is not a genuine material characteristic *per se*.

A masonry specific interface model suitable for modelling both brickwork and blockwork walls has been implemented in LS-DYNA, a three-dimensional non-linear explicit finite element program. The model was validated against results from a series of unreinforced walls tested previously in the laboratory. Results showed the proposed modelling strategy was in general able to predict the dynamic response of full-scale masonry walls with reasonable accuracy. However, a parametric study showed wall response was highly dependent on small changes in loading impulse, base friction, fracture energy, joint failure stress and angle of dilatancy.

The masonry specific interface model was also used to simulate the behaviour of reinforced walls. Results showed that the model was able to predict the correct failure mode and approximate peak displacement for some but not all of the walls. Furthermore, the model correctly predicted that the inclusion of diagonal bar reinforcement in a weakly mortared wall prevented punching failure behind the point of impact.

Acknowledgements

Throughout the duration of the project many people have been provided assistance and given advice, both technical and otherwise. Without these people the project would not have been a success. The author would like to thank all concerned but particular thanks must go to: Dr Matthew Gilbert for supervising the work and providing assistance with the development of this thesis; Dr Andy Tyas for advice on the Split Hopkinson Pressure Bar apparatus and interpretation of results; all technical support staff in the Department of Civil and Structural Engineering for constructing the large Split Hopkinson Pressure Bars; Dr Alan Cartledge and Peter Froggatt for invaluable computing support.

The author would also like to thank collaborators at Liverpool University, Dr Tom Molyneaux and Dr Greg Beattie, for advice and support throughout the project.

Finally, the author would like to acknowledge his family and friends for all their support and encouragement over the past four years.

Table of Contents

Chapter One: Introduction

Page

Chapter Two: Introduction to the Split Hopkinson Pressure Bar

Chapter Three: The response of masonry joints to dynamic tensile loading

Chapter Four: Numerical modelling of unreinforced masonry walls subject to out-of-plane car-like impacts

Chapter Five: Reinforced masonry walls subject to out-of-plane car-like impacts: experiments and numerical modelling

Chapter Six: Discussion, conclusions and recommendations

List of Figures

List of Tables

Chapter One

Introduction

1.1 Background

The road and rail networks across the UK intersect at many locations. Road/rail intersections may take the form of tunnels, level crossings or bridges. Even though modern bridges are constructed from concrete and steel there are thousands of masonry arch bridges with masonry parapets still in use today; some are of great historical importance. When these parapets were originally built they were designed to protect pedestrians and livestock from precipitous drops. However, with the rise of the motor vehicle in modern society, these parapets are now required to resist out-of-plane vehicular impact loading.

One of the main issues affecting bridge owners is whether or not existing parapets are able to resist vehicular impact loading. Until recently, design codes only covered metal or reinforced parapets, so it was extremely difficult for practising engineers to assess the performance of masonry parapets. If all the masonry parapets in the UK were replaced, the cost has been estimated to exceed £1.5 billion (at c.1993 prices). Clearly this is not a cost effective option because some masonry parapets might be able to resist vehicular impact loading. Hence, the question arises: in order to make effective use of financial resources, how can an engineer assess an existing masonry parapet to determine whether or not strengthening work is required?

The answer to the question lies in research. The County Surveyors Society (CSS) in the UK funded a series of actual parapet impact tests on a range of unreinforced masonry walls. The tests showed that many walls were able to resist vehicle impact loading at speeds up to 70 mph but there was a high risk of bricks being ejected from the wall.

In addition to the work carried out by the CSS a number of unreinforced walls were tested under laboratory conditions at Teesside University to study the different failure modes resulting from out-of-plane impact loading. This work formed part a collaborative project also involving Sheffield, Liverpool and Salford Universities entitled 'Impact Resistance of Masonry Walls'.

Initial work at Liverpool University was partly successful in modelling the response of walls to actual car impacts. The responses of the modelled walls were in good agreement with the observed responses of walls tested experimentally providing the masonry joint tensile and shear properties were increased well above quasi-static values. In addition to the modelling work, small-scale material tests showed that the properties of masonry joints were highly rate dependent. For example, under dynamic loading conditions, shear bond strength could increase by a factor of 3 compared with the quasi-static value. However, only a limited number of tests took place and thus no firm conclusions could be drawn.

At Sheffield University a mechanism analysis model was developed to simulate the response of unreinforced walls tested in the laboratory. The methodology was reasonably successful and simulated responses showed good agreement with experimental results. However, the model could not predict whether or not individual masonry units were likely to be ejected from a wall. Furthermore, the material properties used in the models were derived from a limited series of tests and consequently the results were inconclusive.

Subsequently finite element models were developed to simulate the response of the tested walls. However, a number of problems were found to exist:

(i) Insufficient computing power meant that only blockwork walls could be modelled (when explicitly modelling individual units).

(ii) Automatic allocation of interfaces between adjacent elements led to uneven distributions of bond strength, an issue which was unresolved at the time.

(iii) Treatment of friction was not robust.

Knowledge gained from the university research project and work carried out by the CSS assisted with the development of BS 6779 pt 4 (1999): 'Highway parapets for bridges and other structures'. Results indicated that many existing unreinforced walls were likely to be capable of resisting car impacts. However, this was not the case for all walls tested. Hence attention turned to identifying methods of upgrading parapet walls by introducing reinforcement.

The work presented in this thesis aims to build on work conducted as part of the previous collaborative project. The current work has been carried out in collaboration with the Universities of Liverpool and Teesside. The research areas for the current project have been organised to reflect the expertise and facilities that the three universities gained as a result of the original project. An interaction diagram detailing the current organisational structure is shown in Figure 1-1.

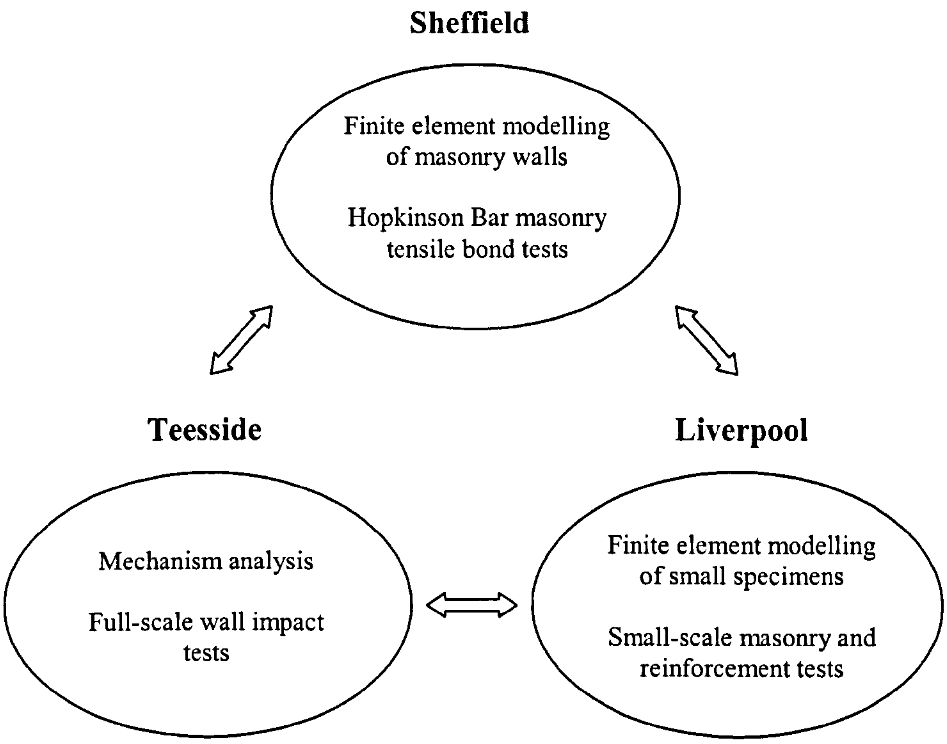

Figure 1-1 Schematic of principal tasks

1.2 Aims of the collaborative project

The main aim of the current collaborative project was to develop an understanding of the response of masonry walls to 'car-like' impact loading. Furthermore, previous work carried out at Liverpool University and Sheffield University highlighted a lack of knowledge on the dynamic properties of masonry materials. Therefore, an additional aim was to investigate the mechanical properties and rate sensitivity of the unit-mortar bond. In order to achieve the overall aims, each university was allocated specific objectives.

1.3 Sheffield objectives

The main research objectives of the work described in this thesis were to:

(i) Investigate the dynamic tensile bond characteristics of masonry using a Split Hopkinson Pressure Bar technique.

(ii) Develop a finite element methodology to investigate the response of masonry walls subject to out-of-plane car-like impacts.

1.4 Liverpool objectives

(i) Develop small-scale test methods in order to provide dynamic and quasi-static data required for the finite element modelling.

(ii) Test and analyse small-scale models.

1.5 Teesside objectives

(i) Test full-scale reinforced and unreinforced masonry walls subject to localised out-of-plane dynamic loads with similar characteristics to those resulting from accidental car impacts.

(ii) Develop mechanism analysis work from previous collaborative EPSRC research project.

1.6 Explanation of objectives

In order to gain an understanding of the response of masonry walls to 'car-like' impact loading it was necessary to carry out both experimental and numerical work.

Experimental work was divided into full-scale and small-scale testing work. The full-scale work was carried out at Teesside University and focussed on testing masonry walls subject to out-of-plane 'car-like' impacts. The aim of the test programme was to develop novel reinforcement strategies to improve the performance of unreinforced masonry walls. This involved testing walls with bed-joint reinforcement, diagonal bar reinforcement, vertical supports and weak mortar.

Small-scale work focussed on testing masonry specimens subject to dynamic tension and shear. Dynamic tension tests were carried out at Sheffield University using a specially designed Split Hopkinson Pressure Bar rig. Dynamic shear tests were carried out at Liverpool University using triplet specimens. In both cases, the post-peak failure behaviour was fully recorded. Additional tests were performed at Liverpool to determine the coefficient of sliding friction, angle of dilatancy and quasi-static shear and tensile failure stress.

At Sheffield University, data from the small-scale tests were used to develop a masonry specific joint interface model in LS-DYNA, a non-linear explicit finite element program. The modelling strategy was validated against the triplet specimens tested at Liverpool and later used to simulate the full-scale walls tested at Teesside. Further analyses of the full-scale wall tests were carried out at Teesside using an updated version of the mechanism analysis tool developed during the previous collaborative EPSRC research project.

1.7 Sheffield scope of work

In order to achieve the first Sheffield objective, a Split Hopkinson Pressure Bar was specially designed. Over a period of 18 months one of the largest test rigs of its kind was constructed in the Department's dynamics laboratory. This thesis describes the development of the test apparatus and presents results from a series of tests on masonry joints subject to dynamic tensile loading. The specific aim of the work was to record the complete stress-strain response of a joint and to investigate whether or not dynamic enhancement exists when masonry joints are subject to increased rates of strain.

The second Sheffield objective was achieved by implementing a masonry specific joint interface model in LS-DYNA, a three dimensional non-linear finite element program. Chapter Four describes the development and application of the modelling strategy. The specific aim of the work was to investigate the dynamic response of unreinforced masonry walls tested during the previous collaborative project and to explore the feasibility of using the modelling strategy to simulate the response of reinforced walls.

1.8 Arrangement of thesis

The thesis is organised into six main chapters. Chapter Two has been written as an extended introduction to the materials characterisation work. In particular, Chapter Two introduces the Split Hopkinson Pressure Bar apparatus to the reader and gives a detailed account of the design process for the Sheffield apparatus. Chapters Three, Four and Five form the main body of the thesis. These chapters have been written as three self contained papers which means there is some intentional overlap in the text.

Chapter Three presents results from a series of laboratory tests on masonry joints subject to dynamic tensile loading. Chapter Four describes the development and application of a material model suitable for modelling the behaviour of unreinforced masonry walls subject to out-of-plane impacts. Chapter Five presents results from a series of full-scale laboratory tests on reinforced masonry walls subject to out-of-plane impacts and applies the modelling strategy proposed in Chapter Four to reinforced walls. Finally, Chapter Six discusses the application of the results presented in Chapters Three, Four and Five and offers recommendations for future work.

Chapter Two

Introduction to the Split Hopkinson Pressure Bar

2.1 Introduction

This chapter has been written as an extended introduction to Chapter 3: The response of masonry joints to dynamic tensile loading. The aim of the chapter is to introduce the reader to dynamic testing by describing the development of a Split Hopkinson Pressure Bar that has been used to investigate the dynamic tensile properties of masonry joints.

The Hopkinson Bar was originally invented by Bertram Hopkinson to study the shapes of pressure waves resulting from the detonation of explosives or impact of bullets at one end of a long rod (Hopkinson 1914). The technique was used in its original configuration primarily to study the dynamic properties of steels in compression up until the end of the Second World War. Davies (1948) continued to work with the Hopkinson Bar and formulated a method to measure the displacement at the end of the bar using a parallel plate condenser. The plates behaved like a microphone enabling the output to be amplified to obtain the displacement history at the end of the bar. Assuming the bar remained elastic the stress-strain profile could be determined.

Kolsky (1949) modified the original Hopkinson Bar by adding another bar with the specimen sandwiched between the two ends. The experimental apparatus then became known as the Kolsky Bar or Split Hopkinson Pressure Bar (SHPB). Kolsky made use of Davies' (1948) analysis to obtain the stress-strain histories in both bars. These could then be combined with one dimensional wave propagation theory to establish the stress-strain history in the specimen.

During the 1960s the development of SHPB continued through work by Harding *et al.* (1960) and Lindholm & Yeakley (1968) who modified the bar in order to subject specimens to tension. Further modifications by Baker & Yew (1966) allowed torsion to be applied to the specimen. Through these important developments the Hopkinson Bar technique could now be used to subject specimens to compression, tension and shear.

2.2 Stored energy bar

2.2.1 Introduction

The SHPB is normally used to apply compression, tension and shear at strain rates between 1 and 10000 s^{-1} compared with quasi-static loading rates of 10^{-3} s^{-1}. These strain rates originally resulted from a pressure wave excited by an explosive means that had the advantage of producing a pulse with a shorter rise time and reasonably constant amplitude (Hopkinson 1914).

More recently the stress wave has been initiated by a striker bar fired from an airgun (e.g. Diamaruya *et al.* 1997) or, as shown in Figure 2-1, applying a stored energy technique to the input bar (Nicholas & Lawson 1971, Hartley & Duffy 1985, Rajagopalan *et al.* 1999). The stored energy approach to dynamic testing is particularly useful because it has the potential for tension, compression and torque to be applied to the bar simultaneously i.e. a combined stress state can be achieved.

In addition to the application of combined stress states, the stored energy technique also allows stress to be applied either dynamically or statically. For example, static pre-compression may be applied prior to a dynamic shear stress (Espinosa *et al.* 2000). This is particularly advantageous when testing frictional materials such as masonry because it is often useful to be able to simulate static loading that results from the self-weight of a structure in addition to the application of a dynamic load. However, in order to achieve the objectives set out in the introduction we shall only consider the application of a stored dynamic tensile pulse.

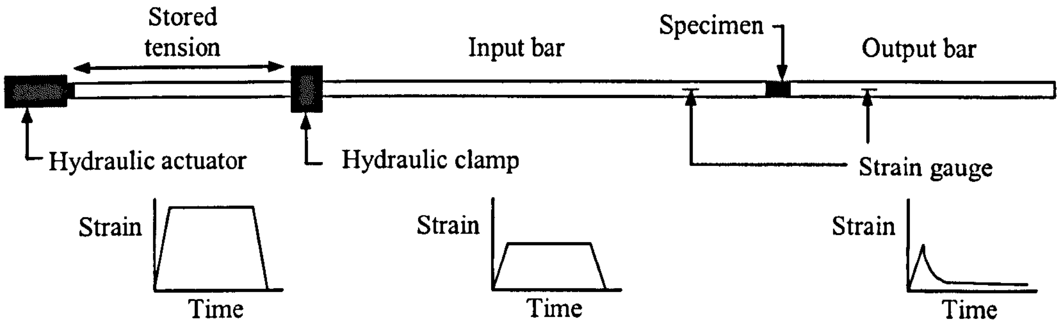

Figure 2-1 Split Hopkinson Pressure Bar (schematic)

2.2.2 Mode of operation

For dynamic tensile loading, a clamp is attached to the input bar and a hydraulic actuator is used to exert a tensile force on one end of the bar. The clamp is released rapidly enabling a stress pulse, with a constant amplitude equal to half that of the stored tension, to travel along the input bar until it reaches the bar-specimen interface (Figure 2-2). At the same time, an unloading pulse of equal magnitude propagates from the clamp toward the hydraulic actuator. The mechanical impedance of the actuator is such that the wave will be reflected back into the input bar.

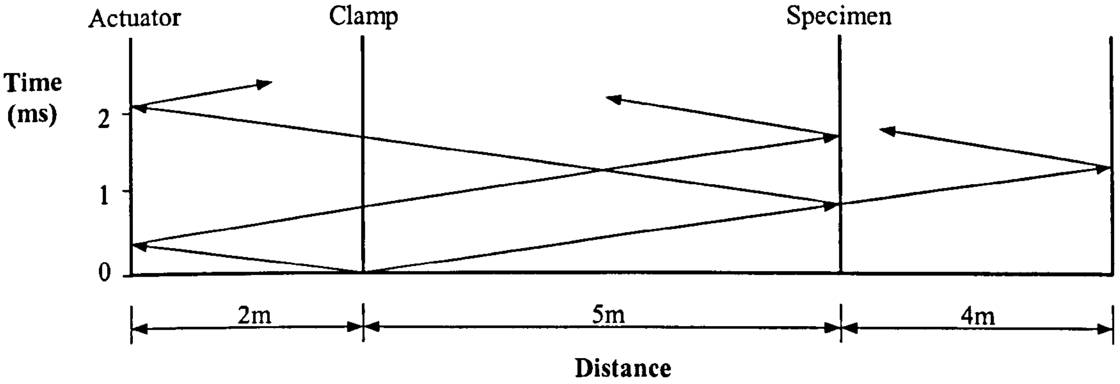

Figure 2-2 Distance vs time diagram for a longitudinal wave propagating in the pressure bar shown in Figure 2-1

When the pulse reaches the front face of the specimen it is partly reflected back into the input bar and partly transmitted into the output bar. The stress pulse travelling in the output bar continues as a tensile pulse but the reflected pulse returns as a compressive pulse. Two strain gauge stations record the strain histories in the two bars and the data is then analysed using a desktop computer. To enable the analysis by Davies (1948) to apply it is essential that both bars remain elastic throughout the duration of the experiment.

2.2.3 Maximum/minimum strain rate

The range of strain rates that can be obtained by a stored energy bar primarily depend on the magnitude of the stored wave and the length of the specimen. The lowest strain rate that is able to fracture a specimen is limited by the duration of the stored input wave i.e. twice the distance between the clamp and the fixed end. The highest strain rate depends on the maximum stress that can be stored whilst the bar continues to remain elastic and the minimum specimen length.

2.2.4 Existing clamp mechanisms

The origins of the stored energy bar can be traced back to the mid 1960's when Baker & Yew (1966) devised a hydraulic clamp that was positioned on the input bar in order to store a torsion wave (Figure 2-3). This was achieved by firstly applying the clamp to the input bar and then turning the free end through a small angle. Whilst the input bar was being loading it was important that the clamp did not slip and the bar remained elastic. A torsion wave was generated by the rapid release of the pre-twisted bar. The rapid release mechanism operated by punching out a steel plate with a slug fired from an airgun.

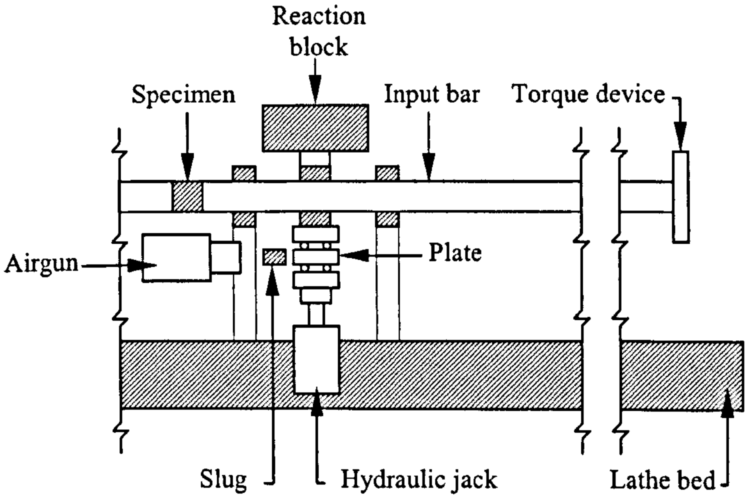

Figure 2-3 Torsional Split Hopkinson Bar showing hydraulic clamp (Baker & Yew 1966)

This release mechanism allowed a torsion wave to propagate along the input bar with a rise time of 30 μs for a stored shear stress of 200 N/mm^2. The clamp arrangement could be used to subject specimens to shear strain rates up to 2100 s^{-1}. As with all stored energy bars, the strain rate could be increased by decreasing the thickness of the specimen and increasing the yield stress of the input bar.

The clamp used by Baker & Yew (1966) may have been experimentally successful but the health and safety requirements for a modern laboratory may not be suited to a rapid release mechanism that is operated by firing a high velocity slug from an airgun. Nicholas & Lawson (1971) approached this problem by employing a clamp mechanism that was operated purely by a hydraulic actuator. Once again, the clamp was positioned on the input bar and attached to a hydraulic actuator by a short length of notched steel rod (Figure 2-4).

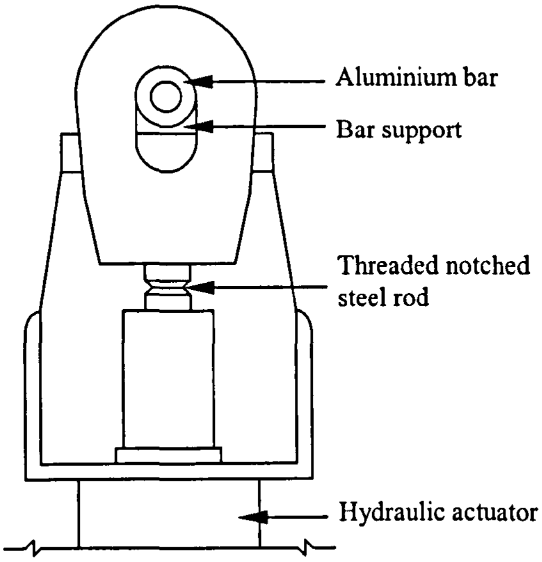

Figure 2-4 Hydraulic clamp detail (Nicholas & Lawson 1971)

A torsion wave was stored in the input bar by firstly exerting a clamping force and then applying a small rotation. The release mechanism operated by increasing the clamping force until the notched steel rod failed. The clamp was able to produce a pulse with a rise-time of approximately 40 μs. Nicholas and Lawson (1971) concluded that the test apparatus was reliable when aluminium specimens were subject to strain rates between

100 s^{-1} and 10000 s^{-1}. The notched rod hydraulic clamp also proved to be a suitable mechanism for releasing a stored incident wave.

Over the past 30 years the hydraulic clamp employed by Nicholas and Lawson (1971) has been modified by a number of researchers (Hartley & Duffy 1985, Rajagopalan *et al.* 1999, Feng & Ramesh 1993, Rajagopalan & Prakash 1999, Chichili & Ramesh 1999) to study shear strain rate effects in a wide range of engineering materials. However, most researchers have continued to use a clamping mechanism that was released by fracturing a notched bolt or threaded rod.

Hartley & Duffy (1985) used a notched rod hydraulic clamp to release a torsion wave. The main difference between their design and the one used by Nicholas and Lawson (1971) was that the incident bar was clamped horizontally instead of vertically (Figure 2-5). This had the advantage of reducing bending effects in the bar before the clamping mechanism was released. The clamp consisted of two vertical arms that were in contact with the aluminium bar. A hydraulic actuator pushing horizontally against one of the vertical arms applied the clamping force. Again, the clamp was released by continuing to increase the clamping force until a notched rod fractured.

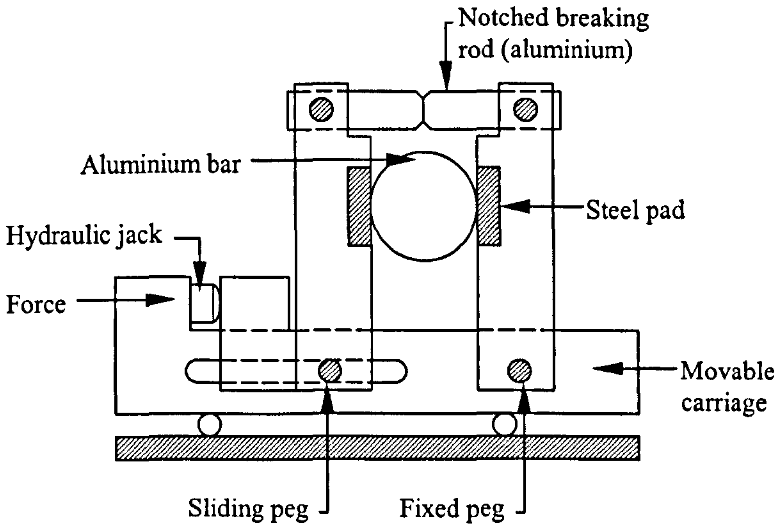

Figure 2-5 Hydraulic clamp detail (Hartley & Duffy 1985)

So far, it has been demonstrated that the stored energy bar has successfully been used to apply dynamic shear loading to a specimen. However, the same principles can be applied to dynamic tensile loading. Section 2.3 describes the design philosophy behind the Split Hopkinson Pressure Bar apparatus used to test masonry specimens subject to dynamic tensile load.

2.3 Design of a stored energy Split Hopkinson Pressure Bar

2.3.1 Determine input and output bar dimensions

The first step in the design process is to choose a suitable material and diameter for the input and output bars. The exact choice of pressure bar material depends on the highest stress needed to fracture a specimen and the minimum value of strain that can accurately be measured in the bar. For example, to fracture a specimen that has a relatively high yield stress (e.g. aluminium) requires a bar with a greater yield stress than the specimen (e.g. steel).

For materials that fracture at much lower yield stresses i.e. brick-mortar specimens, it is useful to select a bar with a relatively low elastic modulus. Therefore, aluminium has been chosen for the input and output bars. This is advantageous because small specimen strains equate to much larger bar strains in aluminium compared to say, steel. Therefore, when data are recorded, the signal to noise ratio will be improved by a factor of 3.

The exact choice of bar diameter is arbitrary. However, the diameter should be large enough to accurately represent the properties of the test specimen. Therefore, the bar diameter should be at least 50 mm to reduce the effects of localised specimen imperfections (Albertini & Montagnani 1994, Cadoni *et al.* 2001, Lok *et al.* 2002). For the present study, the diameter of the input and output bars was 101.6 mm.

The next step in the design process is to determine the length of the input and output bars by firstly calculating the impedance change at the interface between the specimen and the input bar (Figure 2-6).

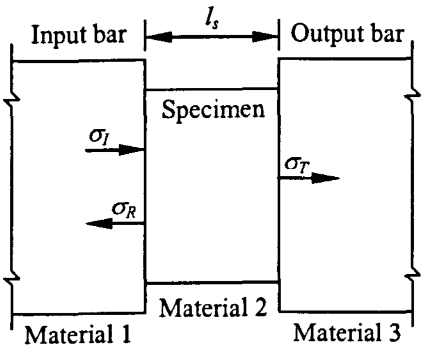

σ_I = Incident stress
σ_R = Reflected stress
σ_T = Transmitted stress
c = Wave speed
A = Area of cross-section
l_s = Specimen length
E = Elastic modulus (bar)

Figure 2-6 Bar-specimen interface

An incident wave travels along the input bar until it reaches the specimen-bar interface. At this point part of the incident wave is reflected back into the input bar and part of the wave is transmitted into the output bar. The ratio between incident and transmitted components is calculated from the relative density, wave speed and cross sectional area of the two materials either side of the interface:

$$\sigma_R = \frac{\rho_2 c_2 A_2 - \rho_1 c_1 A_1}{\rho_2 c_2 A_2 + \rho_1 c_1 A_1}\sigma_I \tag{2-1}$$

$$\sigma_T = \frac{2\rho_2 c_2 A_1}{\rho_2 c_2 A_2 + \rho_1 c_1 A_1}\sigma_I \tag{2-2}$$

Table 2-1 Typical material properties for aluminium and masonry

	Density ρ (kg/m^3)	Wave speed c (m/s)	Cross-sectional area A (mm^2)
Aluminium (101.6mm diameter bar)	2700	5092	8107
Masonry (100mm diameter specimen)	1850	3200	7854

Substituting values from Table 2-1 into (2-1) and (2-2) gives:

$$\sigma_R = -0.4\sigma_I \tag{2-3}$$

$$\sigma_T = 0.6\sigma_I \tag{2-4}$$

If it is assumed that the tensile stress in a masonry joint at failure will be similar to the quasi-static failure stress reported by Rots (1997) and Pluijm (1997) i.e. approximately 1 N/mm^2, the elastic modulus of masonry and aluminium is approximately 20 kN/mm^2 (Beattie 2003) and 70 kN/mm^2 respectively, then the stress in the output bar will also be approximately 1 N/mm^2. Therefore, according to (2-3) and (2-4), the incident and reflected stress will be approximately 1.7 N/mm^2 and 0.7 N/mm^2 respectively. Substituting the reflected stress, σ_R in (2-5) and using a specimen with a length of 50 mm gives a strain rate $\dot{\varepsilon}$ of 2 s^{-1}.

$$\dot{\varepsilon} = \frac{2c\sigma_R}{l_s E}$$

(2-5)

Work by Pluijm (1997) showed that the strain in a masonry joint at peak failure was approximately 100 μstrain (Figure 2-7). Furthermore, Pluijm also showed that the strain at the end of the post-peak softening branch was approximately 2000 μstrain. Therefore, substituting strain and strain rate into Equation 2-6 gives a wavelength l_w of 0.25 m i.e. the wavelength required to reach peak failure.

$$l_w = \frac{\varepsilon_s c}{\dot{\varepsilon}}$$

(2-6)

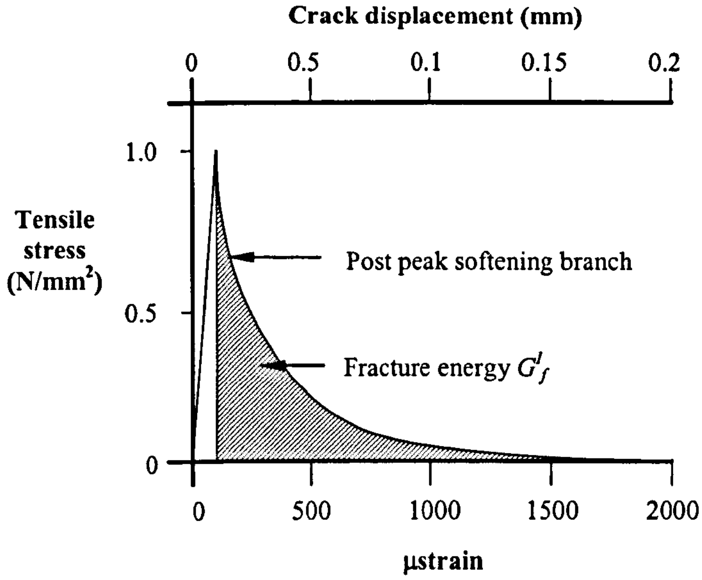

Figure 2-7 Typical behaviour of a masonry joint under tensile loading and definition of fracture energy

If the post-peak strain is equal to 2000 μstrain and the residual post-peak stress is approximately 0.1 N/mm^2 the reflected stress will increase to 1.6 N/mm^2 and the strain rate will increase to 5 s^{-1}. This means that the wavelength required to strain the specimen from 100 μstrain to 2000 μstrain equates to 1.9 m. Hence, the total wavelength needed to fail the specimen is approximately 0.25 + 1.9 = 2.15 m i.e. the specimen will reach the end of the softening branch after 0.00042 seconds.

Now that we know the wavelength required to fracture the specimen, the next step is to calculate the optimum position from which to release the wave. When a tensile wave propagates along the bar, it is likely that flexural waves will also be present. This presents a potential problem because the specimen could fail in bending instead of tension. However, flexural waves propagate more slowly than tensile waves. Therefore, a tensile wave will always precede the arrival of any flexural waves.

As we know that the specimen will take approximately 0.00042 seconds to fail, we can calculate optimum position from which to release the wave if we can predict the velocity of longitudinal and flexural waves. The velocity of a longitudinal wave is given by:

$$c = \sqrt{\frac{E}{\rho}}$$

(2-7)

Where c is the longitudinal wave speed in the bar, E is elastic modulus and ρ is density. If we assume that the elastic modulus and density of the bar are 70000 N/mm^2 and 2700 kg respectively the longitudinal wave speed is approximately 5092 m/s.

The longitudinal velocity of flexural waves varies according to the wavelength. As we do not know the exact wavelength because it will be a function of the release mechanism, we must assume a worst-case scenario. According to Davies (1948) the maximum velocity of a flexural wave occurs when the ratio between the bar radius and wavelength (a/l) is equal to about 0.3. This in turn gives a ratio between longitudinal wave speed and flexural wave speed of approximately 0.64. As we have already calculated the longitudinal wave speed to be 5092 m/s it follows that the maximum flexural wave speed is approximately 0.64 × 5092 = 3259 m/s.

For the specimen to fail in tension the time between the arrival of the front of the tensile wave and arrival of the front of the flexural wave must be at least 0.00042 seconds. If we let x represent the distance between the clamp and the specimen and the flexural and longitudinal wave speeds to be c_f and c respectively we can show:

$$\frac{x}{c_f} - \frac{x}{c} \geq 0.00042$$

(2-8)

Substituting $c_f = 3259$ m/s and $c = 5092$ m/s in (2-8) we find that the distance between the clamp and the specimen should be at least 3.8 m. As we are designing a stored energy bar the distance between the clamp and hydraulic actuator needs to be at least equal to half the length of the loading wave. Therefore, the total length of the input bar should be at least (0.5 × 1.9) + 3.8 = 4.75 m.

The output bar needs to be long enough to allow the transmitted wave to be fully recorded before it is overwritten by its own reflection. If we assume that the transmitted wave is fully recorded by strain gauges positioned 1m away from the specimen the minimum output bar length should be half the input wavelength plus the distance between the strain gauges and specimen i.e. (0.5 × 1.9) + 1 = 1.95 m.

The optimum position for strain gauges on the input bar is also 1m away from the specimen. However, positioning the gauges 1m away from the specimen only allows us to read the first 2 m of the input wave before it is overwritten. Therefore, a small amount of data manipulation may be required to determine the complete stress-strain history in the specimen.

From the above calculations it was decided to construct a SHPB rig with an input and output bar length of approximately 7 m and 4 m respectively. The diameter of both bars was 101.6 mm.

2.3.2 Choice of strain gauges

The stress-strain history of a specimen is determined from strain gauges attached to the input and output bars. Strain gauges can be divided into two main types:

(i) Conventional electrical resistance
(ii) Semiconductor

One of the main differences between the two types of strain gauge is the gauge factor. The gauge factor controls the change in output voltage for a given change in strain. For conventional gauges the gauge factor is typically around 2 but semiconductor gauges have much higher gauge factors in the region of 100-250. This means that semiconductor gauges are more sensitive to changes in strain than conventional gauges. High sensitivity is particularly important in the current work because the strain in the bar will be no more than 14 μstrain if a specimen fails at approximately 1 N/mm^2.

Another difference between the two types of strain gauges is linearity. For semiconductor gauges, the strain-voltage relationship is non-linear. If the gauges are significantly non-linear a calibration factor needs to be applied to the results. However, if the change in strain is small the gauges may be assumed to be linear for a small change in voltage.

The non-linearity of four semi-conductor gauges was investigated by loading the input bar over 5 N/mm^2. Gauges were positioned at quarter points around the perimeter and voltage readings were taken every 0.25 N/mm^2 (Figure 2-8).

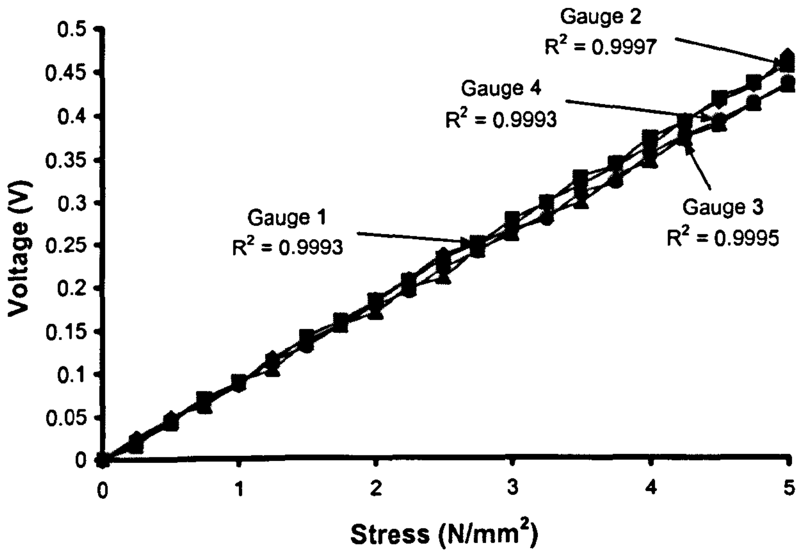

Figure 2-8 Investigation of voltage output for four semi-conductor gauges

The R^2 values in Figure 2-8 show how closely the data fits a linear trend line. The closer the value is to 1 the more linear the data set. Therefore, it may be concluded that semiconductor gauges have a near linear response when the bar is loaded up to 5 N/mm^2.

Figure 2-8 has shown that semiconductor gauges can accurately record the stress-strain history in the input and output bars. However, it is important to ensure that the results are not affected by the gauge length. For example, if the gauge length is similar to the wavelength of a pulse frequency resolution will be lost. Therefore, it is advantageous to use a small gauge length.

In section 2.3.1 the wavelength required to fail a brick-mortar specimen was found to be approximately 2.15 m. This implies that no resolution will be lost if the gauge length is of the order of a few millimetres. Therefore, it was decided to use semiconductor gauges with an active gauge length of 5 mm.

2.3.3 Sampling data

The first stage in designing an efficient data acquisition system is to make sure the strain gauges are wired correctly to give the desired output. As it is important to ensure that the specimen is subject to pure tension prior to peak failure, gauges mounted on opposite sides of the bar need to be monitored individually. Therefore, all strain gauges were wired as a quarter bridge (Figure 2-9).

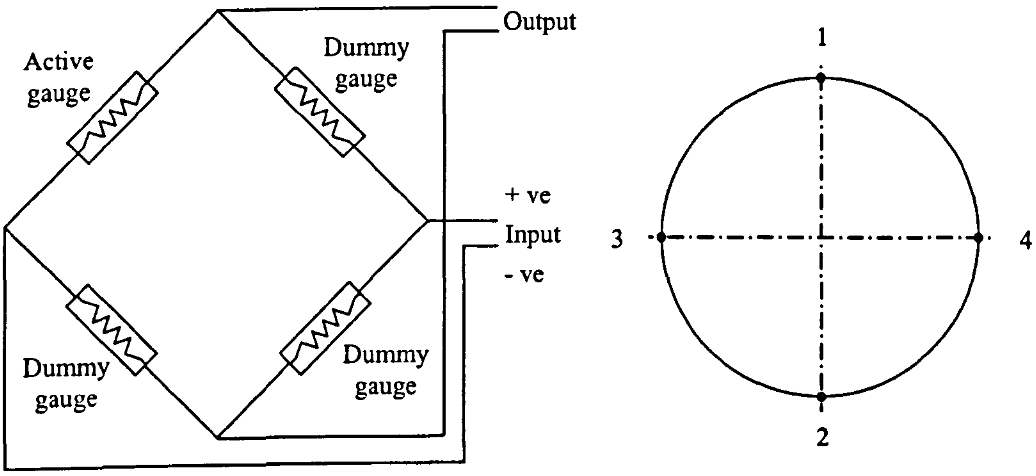

Figure 2-9 Wheatstone bridge (left) and bar cross section showing position of strain gauges (right)

The change in voltage across the Wheatstone bridge is given by:

$$\Delta V_{out} = \frac{K\sigma V_{in}}{4E} \tag{2-9}$$

Where ΔV_{out} is the change in voltage output, V_{in} is the voltage input, K is the gauge factor, E is the elastic modulus of the bar and σ is the stress in the bar.

Assuming the failure stress recorded in the output bar is 1 N/mm^2, the gauge factor is 168, the input voltage is 10 V and the elastic modulus of the bar is 70 kN/mm^2, the change in output voltage will be 6 mV. As the specimen is loaded dynamically the change in voltage will occur over a very short period of time. Therefore, a computer controlled data acquisition board is needed to sample the data.

Data acquisition boards receive a continuous analogue input signal that has to be discretized in the time and voltage domain. As it is impossible to sample continuously it is important to ensure that the sample rate is fast enough to capture the data. Assuming the fracturing process takes approximately 0.00042 seconds and 1000 data points are required in the time domain the analogue signal will have to be sampled at least 2 million times per second i.e. 2 MHz.

Sampling in the voltage domain depends on the resolution of the board (i.e. 10 bit, 12 bit etc). If a board has a 12 bit resolution it simply means that it will take 2^{12} samples over the input voltage range. In order to get the highest resolution from the data acquisition board the input voltage should be no more than ±1 V. However, we have calculated the voltage change to be just 6 mV. Therefore, if we use a 12 bit board to sample the data there will be just 12 data points in the voltage domain. This is clearly unacceptable so the signal needs to be amplified.

In a quasi-static problem amplifier performance is not usually an issue providing the quality of the signal is acceptable. However, in a dynamic problem it is essential to ensure that the amplifier can process the signal at a fast enough rate. (2-6) showed that the specimen reached peak failure in approximately 50 μs. Therefore, the amplifier should have a minimum bandwidth of 100 kHz.

From the above calculations it was decided to sample the analogue signal using Fylde amplifiers (minimum bandwidth 100 kHz) and a 12 bit data acquisition board (Adlink NuDAQ PCI-9812).

2.3.4 Signal processing: wave dispersion in a cylindrical bar

Once the data acquisition hardware has converted the raw analogue signal into a digital signal it can then be analysed on a desktop computer. Before any analysis is performed it is often useful to make a correction for wave dispersion. However, in the present study, it is not strictly necessary to apply a correction because most of the energy in the loading pulse is transmitted at frequencies that are not significantly dispersive i.e. the ratio between bar radius and wavelength (a/l) is much smaller than unity (see Chapter 3, Figure 3-8). Therefore, the correction procedure applied to the experimental results reported in Chapter 3 has been included for completeness rather than necessity.

When an elastic wave propagates along a cylindrical bar it will become distorted due to dispersive effects caused by the variation of phase velocity with wavelength (Follansbee & Frantz 1983). This results in the high frequency components of the wave travelling more slowly than low frequency components.

The amount of dispersion depends on the geometric relationship between the length of the wave and the diameter of the bar. When a wavelength approaches the bar diameter dispersion filters out certain frequency components and distorts the stress pulse. As a result, the stress pulse derived from strain gauges placed on the surface of the input and output bars will not be the same as the stress pulse at the specimen.

In some instances dispersion may be advantageous because it has the effect of smoothing out a stress pulse. For example, if a noisy stress wave was released by a clamping mechanism, dispersion causes the pulse to become much smoother as it travels along the input bar. This may result in a more constant amplitude and hence strain rate in the specimen.

In recent years, it has become common practice to account for the effects of wave dispersion by applying a correction to the phase angle of each Fourier component (Gorham 1983, Follansbee & Frantz 1983). The Fourier Transform is calculated by multiplying the original signal by a sine wave that has a constant amplitude and frequency. The result is integrated to give the Fourier component at that particular frequency and amplitude. For example, suppose we have an input signal in the form of a sine wave like the one shown in Figure 2-10.

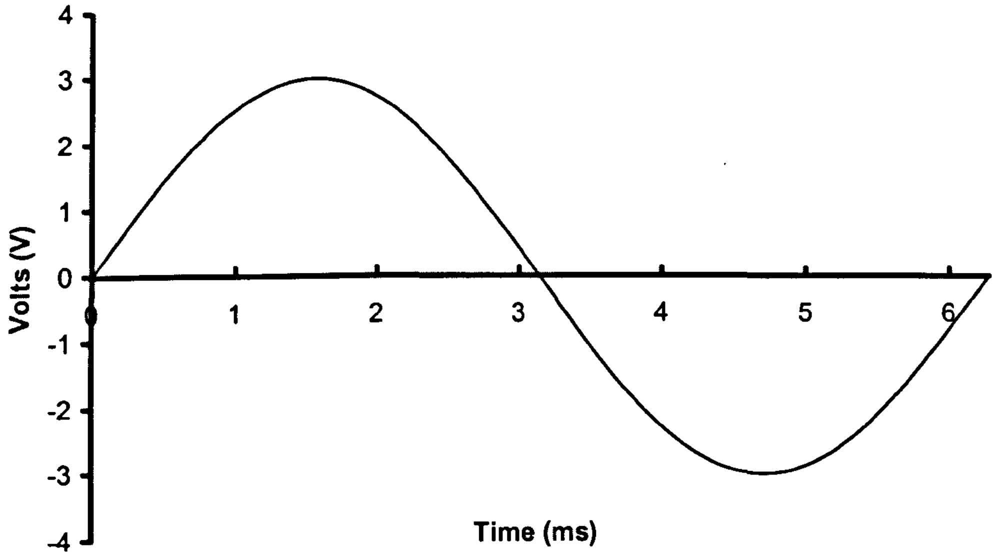

Figure 2-10 Wave prior to dispersion correction

The sine wave in Figure 2-10 is multiplied by a second sine wave with unit amplitude and frequency 159.2 kHz (Figure 2-11).

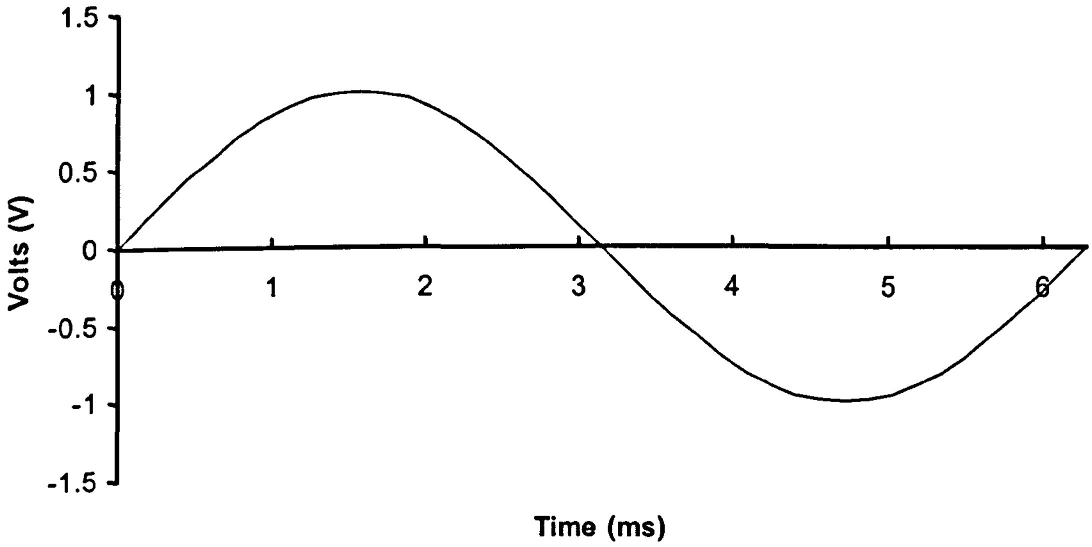

Figure 2-11 Sine wave with unit amplitude and frequency 159.2 kHz

The result is shown in Figure 2-12.

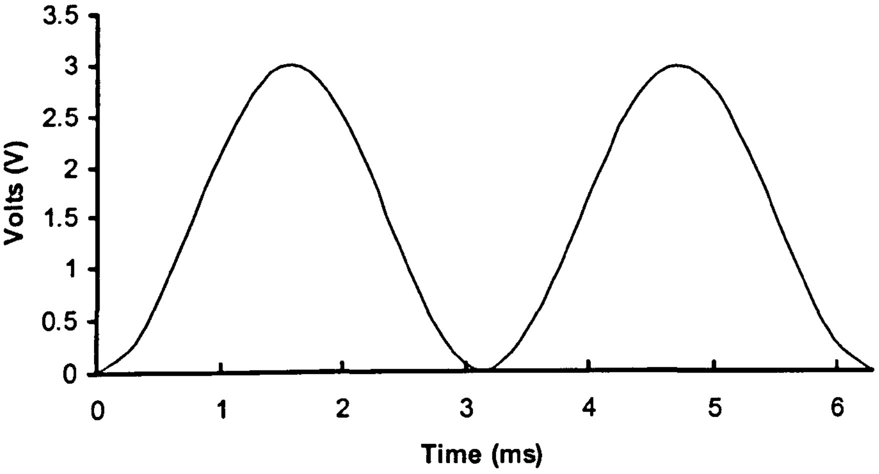

Figure 2-12 Result of multiplying original sine wave by unit sine wave

Integrating the result shown in Figure 2-12 and dividing by the total signal duration (6.28 ms) gives a value of 1.5 Volts. This value is the amplitude of the Fourier Transform at a frequency of 159.2 kHz and is equal to half the amplitude of the original sine wave (Figure 2-13).

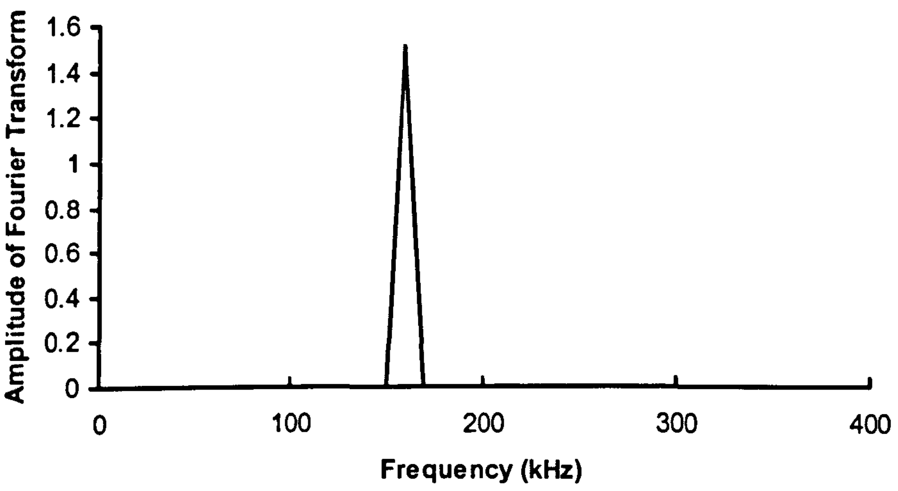

Figure 2-13 Frequency analysis of a sine wave showing amplitude of Fourier Transform at different frequencies

As the sine wave is a trivial case the amplitude of the Fourier Transform at any other frequency is always zero (Figure 2-13). However, for waves that comprise a spectrum of frequencies there will be a corresponding number of Fourier Transform amplitudes.

The method outlined above to calculate the Fourier Transform amplitude holds true if the signal is in phase. However, if the signal is out of phase we also need to repeat the procedure by integrating and multiplying by a unit cosine wave. Then, if the amplitude derived by multiplying the original signal by a unit sine wave is A_{sin} and the amplitude derived by multiplying the original signal by a unit cosine wave is A_{cos} the correct amplitude $A_{correct}$ is given by:

$$A_{correct} = \sqrt{A_{\sin}^2 + A_{\cos}^2} \tag{2-10}$$

Once the signal has been converted to the frequency domain a phase shift is applied by calculating the phase angle ϕ_ω and phase velocity c_ω for each frequency component. The phase angle is simply the arctan of the ratio of the two amplitude components, A_{sin} and A_{cos}.

$$\phi_\omega = \tan^{-1}\left(\frac{A_{\cos}}{A_{\sin}}\right) \tag{2-11}$$

Phase velocity c_w is calculated from the wavelength l and frequency ω of each Fourier component, the longitudinal wave speed c and radius of the pressure bar a:

$$\frac{c}{c_\omega} = \frac{\left(\frac{a}{l}\right)}{\left(\frac{2\pi\omega a}{c}\right)} \tag{2-12}$$

The next step is to derive the phase shift between the point at which the signal was recorded and the bar-specimen interface (distance z) for each frequency component. The phase shift ϕ'_ω is given by:

$$\phi'_\omega = \left(\frac{c}{c_\omega} - 1\right)\frac{\omega z}{c}$$

(2-13)

Classical Pochammer-Chree wave theory suggests that the axial strain across the cross-section of a bar is not uniform. Therefore, in an extreme case, it is possible to record a stress wave that is opposite in sign to the true stress wave. This phenomenon can occur because strain gauges attached to the perimeter of a bar only record surface strain which is not necessarily representative of the strain in the bar cross-section.

The accuracy of the phase shift can be improved by multiplying each frequency component by a factor to allow for the difference between the axial strain measured at the surface of the bar and the average axial stress over the cross-section calculated from theory. Full details of the correction procedure are given by Tyas & Watson (2000). Once all of the amplitudes and phase angles have been corrected the wave can be converted back into the time domain for further analysis.

$$\phi_{corrected\ \omega} = \phi_\omega - \phi'_\omega$$

(2-14)

2.4 References

Albertini C, Montagnani M (1994); Study of the true stress-strain diagram of plain concrete with real size aggregate; need for and design of a large Hopkinson bar bundle; Journal de Physique IV, Colloque C8, 113-118.

Baker WE, Yew CH (1966); Strain-Rate Effects in the Propagation of Torsional Plastic Waves; Journal of Applied Mechanics, Vol. 33, pp 917-923.

Beattie (2003); Joint fracture in reinforced and unreinforced masonry under quasi-static and dynamic loading; PhD thesis submitted to Liverpool University, UK.

Cadoni E, Labibes K, Berra M, Giangrasso M, Albertini C (2001); Influence of Aggregate Size on Strain-Rate Tensile Behaviour of Concrete; ACI Materials Journal, Vol. 98, 220-223.

Chichili DR, Ramesh KT (1999); Recovery Experiments for Adiabatic Shear Localization: A Novel Experimental Technique; Journal of Applied Mechanics, Vol. 66, pp 10-20.

Davies RM (1948); A Critical Study of the Hopkinson Pressure Bar; Philosophical Transactions of the Royal Society of London A, Vol. 240, pp 375-457.

Diamaruya M, Kobayashi H, Nonaka T (1997); Impact tensile strength and fracture of concrete; Journal de Physique IV, Colloque C3, pp 253-258.

Espinosa HD, Patanella AJ, Fischer M (2000); Dynamic Friction Measurements at Sliding Velocities Representative of High-Speed Machining Processes; Journal of Tribology, 122, 834-848.

Feng R, Ramesh KT (1993); The Rheology of Lubricants at High Shear Rates; Journal of Tribology, Vol. 115, pp 640-647.

Follansbee PS, Frantz C (1983); Wave Propagation in the Split Hopkinson Pressure Bar; Journal of Engineering Materials and Technology, Vol. 105, pp 61-66.

Gorham DA (1983); A numerical method for the correction of dispersion in pressure bar signals; Journal of Physics E: Scientific Instruments, Vol. 16, pp 477-479.

Harding J, Wood EO, Campbell JD (1960); Tensile Testing of Materials at Impact Rates of Strain; Journal Mechanical Engineering Science, Vol. 2, pp 88-96.

Hartley KA, Duffy J, Hawley RH (1985); The Torsional Kolsky (Split Hopkinson) Bar, Metals Handbook 9th edition, Vol. 8, pp 218-228.

Hopkinson B (1914); A method of measuring the pressure produced in the detonation of high explosives or by the impact of bullets; Philosophical Transactions of the Royal Society of London A, Vol. 213, pp 437-456.

Kolsky H (1949); An investigation of the mechanical properties of materials at very high rates of loading; Proceedings of the Physics Society of London B, Vol. 62, pp 676-700.

Lindholm US, Yeakley LM (1968); High Strain-Rate Testing: Tension and Compression; Experimental Mechanics, Vol. 8, pp 1-9.

Lok TS, Li XB, Liu D, Zhao PJ (2002); Testing and Response of Large Diameter Brittle Materials Subjected to High Strain Rate; Journal of Materials in Civil Engineering, May/June, 262-269.

Nicholas T, Lawson JE (1971); On the determination of the mechanical properties of materials at high shear-strain rates; Journal of Mechanics, Physics and Solids, Vol. 20, pp 57-64.

Pluijm van der R (1997); Non-Linear Behaviour of Masonry Under Tension; Heron, Vol. 42, pp 25-54.

Rajagopalan S, Prakash V (1999); A modified torsional Kolsky bar for investigating dynamic friction; Experimental Mechanics, Vol. 39, pp 295-303.

Rots JG (1997); Structural Masonry: An Experimental/Numerical Basis for Practical Design Rules; AA Balkema, Rotterdam, ISBN 90 5410 680 8.

Tyas A, Watson A (2000); Experimental Evidence of Pochammer-Chree Strain Variations in Elastic Cylinders; Experimental Mechanics, Sept, pp 331-337.

Chapter Three

The response of masonry joints to dynamic tensile loading

Summary

This chapter presents results from a series of laboratory tests on masonry joints subject to dynamic tensile loading. The tests were carried out using specially designed Split Hopkinson Pressure Bar apparatus. The chapter describes the development of the test apparatus and discusses how the results can be used in numerical models.

Results showed an apparent dynamic enhancement when specimens were loaded at strain rates of approximately 1 s^{-1}. Finite element modelling has been used to support a conjecture that this effect is probably caused by the inherent variability at the brick-mortar interface and is not a genuine material characteristic *per se*.

3.1 Introduction

In the last 10 years, masonry researchers have focused on the quasi-static behaviour of the brick-mortar interface (Rots 1997, Pluijm 1997) because it has been shown to have a significant influence on the overall behaviour of many types of structures. This is apparent when a structure is subject to both quasi-static and dynamic impact loads (Gilbert *et al.* 2002).

At present, there are virtually no data on the dynamic properties of masonry materials. However, the dynamic response of other structural materials, such as steel and concrete, has received much more attention. For example, it has been widely reported that concrete, subject to dynamic tension, appears to exhibit a 'dynamic enhancement' as strain rates approach 1 s^{-1} (Malvar & Ross 1998). Therefore, the question arises: how do masonry joints respond to an increase in loading rate?

In recent years, it has become common practice to use a Split Hopkinson Pressure Bar to investigate the dynamic response of many different types of materials. Originally invented by Bertram Hopkinson to study the shapes of pressure waves in long cylindrical bars (Hopkinson 1914), Davies (1948) continued to develop the apparatus and formulated a method to measure the displacement-time history at the end of a bar. Assuming the bar remained elastic the stress-strain profile could be determined. Kolsky (1949) then modified the original Hopkinson Bar by adding another bar with a material specimen sandwiched between the two ends. The experimental apparatus then became known as the Kolsky Bar or Split Hopkinson Pressure Bar (SHPB). Kolsky made use of Davies' (1948) analysis to obtain the stress-strain histories in both bars. These could then be combined with one dimensional wave propagation theory to establish the stress-strain history in the specimen.

This chapter presents results from a series of laboratory tests on masonry joints subject to dynamic tensile loading. The aim of the work is to characterise the complete stress-strain response of a masonry joint and determine whether or not a dynamic enhancement exists. The tests were carried out using a specially designed Split Hopkinson Pressure Bar. The chapter describes the development of the test apparatus and discusses the application of the results to numerical modelling.

3.2 Post-peak tensile behaviour of quasi-brittle materials

At present, there is little information on the dynamic response of masonry joints in the literature. However, there is a limited amount of data on the quasi-static behaviour of masonry joints (Rots 1997, Pluijm 1997) and the dynamic response of other quasi-brittle materials such as concrete and mortar (Zeilinski & Reinhardt 1982, Ross *et al.* 1989, Ross *et al.* 1995, Rossi *et al.* 1994, Rossi & Toutlemonde 1996, Diamaruya *et al.* 1997).

Rots (1997) and Pluijm (1997) showed that under quasi-static loading conditions the tensile strength of a masonry joint was in the region of 0.2-3.0 N/mm^2 depending on the class of mortar. However, perhaps more importantly, it was observed that masonry joints did not fail in a completely brittle manner but instead exhibited a post-peak softening branch (Figure 3-1).

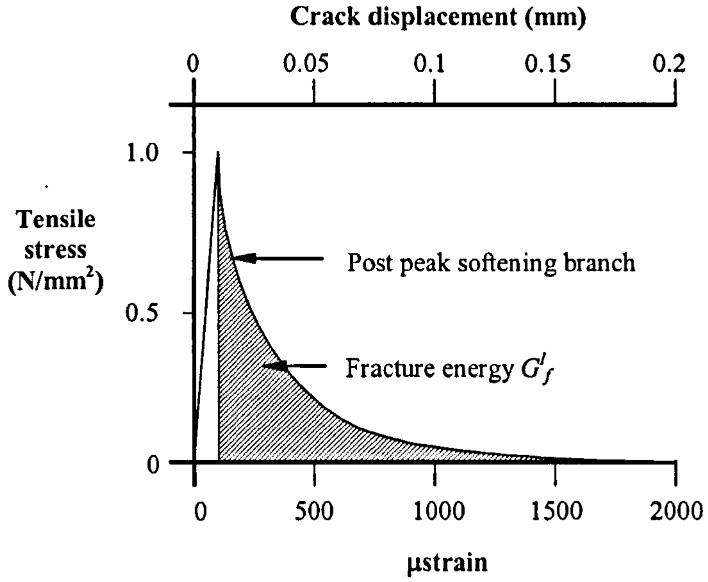

Figure 3-1 Typical behaviour of a masonry joint under tensile loading and definition of fracture energy

The amount of energy dissipated (due to the joint cracking) corresponds to the area under the tensile stress-crack displacement curve. This is termed mode I fracture energy G^I_f. It is known that the tensile strength of a quasi-brittle material is highly dependent on the fracturing process and the associated energy dissipation (Bažant & Kazemi 1990).

The post-peak response of a masonry joint subject to quasi-static tension is similar to that exhibited by concrete and mortar (Bažant & Kazemi 1990). However, whilst some researchers have used a Split Hopkinson Pressure Bar to investigate the response of concrete and mortar subject to dynamic tensile stresses, little effort has been made to characterise post-peak behaviour. Previous researchers have only considered linear elastic behaviour up to peak load and the effects of increasing strain rate (e.g. Zeilinski & Reinhardt 1982).

3.3 Stored energy Split Hopkinson Pressure Bar

3.3.1 Introduction

In most SHPB rigs, the stress pulse is generated by moving a striker bar which impacts the end of a bar. In a stored energy SHPB rig the stress pulse is generated by rapidly releasing a pre-stressed section of bar. The stored energy approach to dynamic testing is particularly useful because it has the potential for tension, compression and torque to be applied to the bar simultaneously i.e. a combined stress state can be achieved. Furthermore, it is also easier to generate a tensile pulse compared to the striker bar approach.

In addition to the application of combined stress states, the stored energy technique also allows stresses to be applied either dynamically or quasi-statically. For example, static pre-compression may be applied prior to a dynamic shear stress (Espinosa *et al.* 2000). This is particularly advantageous when testing frictional materials such as masonry because it is often useful to be able to simulate static loading that results from the self-weight of a structure in addition to the application of a dynamic load. However, for the purpose of this chapter we shall only consider the application of a stored dynamic tensile pulse.

3.3.2 Mode of operation

For dynamic tensile loading, a clamp is attached to the input bar and a hydraulic actuator is used to exert a tensile force on one end of the bar (Figure 3-2). The clamp is released rapidly enabling a stress pulse, with nominally constant amplitude equal to half that of the stored tension, to travel along the input bar until it reaches the bar-specimen interface. At the same time, an unloading pulse of equal magnitude propagates from the clamp toward the hydraulic actuator. The mechanical impedance of the actuator is such that the wave will be reflected back into the input bar.

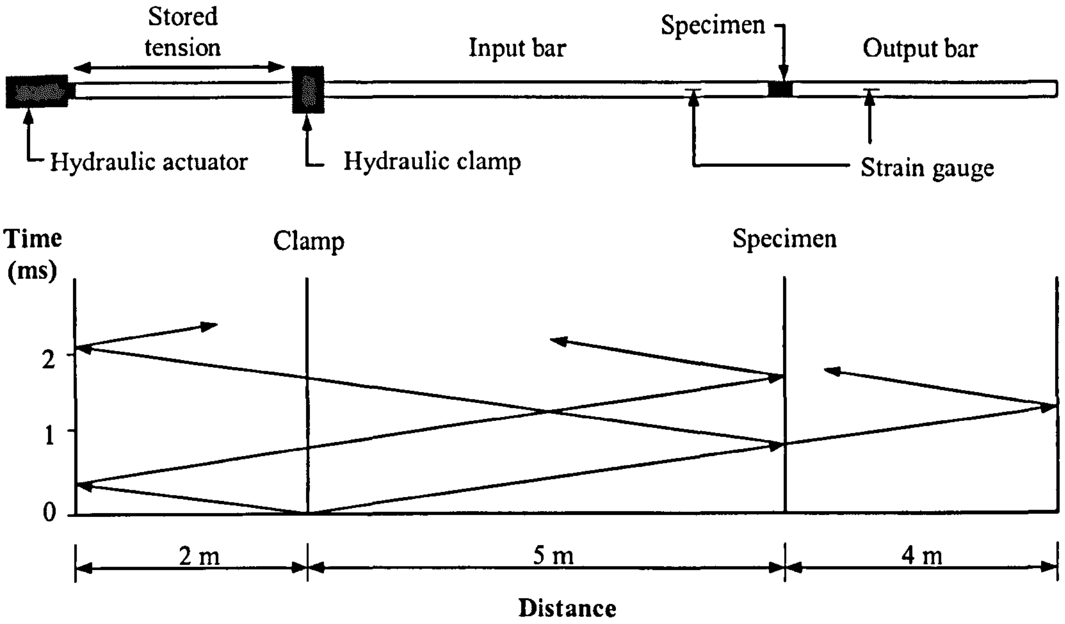

Figure 3-2 Top: Stored energy Split Hopkinson Pressure Bar (schematic) Bottom: Distance vs time diagram for a longitudinal wave propagating in a pressure bar

When the pulse reaches the front face of the specimen it is partly reflected back into the input bar and partly transmitted into the output bar. The stress pulse travelling in the output bar continues as a tensile pulse but the reflected pulse returns as a compressive pulse. Two strain gauge stations record the strain histories in the two bars and the data are then analysed using a desktop computer. It is evident from Figure 3-2 that the specimen receives the leading edge of the stress pulse at approximately 0.95 ms and that there is a further period of approximately 0.75 ms before the reflected wave from the actuator arrives. To enable the analysis by Davies (1948) to apply it is essential that both bars remain elastic throughout the duration of the experiment.

3.3.3 Maximum/minimum strain rate

The range of strain rates that can be obtained by a stored energy SHPB depends primarily on the magnitude of the stress in the stored wave and the length of the specimen. The lowest strain rate that is able to fracture a specimen is limited by the duration of the stored input wave i.e. twice the distance between the clamp and the fixed end. The highest strain rate depends on the maximum stress that can be stored whilst the bar continues to remain elastic and the minimum specimen length.

3.3.4 Length of input and output bars

The length of the input and output bars is dictated by the time needed to fail a specimen. For masonry joints, the test duration needs to be reasonably long (>300 μs) in order to record the peak failure stress and post-peak softening branch. Until recently, test duration was usually limited by the length of the input and output bars. However, advancements in wave separation techniques have significantly increased the theoretical test duration (Zhao & Gary 1997).

In practice, even though the theoretical test duration may be infinite, the useful test duration is often limited by the arrival of flexural waves at the specimen. This is particularly important because masonry has been shown to be highly sensitive to multi-axial loads (Syrmakezis & Asteris 2001). Therefore, it is essential that a test specimen has time to fail in tension before the arrival of a flexural wave.

Davies (1948) showed that longitudinal and flexural wave speed varied according to the ratio of bar radius to wavelength (a/l). If a/l is small (<0.2), longitudinal waves travel at a much higher velocity than flexural waves. Therefore, if the input bar is long, a longitudinal wave is released such that it will have time to become adequately separated from a flexural wave. Hence useful test duration is governed by the distance between the bar-specimen interface and the point at which a longitudinal wave is released.

For the present study, after some analysis, it was concluded that the length of the input and output bars should be approximately 7 m and 4 m respectively. This configuration allows a pulse with a duration of 750 μs to be released 5 m from the specimen. If it is assumed that flexural waves propagate at their maximum velocity (≈64% of the longitudinal wave speed when a/l ≈ 0.3), the useful test duration is at least 635 μs.

3.3.5 Specimen dimensions

Since the Split Hopkinson bar was first introduced there has been some debate about the choice of specimen dimensions. Kolsky (1949) stressed that the test was only valid if the thickness of the specimen is small compared to the shortest wavelength of the

Fourier spectrum of the pulse. More recently, it has been suggested that specimen dimensions may have an influence on dynamic enhancement (Gorham 1991, Dioh *et al.* 1993, 1995). However, few researchers have attempted to quantify this relationship and it seems that the precise choice of specimen dimensions is somewhat arbitrary. Therefore, it was decided to use specimens with length:diameter aspect ratios of 0.5 and 1.0.

3.3.6 Description of test set-up

The test rig designed comprised of a heavily reinforced concrete reaction beam supported by two short reinforced concrete columns (Figure 3-3). A double acting hydraulic actuator was attached to the concrete beam by means of a steel reaction frame. One end of the input bar was threaded and screwed into the actuator.

Brick-mortar-brick specimens were glued to the free end of the input bar. The opposite face of the specimen was glued to one end of the output bar. The free end of the output bar terminated at an end stop. The end stop was not directly connected to the output bar and was positioned purely for safety reasons.

The input and output bars were aligned along their longitudinal axes by carefully adjusting the bar supports. Both bars were manufactured from 6082-T6 aluminium and had a diameter of 101.6 mm.

The input and output bars were manufactured from aluminium in preference to steel because specimen strains equate to much larger bar strains. Therefore, the signal to noise ratio will be improved by a factor of 3. A large bar diameter was chosen to reduce the effects of localised specimen imperfections (Albertini & Montagnani 1994, Cadoni *et al.* 2001, Lok *et al.* 2002).

The clamp mechanism incorporated four 500 kN hydraulic actuators working in parallel (Figure 3-4). The actuators reacted between the steel beam and concrete beam above, transferring a downward force to the aluminium clamp head via two 28 mm diameter steel bars. The clamp released by continuing to apply pressure to the hydraulic actuators until a notched bolt failed in tension. The efficacy of various bolt materials were tested, including aluminium and mild steel, but high strength steel bar (yield stress ≈1000 N/mm^2) was found to provide the best response.

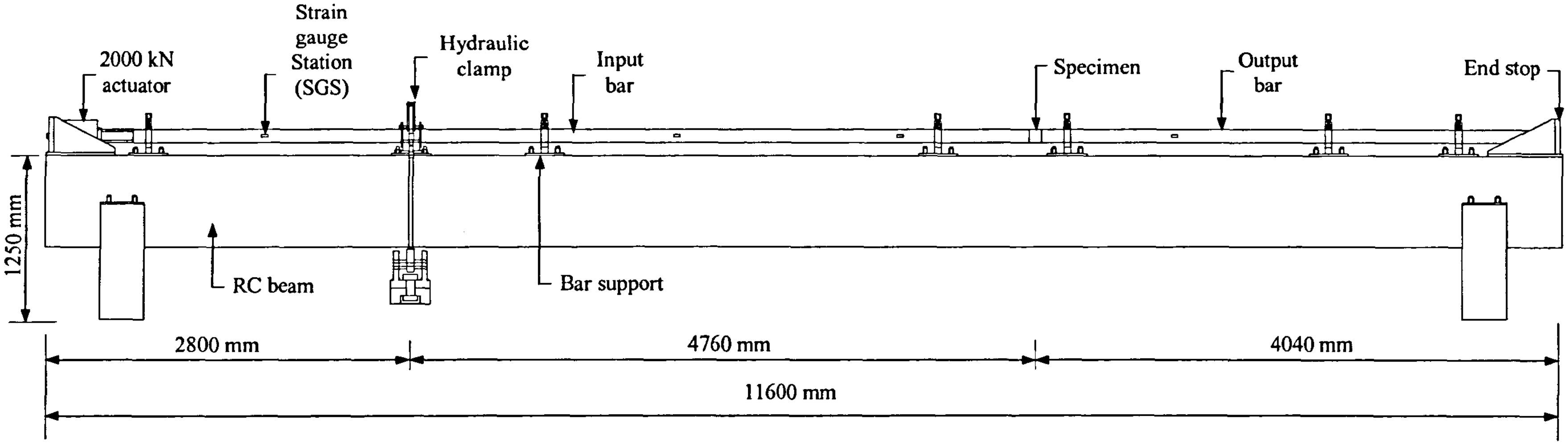

Elevation

Figure 3-3 General arrangement of test apparatus

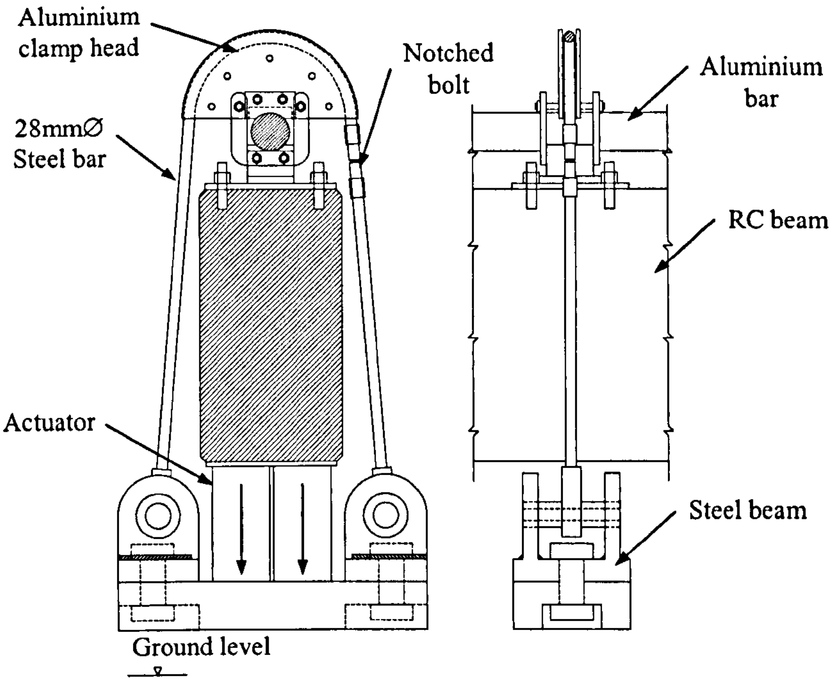

Figure 3-4 Detail showing hydraulic clamp mechanism

Data were recorded by two sets of semi-conductor strain gauges (Kyowa KSPH-4-2K-E4) positioned on the input and output bars 1m away from the specimen. The use of semi-conductor gauges allowed strain measurements to be resolved to approximately 0.1µstrain (equivalent to a stress of 0.007 N/mm^2). High sensitivity is particularly important in the present study because of the very low strengths of the masonry specimens being tested (approximately 0.2-3.0 N/mm^2).

Gauges were located at quarter points around the perimeter of each bar and connected to Fylde amplifiers (minimum bandwidth 100 kHz). Output was monitored by a high-speed PC-based data acquisition system (Adlink NuDAQ PCI-9812) with a minimum sampling rate of 2 MHz per channel.

3.3.7 Test specimens

Cylindrical specimens were prepared from Marshalls' solid red smooth Accrington Nori clay engineering bricks (class B). The bricks were cut, cored and ground smooth on one face to provide a high quality finish (within ±0.1 mm across the diameter). The other face of the brick was left in its initial condition. The cores were washed and brushed clean to remove any residue from the cutting process.

Two brick cores were bonded together with a class (iii) mortar to BS 5628(i) (1:1:6 cement:lime:sand) to make one specimen (Figure 3-5). The brick cores were carefully levelled and aligned to ensure that the two outer surfaces remained parallel (within ±0.1 mm across the diameter). A small compressive stress of 0.002 N/mm^2 was applied to the specimen to simulate the overpressure that would be present during the construction of a typical masonry wall. All specimens were cured under polythene for 24 hours and then in ambient laboratory conditions before being tested after a nominal 28 days.

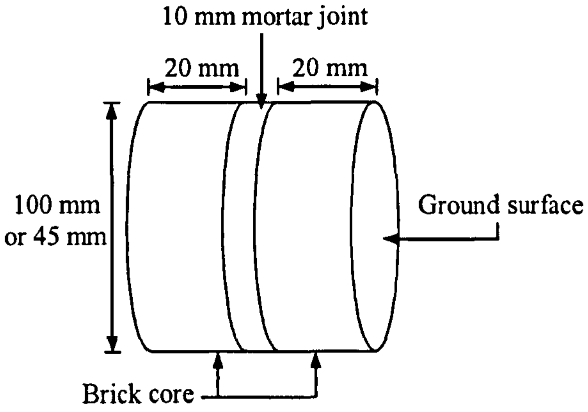

Figure 3-5 Brick-mortar-brick specimen

3.3.8 Dynamic test arrangement

The input and output bars were carefully aligned to ensure that the free ends were parallel. Displacement gauges were positioned at the free end of the input bar to monitor horizontal and vertical movement. The clamp was attached to the input bar and a hydraulic actuator exerted a tensile force on one end of the bar. A specimen was fixed into position between the input and output bars by a rapid hardening epoxy resin adhesive. To ensure a good acoustic connection at the specimen-bar interface a wedge was positioned between the output bar and end stop. After 1 hour, the wedge was removed and a tensile wave was released rapidly by continuing to apply pressure to the clamp until a notched steel bolt failed in tension.

3.3.9 Quasi-static test arrangement

In order to investigate whether or not a dynamic enhancement existed it was also necessary to test specimens quasi-statically. Therefore, specimens were tested in a quasi-static loading rig (Figure 3-6). Each specimen was bonded to a set of steel platens using a rapid hardening high strength epoxy resin adhesive. The platens were carefully aligned along their longitudinal axes to minimise eccentricity. The platens connected to the rig via two ball joints.

The specimen was loaded in quasi-static tension by turning a threaded steel rod. A pressure gauge mounted between the reaction plate and steel platen measured the stress in the specimen. Output was monitored using an ORION data logger sampling at a rate of 1 s^{-1}. As the aim of the quasi-static tests was to investigate whether or not a dynamic enhancement existed, no attempt was made to record post-peak behaviour.

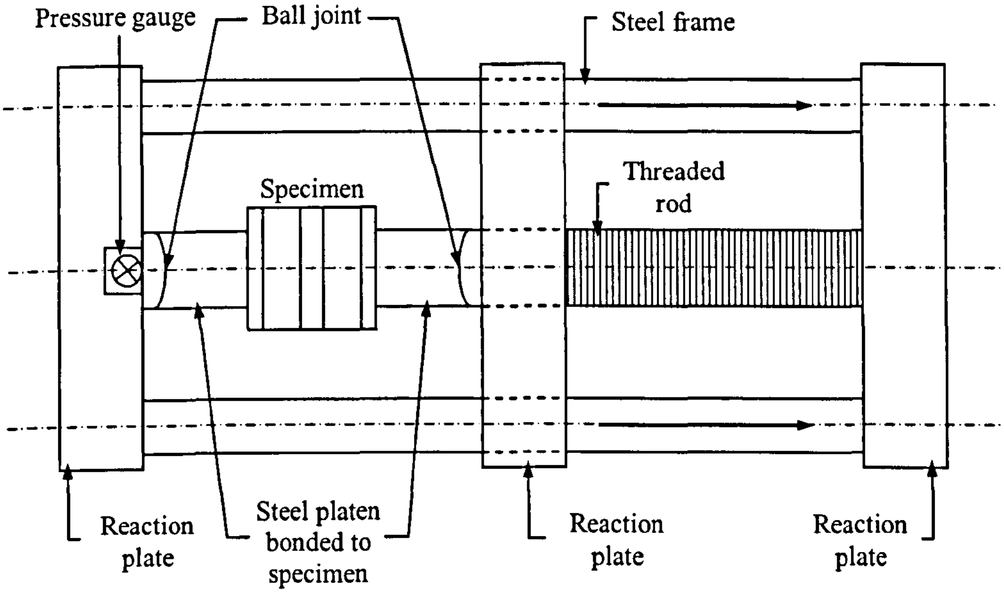

Figure 3-6 Elevation of quasi-static test rig

3.4 Experimental results

For all dynamic tests, an input wave with approximate duration of 750 μs and a peak stress of 3.5 N/mm^2 was used. Figure 3-7 shows the first 350 μs of an input and transmitted wave time shifted to the specimen. The average stress in the specimen is derived from the transmitted wave. Note that the specimen reaches peak failure as the input wave continues to rise. This means that the strain rate in the specimen is not constant. However, once the specimen starts to fail the strain rate will increase rapidly regardless of the nature of the input wave. Therefore, it is effectively impossible to test a quasi-brittle specimen to failure at a constant strain rate throughout.

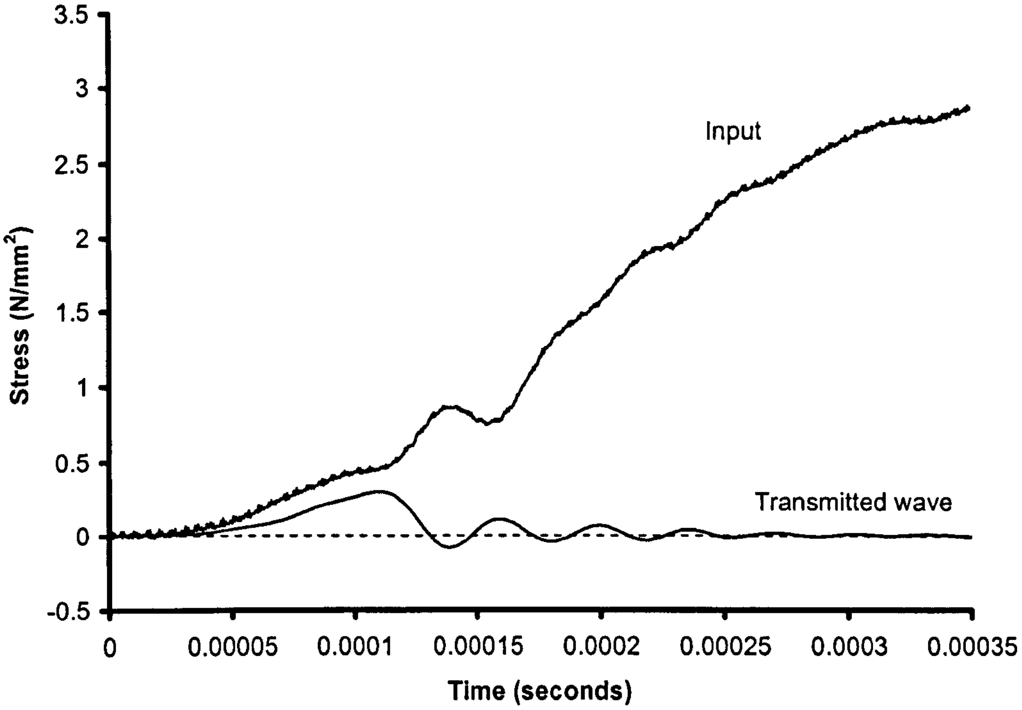

Figure 3-7 Example of a typical input and transmitted wave

Table 3-1 provides results from the dynamic tension tests. Table 3-2 provides results from the quasi-static load tests.

Table 3-1 Details of dynamic tests

Test Ref.	Nominal Specimen Size (Diameter × Length mm)	Batch	Age at Test (Days)	Strain Rate at Peak Stress (s^{-1})	Peak Failure Stress (N/mm^2)
1	45 × 50	1^{*}	28	1.32	0.8
4	100 × 50	1^{*}	33	1.00	2.12
5	45 × 50	2^{**}	33	1.45	1.61
7	100 × 50	2^{**}	34	0.89	1.85
8	100 × 50	3^{+}	34	1.52	1.17
9	45 × 50	3^{+}	34	1.12	1.72
11	45 × 50	2^{**}	37	1.44	1.50
13	45 × 50	2^{**}	58	0.96	1.70
Mean					1.56
Standard deviation					0.41
Coefficient of variation					0.26

Mortar cube strength to BS 5628 pt 3

* Batch 1 mean compressive strength = 13.1 N/mm^2

** Batch 2 mean compressive strength = 11.7 N/mm^2

$^{+}$ Batch 3 mean compressive strength = 12.1 N/mm^2

Table 3-2 Details of static tests

Test Ref.	Nominal Specimen Size (Diameter × Length mm)	Batch	Age at Test (Days)	Peak Failure Stress (N/mm^2)
3	100 × 50	1	30	0.70
6	100 × 50	2	33	0.62
10	100 × 50	3	34	0.32
12	100 × 50	3	57	0.48
14	45 × 50	2	83	0.38
15	45 × 50	2	83	0.56
Mean				0.51
Standard deviation				0.14
Coefficient of variation				0.27

3.5 Analysis of results

3.5.1 Correction for wave dispersion

A stress wave propagating in a pressure bar is composed of a spectrum of frequencies. If all frequency components travelled at the same velocity, the stress wave recorded at the gauge station would be the same as the stress wave recorded at the specimen. However, high frequency components travel more slowly than low frequency components. This has the effect of ‘smoothing out’ the wave as it travels along the bar. Therefore, the wave recorded at the gauge station may not be the same as the wave recorded at the specimen.

In recent years, it has become common practice to account for the effects of wave dispersion by applying a correction to the phase angle of each Fourier component (Gorham 1983, Follansbee & Frantz 1983). However, the correction approach assumes that the strain recorded at the perimeter of the bar is representative of the average strain in the bar cross-section. In practice, lateral inertia is not constant over the bar cross-section and elastic modulus varies with frequency and radial ordinate.

Tyas & Watson (2001) noted that dispersion affects the phase angle of the Fourier component whereas lateral inertia and non-uniform elastic modulus affect the amplitude of the Fourier component. Therefore, factors could be derived from Davies' (1948) analysis to correct the amplitude of the Fourier component.

Tyas & Watson (2001) give full details of the correction method but the procedure may be summarised as follows:

(i) Convert time-domain signal recorded in input and output bars into the frequency domain using a Fast Fourier Transform.

(ii) Calculate the phase angle, phase velocity and amplitude of each frequency component.

(iii) Apply a correction factor to the amplitude to correct for dispersion, lateral inertia and non-uniform elastic modulus.

(iv) Calculate the phase shift for each frequency component. In this case, the wave recorded in the output bar was shifted 1 m back towards the specimen.

(v) Convert the frequency domain signal back into the time domain using the corrected phase angle.

Figure 3-8 shows a stress wave from the output bar that has been converted into the frequency domain using a Fast Fourier Transform (taken from a 45 mm diameter specimen). Note that there is a sharp drop in the amplitude of the Fourier component at $a/l = 0.37$ as the strain at the bar perimeter falls to zero. This indicates that the pulse is likely to be dispersive.

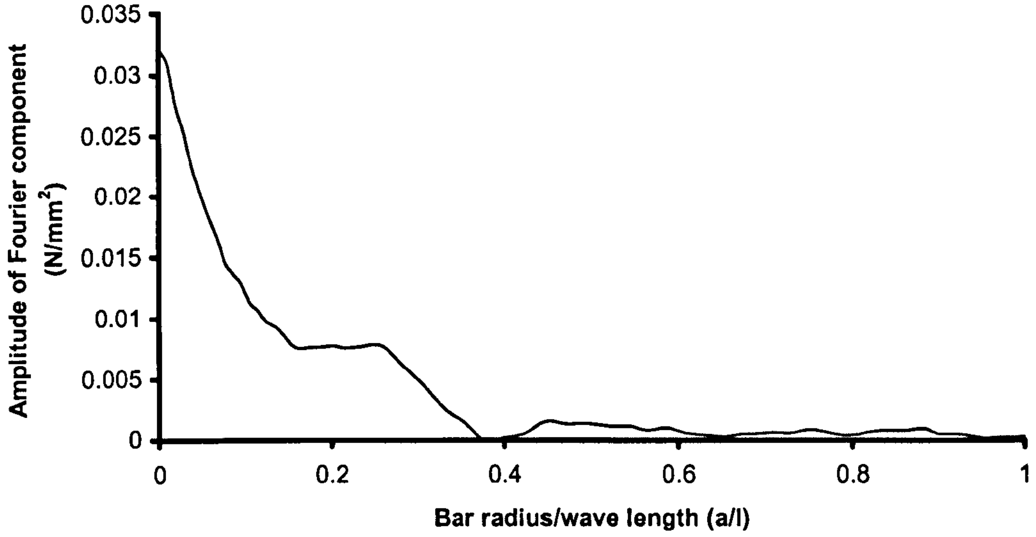

Figure 3-8 Example of a stress wave converted from the time domain into the frequency domain

Figure 3-9 shows the stress wave in Figure 3-8 both uncorrected and corrected for dispersion, lateral inertia and non-uniform elastic modulus. A phase shift has been applied to each frequency component such that the stress wave recorded in the output bar is now the same as the stress wave at the bar-specimen interface. Note that the corrected wave is generally much smoother and the peak stress is 11.2% higher than the uncorrected wave. The post-peak oscillations most likely result from stress waves oscillating in the output side of the specimen as the brick-mortar interface starts to fail.

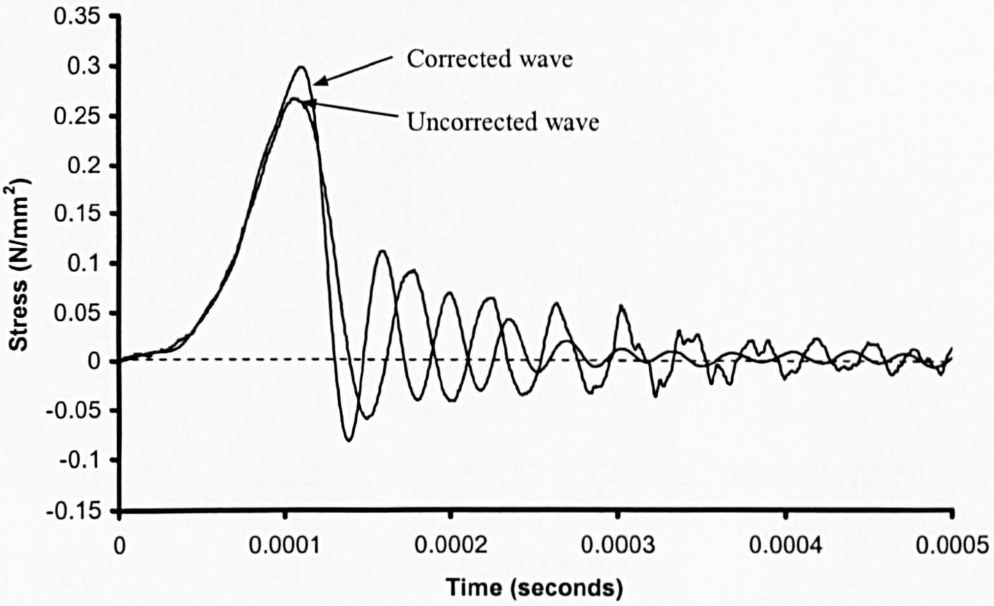

Figure 3-9 Example of a stress wave recorded in the output bar corrected for wave dispersion, lateral inertia and non-uniform elastic modulus

3.5.2 Stress-strain response of a specimen

The stress-strain response of a specimen can be obtained by applying one-dimensional wave propagation theory to the stress waves recorded in the input and output bars. Figure 3-10 shows a short specimen sandwiched between two cylindrical long bars. The displacement at the end of each bar can be written in terms of incident, transmitted and reflected strain (Davies 1948).

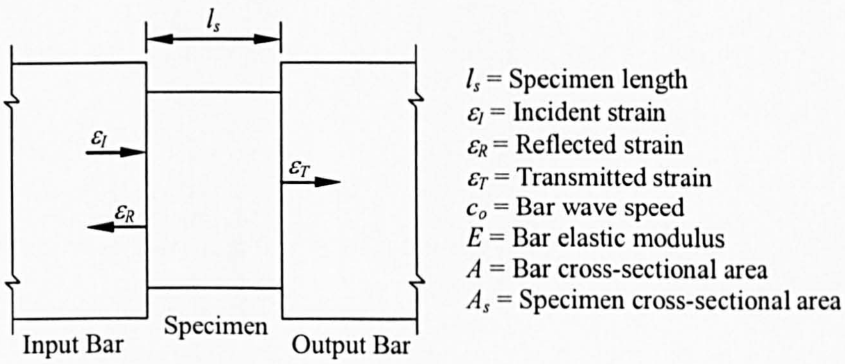

Figure 3-10 Bar-specimen interface

The average strain in a specimen ε_s is found by integrating the reflected strain component ε_R over time:

$$\varepsilon_s = \pm\frac{c_0}{l_s}\int_0^t(\varepsilon_I - \varepsilon_R - \varepsilon_T)dt \tag{3-1}$$

Or

$$\varepsilon_s \cong \pm\frac{c_0}{l_s}\int_0^t \varepsilon_R \, dt \tag{3-2}$$

And for the average strain rate $\dot{\varepsilon}$:

$$\dot{\varepsilon}_s = \pm\frac{c_0}{l_s}(\varepsilon_I - \varepsilon_R - \varepsilon_T) \tag{3-3}$$

Or

$$\dot{\varepsilon}_s \cong \pm\frac{c_0}{l_s}\varepsilon_R \tag{3-4}$$

If a specimen is short, we can assume that the stress across a specimen is constant. Therefore, the average stress in a specimen σ_s is:

$$\sigma_s \cong \pm E\left(\frac{A}{A_s}\right)\varepsilon_T \tag{3-5}$$

Figure 3-11 shows the stress-strain response of a 45 mm diameter specimen. Note that the post-peak stress-strain oscillations are a direct result of the post-peak stress-time oscillations shown in Figure 3-9.

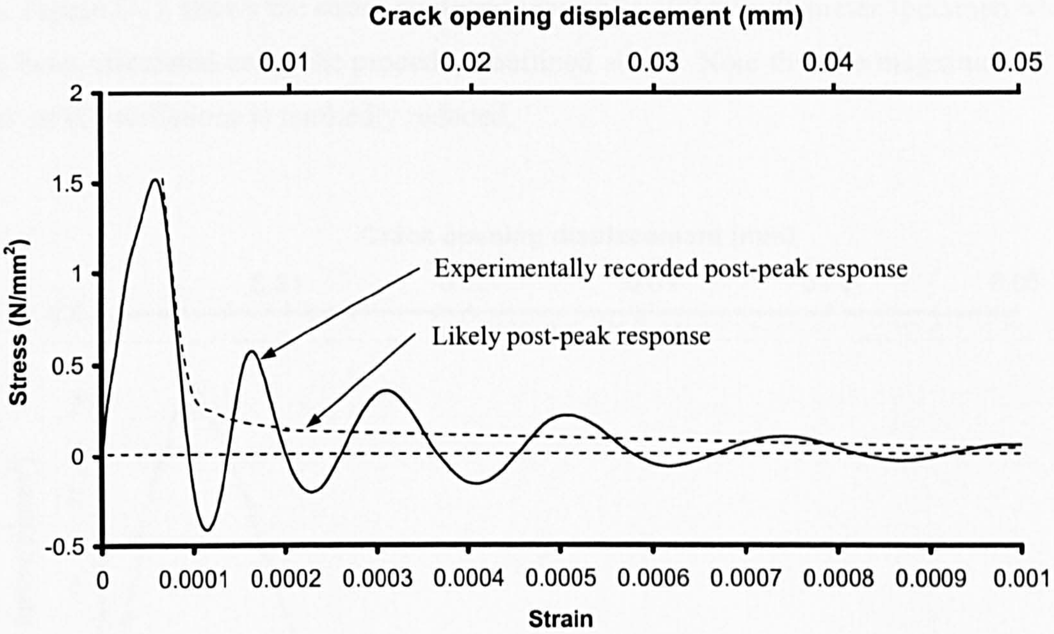

Figure 3-11 Typical stress-strain response for a 45mm diameter specimen

As the specimen starts to fail part of the loading wave is trapped between the bar-specimen interface and point at which the specimen fails. If the brick-mortar joint fails on the input side of the specimen, the trapped wavelength will be 60 mm (i.e. twice the distance between the output bar and the point at which the specimen fails). As the longitudinal wave speed in masonry is approximately 3000 m/s the wave will have a duration of 20 μs. Unless the input and output bars are manufactured from the same material as the specimen, there will be an impedance mismatch at the bar-specimen interface. This causes stress waves to oscillate at a period of 40 μs between the point at which the specimen fails and the bar-specimen interface i.e. the form of the recorded post-peak softening branch is influenced by the dimensions of the specimen used when a SHPB is employed.

It is interesting to compare the stress-strain response of a 45 mm diameter specimen to the stress-strain response of a 100 mm diameter specimen because the impedance mismatch at the output bar-specimen interface is reduced by a factor of approximately 2.5. Figure 3-12 shows the stress-strain response of a 100 mm diameter specimen which has been calculated using the procedure outlined above. Note that the magnitude of the post-peak oscillations is markedly reduced.

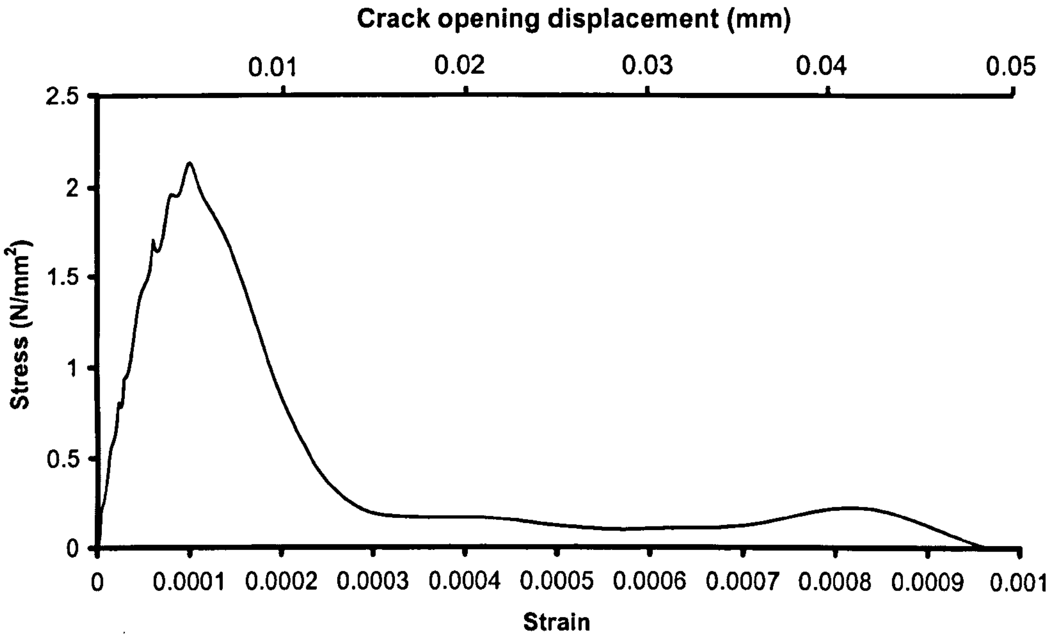

Figure 3-12 Typical stress-strain response for a 100mm diameter specimen

3.5.3 Peak failure stress and dynamic enhancement

Results shown in Table 3-1 and Table 3-2 indicated mean peak failure stresses for specimens subject to dynamic and quasi-static tensile load of 1.56 N/mm^2 and 0.51 N/mm^2 respectively. Therefore, the dynamic increase factor (DIF) is 3.1. To the author's knowledge, this is the first DIF reported for masonry joints. However, similar DIF's have been recorded for concrete subject to dynamic tensile load (Malver & Ross 1998).

The reasons for a dynamic enhancement at increased rates of strain are the subject of much debate. It has been suggested that the DIF may be influenced by specimen dimensions and stress wave effects (Gorham 1991, Dioh *et al.* 1993, 1995). However, due to the limited number of test specimens, it is difficult to make any firm conclusions regarding the choice of specimen dimensions.

Ross *et al.* (1995) reported that the strain rate sensitivity of concrete appeared to be a function of water content. It is well known that concrete is susceptible to shrinkage at excessively high water contents. This can lead to the formation of voids and micro cracks within the matrix. The present author believes that the formation of voids and micro cracks may not be uniform over a cross-section because moisture evaporates more easily from the perimeter. Therefore, the tensile failure stress at the perimeter may be less than at the centre. If a specimen is subject to quasi-static load, stresses are free to progressively redistribute in the cross-section prior to complete failure occurring. However, when dynamically loaded, stresses in a specimen may not have time to redistribute and consequently failure will effectively involve simultaneous mobilisation of all bonds at the brick-mortar interface, irrespective of the relative strengths of these bonds.

In the context of brick masonry, Pluijm (1997) found that the bond area between the mortar and the brick was highly irregular due to shrinkage (Figure 3-13). In many cases, it was observed that the net bond area was asymmetric and restricted to the central part of the specimen. On average, the net bond area was found to be just 35% of the cross-sectional area. Therefore, when a masonry joint is subject to quasi-static tension, there is likely to be a non-uniform stress distribution, with failure initiating at the weakest part of the cross-section, and stresses quickly redistributing.

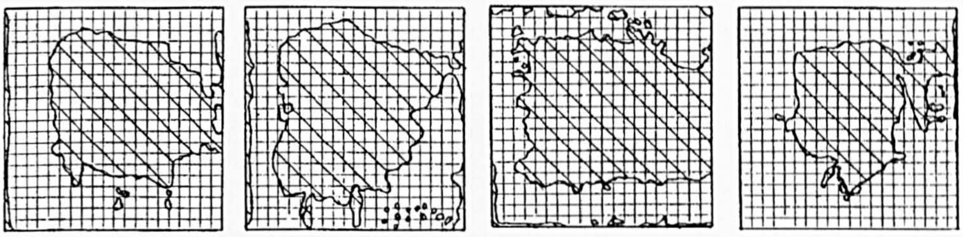

Figure 3-13 Net bond surface of a masonry joint (Pluijm 1997)

When a specimen is subject to a dynamic load, the applied stress is initially almost uniform because flexural waves propagate more slowly than longitudinal waves. As the load increases stress cannot redistribute at a fast enough rate, allowing the specimen to carry a higher load for a short period. To investigate this phenomenon more closely, a numerical model of the bar and specimen was set up.

3.6 Numerical modelling

3.6.1 Introduction

The test set-up has been modelled using a 3D non-linear explicit finite element code incorporating a masonry specific joint interface model. Chapter 4 gives full details of the joint interface model. Though it is usually common practice (and more computationally efficient) to model cylindrical bars in two dimensions using an axi-symmetric model, a three-dimensional model is required to investigate the influence of an irregular bond area.

3.6.2 Description of model

For sake of computational efficiency the whole SHPB rig was not modelled. Instead, input and output bars which were 1100 mm long with a diameter of 101.6 mm were modelled. The specimen sandwiched between these was assumed to be 50 mm thick, with a diameter of 100 mm (Figure 3-14). Material properties are given in Table 3-3. A non-reflecting boundary condition was imposed at the free end of the input and output bars. Both bars and the specimen were modelled using 8-noded solid elements and an elastic material model. Single point integration was used with viscous hourglass control (Hallquist 1998).

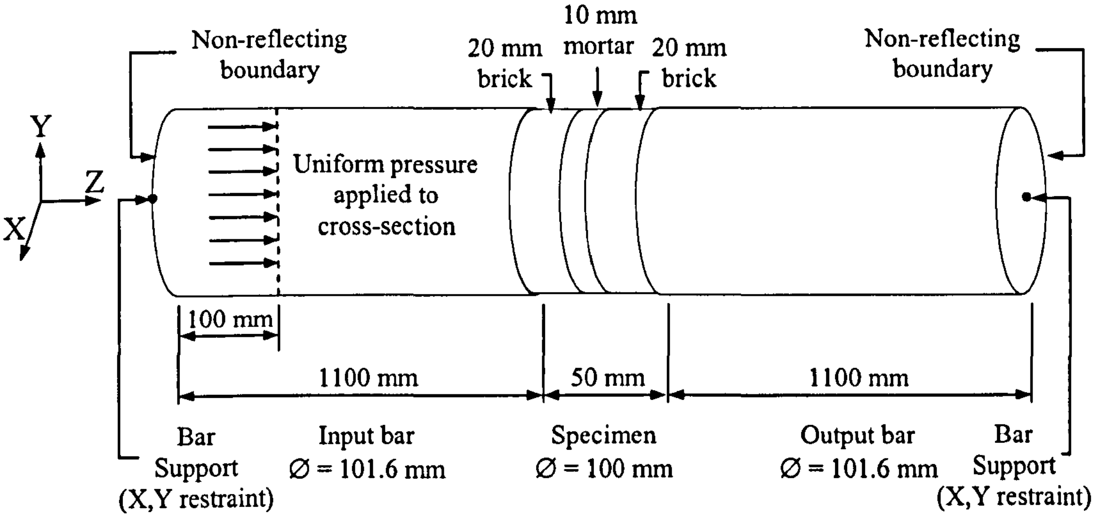

Figure 3-14 Split Hopkinson bar model

Table 3-3 Model properties

Property	Value
Aluminium bar	
Density	2700 kg/m^3
Elastic modulus	70 kN/mm^2
Poisson's ratio	0.33
Brick	
Density	2200 kg/m^3
Elastic modulus	30 kN/mm^2
Poisson's ratio	0.3
Mortar	
Density	1870 kg/m^3
Elastic modulus	10 kN/mm^2
Poisson's ratio	0.3
Brick-mortar interface	
Tensile failure stress	Varies
Shear failure stress	$\sqrt{3}$ × tensile failure stress
Coefficient of friction	0.78
Limit of tensile softening displacement	0.05 mm
Limit of shear softening displacement	0.65 mm
Coefficient of dilatant friction	0.125
Limit of dilatancy	0.8 mm

For the dynamic load case, the bars were constrained from moving out-of-plane i.e. X and Y direction by two nodes positioned at the centre axis, one at either free end. For the quasi-static load case, the node at the free end of the output bar was also constrained from moving in plane. As failure was likely to be influenced by small changes in stress, no gravity was applied to the model.

In the dynamic load case, the input bar, output bar and brick discs were meshed using 5×5×5 mm solid elements (Figure 3-15). The mortar was meshed using 5×5×3.3 mm solid elements. In the static load case, the input and output bars were meshed 10×10×10mm to ensure that the model did not have an excessively long runtime. However, it is important to note that the specimen was meshed using 5×5×5 mm and 5×5×3.3 mm solid elements for both load cases.

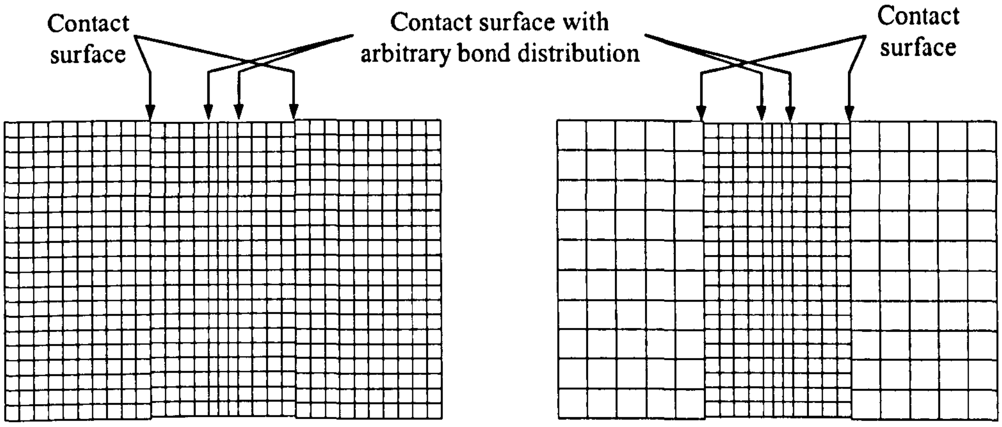

Elevation at bar-specimen interface

Elevation at bar-specimen interface

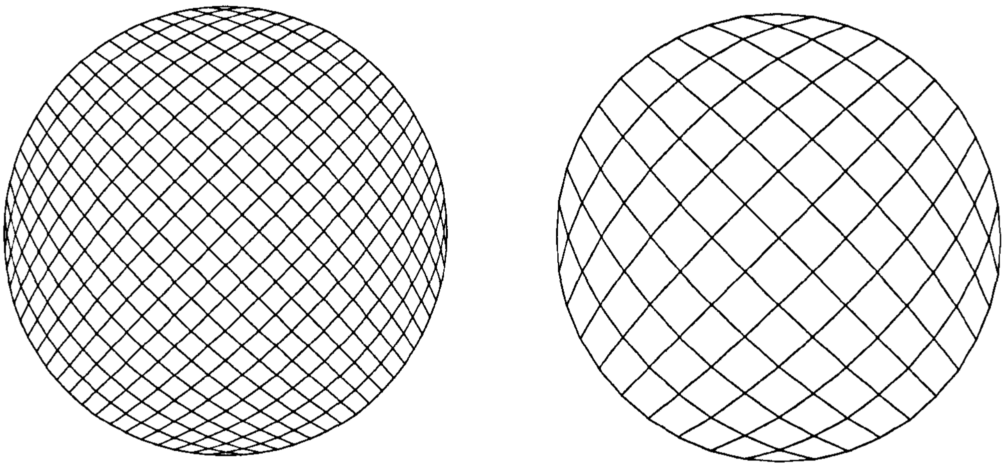

Section through bar
(5×5×5mm)

Section through bar
(10×10×10mm)

Figure 3-15 Mesh density: Left: Dynamic load case Right: Quasi-static load case

To investigate the possible influence of any non-uniformity of the brick-mortar bonding, three arbitrarily chosen bond distributions are investigated (Figure 3-16):

(i) Uniform failure stress.

(ii) 25% of the interface has the mean quasi-static failure stress; 75% of the interface has the mean dynamic failure stress.

(iii) 50% of the interface has the mean quasi-static failure stress; 50% the interface has the mean dynamic failure stress.

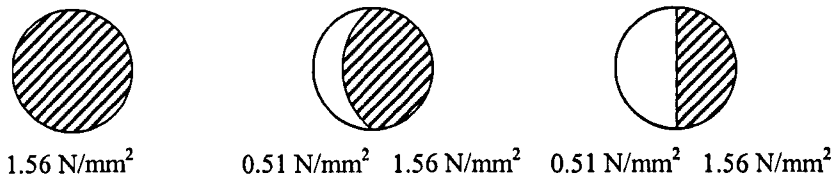

Figure 3-16 Detail showing variation of failure stress in the brick-mortar interface.

With each of the three bond distributions present, dynamic and quasi-static tensile loads were applied to the SHPB model. In dynamic cases, an experimentally recorded stress-time history was applied to the input bar. In the quasi-static case, the specimen was loaded to failure in approximately 100 ms (this is 1000 times longer than the duration of the dynamic test).

3.6.3 Numerical model results

Table 3-4 gives details of the numerically predicted quasi-static and dynamic mean failure stresses. The mean failure stress was taken to be that recorded at the centre of the output bar, 1 m from the specimen-bar interface.

Table 3-4 Details of quasi-static and dynamic mean failure stress

Bond distribution		Quasi-static mean failure stress (N/mm^2)	Dynamic mean failure stress (N/mm^2)	DIF
(i)	100% 1.56 N/mm^2	1.55	1.55	1.00
(ii)	75% 1.56 N/mm^2 25% 0.51 N/mm^2	0.58	1.16	2.00
(iii)	50% 1.56 N/mm^2 50% 0.51 N/mm^2	0.50	0.74	1.48

From Table 3-4 it is evident that the presence of a weak zone amounting to 25% of the cross-sectional area reduced the mean dynamic failure stress by 25%. When the same cross-section was subject to quasi-static load the mean failure stress reduced by approximately 63%. This resulted in a DIF of 2. Increasing the weak zone to 50% of the cross-section reduced the dynamic and quasi-static failure stress by 52% and 68% respectively.

The results in Table 3-4 support the conjecture that it is likely to be the uneven distribution of bond across the cross-section which leads to DIFs greater than unity. Furthermore, it is quite possible that for some other arbitrary distribution of bond the quasi-static and dynamic mean failure stresses are 0.51 N/mm^2 and 1.56 N/mm^2 respectively (i.e. the measured mean quasi-static and dynamic failure stresses).

Figure 3-17 shows the predicted stress-time response of a 100 mm diameter specimen subject to dynamic load. It can be observed that the amplitude of the oscillations overwriting the softening branch is markedly reduced when the specimen fails at a lower peak stress. Therefore, the post-peak oscillations are influenced by the time taken for a specimen to fail.

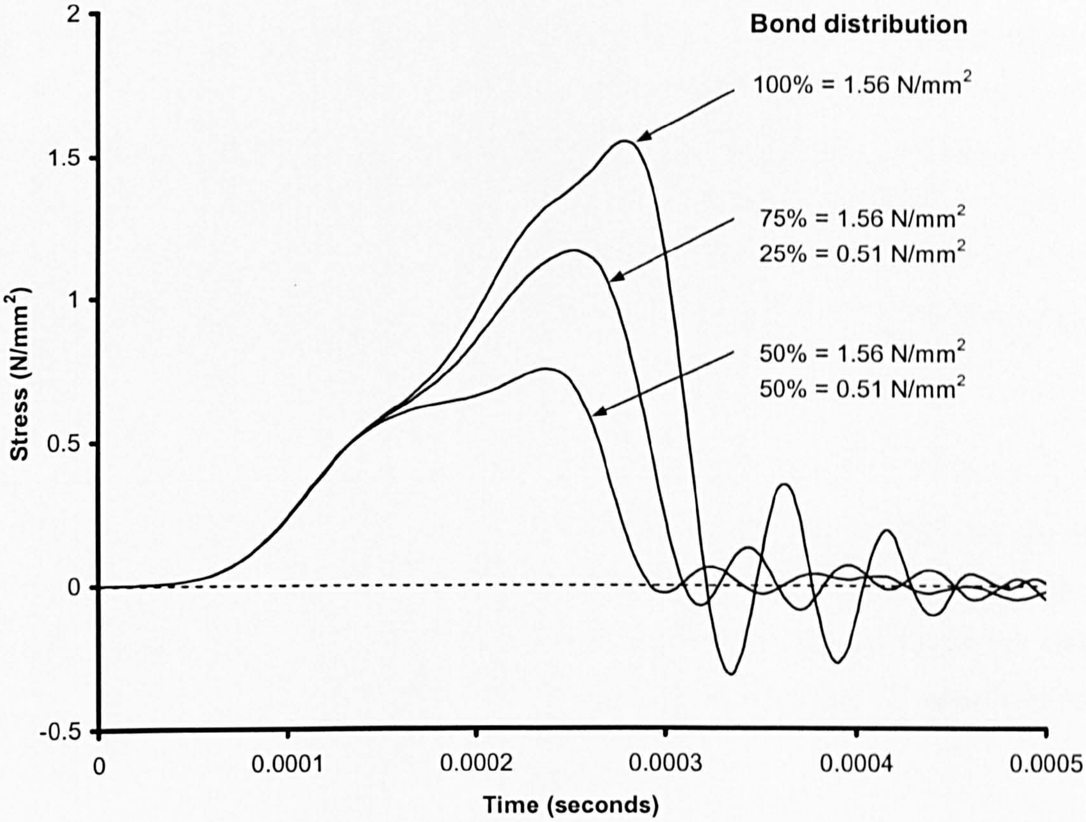

Figure 3-17 Predicted stress-time response of a 100 mm diameter specimen subject to dynamic load

The overall form of the predicted stress-time response shown in Figure 3-17 is similar to the experimentally observed stress-time response shown in Figure 3-9. However, it is important to note that the time required to reach peak failure is influenced by the characteristics of the loading wave and mean failure stress at the brick-mortar interface. Furthermore, the time required to reach the end of the post-peak softening branch is influenced by an assumed limiting tensile displacement.

3.7 Application of results to numerical modelling

When modelling masonry joints it is usually common practice to assume a 100% bond at the brick-mortar interface. However, Pluijm (1997) showed that the average net bond area of a masonry joint might typically comprise just 35% of the cross-sectional area. If variable bond area is not taken into account, the quasi-static tensile failure stress used in a model will underestimate the actual bond strength. This may not be important in a quasi-static problem provided the force required to fail a joint is the same.

In a dynamic problem, numerical work has shown that the force required to fail a joint is influenced by bond distribution. When a 'weak zone' was assigned to 25% of the interface area the joint failed at twice the quasi-static failure stress. Furthermore, when a weak zone was assigned to 50% of the interface area the joint failed at 1.5 times the quasi-static failure stress. Therefore, when modelling the response of masonry joints at strain rates of approximately 1 s^{-1} or higher it would seem to be important to consider the influence of net bond area.

3.8 Conclusions

A large diameter stored energy SHPB rig has been developed specially for use with masonry joints and other low strength quasi-brittle materials. In particular, use of semiconductor strain gauges enabled strain to be resolved to approximately 0.1 μstrain (equivalent to a stress of 0.007 N/mm^2), at least an order of magnitude higher than when using standard electrical resistance strain gauges.

Brick specimens tested in tension at strain-rates of approximately 1 s^{-1} indicated an apparent dynamic enhancement of bond strength (DIF = 3.1). However, finite element modelling studies showed this effect is probably caused by the inherent variability of the unit-mortar bond, and may not be a genuine material characteristic *per se*.

The form of the recorded post-peak softening branch was shown to be influenced by the dimensions of the specimen used when a SHPB is employed. Furthermore, a numerical model showed that the magnitude of the oscillations overwriting the softening branch was influenced by the rate at which a specimen failed.

Due to the small number of specimens tested, it is difficult to draw any firm conclusions regarding the influence of specimen dimensions on the DIF. However, from the results reported in Table 3-1 and Table 3-2, quasi-static and dynamic mean failure stresses do not appear to be influenced by specimen dimensions.

3.9 Acknowledgements

The author would like to acknowledge the assistance provided by Dr Andy Tyas both throughout the project and for correcting the SHPB results for dispersion. Also acknowledged is the support of the technical staff at the University of Sheffield. Finally, the support of EPSRC, under grant references GR/M43128, GR/M43135 and GR/M43142 is acknowledged.

3.10 References

Albertini C, Montagnani M (1994); Study of the true stress-strain diagram of plain concrete with real size aggregate; need for and design of a large Hopkinson bar bundle; Journal de Physique IV, Colloque C8, 113-118.

Bažant ZP, Kazemi MT (1990); Determination of fracture energy, process zone length and brittleness number from size effect, with application to rock and concrete; International Journal of Fracture, 44, 111-131.

Cadoni E, Labibes K, Berra M, Giangrasso M, Albertini C (2001); Influence of Aggregate Size on Strain-Rate Tensile Behaviour of Concrete; ACI Materials Journal, Vol. 98, 220-223.

Davies RM (1948); A Critical Study of the Hopkinson Pressure Bar; Philosophical Transactions of the Royal Society of London A, Vol. 240, 375-457.

Diamaruya M, Kobayashi H, Nonaka T (1997); Impact tensile strength and fracture of concrete; Journal de Physique IV, Colloque C3, 253-258.

Dioh NN, Ivankovic A, Leevers PS, Williams JG (1995); Stress wave propagation effects in the split Hopkinson pressure bar tests; Proceedings of the Royal Society of London A, Vol. 449, 187-204.

Dioh NN, Leevers PS, Williams JG (1993); Thickness effects in split Hopkinson pressure bar tests; Polymer, Vol. 34, 4230-4234.

Espinosa HD, Patanella AJ, Fischer M (2000); Dynamic Friction Measurements at Sliding Velocities Representative of High-Speed Machining Processes; Journal of Tribology, 122, 834-848.

Follansbee PS, Frantz C (1983); Wave propagation in the Split Hopkinson pressure bar; Journal of Engineering Materials and Technology, 105, 61-66.

Gilbert M, Hobbs B, Molyneaux TCK (2002); The performance of unreinforced masonry walls subjected to low-velocity impacts: experiments; International journal of impact engineering, 27, 231-251.

Gorham DA (1991); The effect of specimen dimensions on high strain rate compression measurements of copper; Journal de Physique D: Applied Physics, 24, 1489-1492.

Gorham DA (1983); A numerical method for the correction of dispersion in pressure bar signals; Journal de Physique E, 16, 477-479.

Hallquist JO (1998); LS-DYNA user manual; Livermore Software Technology Corporation.

Hartley KA, Duffy J, Hawley RH (1985); The Torsional Kolsky (Split Hopkinson) Bar, Metals Handbook 9th edition, Vol. 8, 218-228.

Hopkinson B (1914); A method of measuring the pressure produced in the detonation of high explosives or by the impact of bullets; Philosophical Transactions of the Royal Society of London A, Vol. 213, 437-456.

Kolsky H (1949); An investigation of the mechanical properties of materials at very high rates of loading; Proceedings of the Physics Society of London B, Vol. 62, 676-700.

Lok TS, Li XB, Liu D, Zhao PJ (2002); Testing and Response of Large Diameter Brittle Materials Subjected to High Strain Rate; Journal of Materials in Civil Engineering, May/June, 262-269.

Malvar LJ, Ross CA (1998); Review of Strain Rate Effects for Concrete in Tension; ACI Materials Journal, Nov-Dec, 735-739.

Pluijm R van der (1997); Non-Linear Behaviour of Masonry Under Tension; Heron, Vol. 42, 25-54.

Ross AC, Tedesco JW, Kuennen ST (1995); Effects of strain rate on concrete strength; ACI Materials Journal, Jan-Feb, 37-47.

Ross AC, Thompson PY, Tedesco JW (1989); Split-Hopkinson Pressure-Bar tests on concrete and mortar in tension and compression; ACI Materials Journal, Sept-Oct, 475-481.

Rossi P, Mier JGM van, Toutlemonde F, Le Maou F, Boulay C (1994); Effect of loading rate on the strength of concrete subjected to uniaxial tension; Materials and Structures, Vol. 27, 260-264.

Rossi P, Toutlemonde F (1996); Effect of loading rate on the tensile behaviour of concrete: description of the physical mechanisms; Materials and Structures, 29, 116-118.

Rots JG (1997); Structural Masonry: An Experimental/Numerical Basis for Practical Design Rules; AA Balkema, Rotterdam, ISBN 90 5410 680 8.

Syrmakezis CA. Asteris PG (2001); Masonry Failure Criterion under Biaxial Stress State; Journal of Materials in Civil Engineering; Jan/Feb, 58-64.

Tyas A, Watson AJ (2001); An investigation of frequency domain dispersion correction of pressure bar signals; International Journal of Impact Engineering, 25, 87-101.

Zeilinski AJ, Reinhardt HW (1982); Stress-strain behaviour of concrete and mortar at high rates of tensile loading; Cement and Concrete Research, Vol. 12, 309-319.

Zhou H, Gary G (1997); A new method for the separation of waves. Application to the SHPB technique for an unlimited duration of measurement; Journal of Mechanics, Physics and Solids, 45, 1185-1202.

3.11 Postscript

Chapter Three has shown that brick-mortar specimens tested in tension at strain-rates of approximately 1 s^{-1} indicated an apparent dynamic enhancement of the bond strength (DIF = 3.1). Initially it might appear that an 'enhanced' tensile failure stress should therefore be used when modelling the dynamic response of masonry structures. However, the term 'dynamic' can refer to any strain rate that is not deemed quasi-static. Ideally, it would be most realistic to model the real irregular distribution of bonding and to use the dynamic failure properties. Such a model should work satisfactorily with both dynamic and quasi-static loading regimes. However, modelling irregular bond distributions is difficult. Hence, the question arises: assuming a uniform distribution of failure stress, is it appropriate to use enhanced failure stresses when modelling the response of masonry walls subject to out-of-plane impacts?

Dynamic enhancement appears to occur because the unit-mortar bond is uneven and because stresses cannot redistribute at a fast enough rate, allowing a specimen to carry a higher load for a short period. The rate at which stresses can redistribute is influenced by the loading rate or, more appropriately, the rate at which a crack opens. Figure 3-18 shows crack opening displacement vs. time for a masonry specimen subject to quasi-static and dynamic load (results have been taken from a Hopkinson Bar model with uniform bond area).

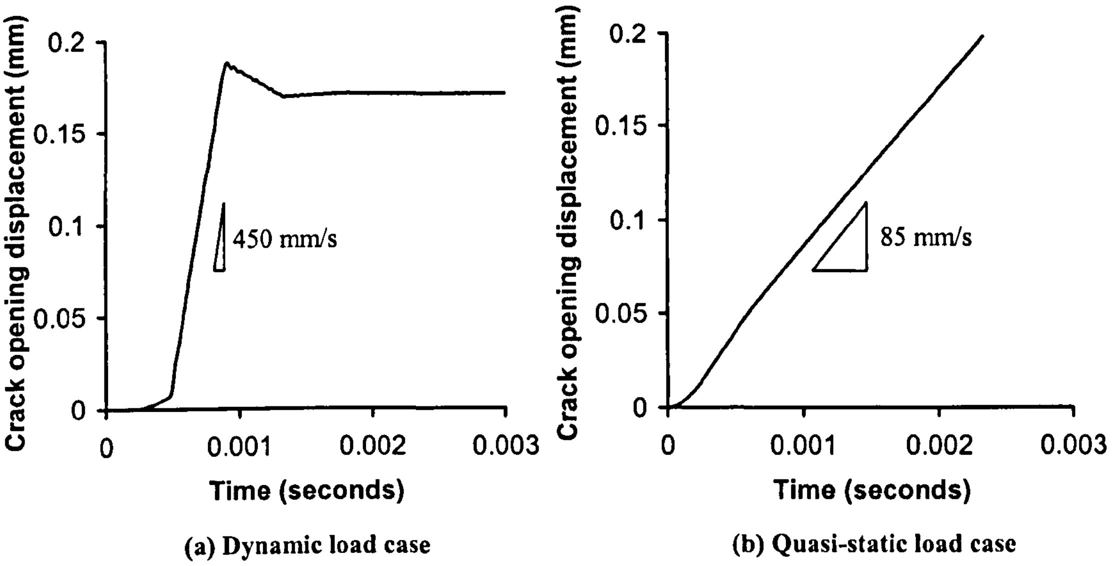

(a) Dynamic load case

(b) Quasi-static load case

Figure 3-18 Mean crack opening displacement rate

From the slope of the displacement-time histories in Figure 3-18 it is apparent that the crack opening velocity for dynamic and quasi-static load cases is approximately 450 mm/s and 85 mm/s respectively. The dynamic and quasi-static crack opening velocities can be compared to a model of a typical masonry wall subject to an out-of-plane car-like impact at mid-length (note that the modelling strategy described in Chapter Four has been used in this case). Figure 3-19 shows crack opening displacement vs. time for a vertical joint behind the point of impact.

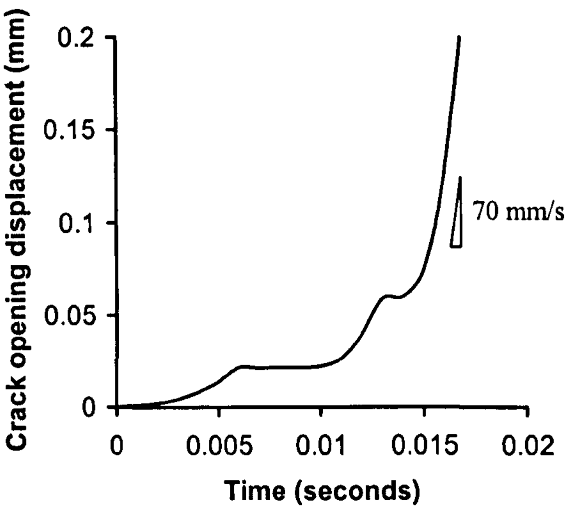

Figure 3-19 Crack opening displacement for a vertical joint in a masonry wall subject to an out-of-plane impact

From Figure 3-19 it is apparent that the crack opening velocity is much slower than the dynamic load case used in the Hopkinson Bar model. Furthermore, even if the crack opening velocity is determined from the steepest part of the curve it is just 70 mm/s i.e. similar to the quasi-static load case used in the Hopkinson Bar model. Therefore, in this particular case, stresses in a masonry joint are likely to have time to redistribute. This appears to indicate that quasi-static tensile failure stresses should be used when modelling the response of masonry walls subject to out-of-plane impacts.

Chapter Four

Numerical modelling of unreinforced masonry walls subject to out-of-plane car-like impacts

Summary

This chapter describes the development and application of a modelling approach suitable for unreinforced brickwork and blockwork masonry walls subject to out-of-plane impacts. The approach incorporates a specially formulated masonry specific interface model. Key features include: (i) a Mohr-Coulomb failure criterion; (ii) a post-peak softening branch following initial fracture; (iii) inclusion of dilatancy. The interface model was implemented in LS-DYNA, a three-dimensional non-linear explicit finite element program.

The model has been validated against results from a series of unreinforced walls tested previously in the laboratory. Results showed the proposed modelling strategy was in general able to predict the dynamic response of full-scale masonry walls with reasonable accuracy. However, a parametric study showed wall response was highly dependent on small changes in loading impulse, base friction, fracture energy, joint failure stress and angle of dilatancy.

4.1 Introduction

The road and rail networks across the UK intersect at many locations. Road/rail intersections may take the form of tunnels, level crossings or bridges. Even though modern bridges are constructed from concrete and steel there are thousands of masonry arch bridges with masonry parapets still in use today - some are of great historical importance. When these parapets were originally built they were designed to protect pedestrians and livestock from precipitous drops. However, with the rise of the motor vehicle in modern society, these parapets are now required to resist vehicular impact loading.

Whilst in many cases, masonry parapets may deflect an errant vehicle and prevent it from leaving the carriageway, there is a real risk of masonry units being ejected from the wall into the surrounding area. This may not be too problematic if the parapet passes over a river but in the case of a railway line or busy road, serious consequences could arise.

Recent high profile incidents in the UK have focussed attention on the performance of bridge parapets and their ability to prevent vehicles leaving the carriageway and falling onto railway lines. Over the past 25 years, The Health and Safety Executive (2002) recorded 13 incidents where vehicles have fallen from bridges or seriously damaged safety barriers.

The County Surveyors Society (CSS) in the UK funded a series of actual parapet impact tests on a range of masonry walls (Middleton 1994). The wall types tested included brickwork, blockwork, random rubble and dry stone. The tests took place at the Motor Industries Research Association (MIRA) test ground using a 1.5T vehicle to impact a wall at an angle of 20°. This testing arrangement has been adopted as standard for all new bridge parapet systems. The tests showed that many walls were able to resist vehicle impacts at speeds up to 70 mph. However, all tests took place with the vehicle travelling at 50 mph or more and wall response at lower velocities may be important in assessing the critical vehicle velocity at which a parapet becomes unstable.

Tests carried out by the CSS provided much needed experimental data on the response of full-scale parapets subject to impact loading. However, the tests were extremely costly and only a limited number of tests could be conducted. Hence, test repeatability was not assessed. Laboratory impact tests are much more controllable and therefore, in addition to the tests carried out by the CSS, a number of reinforced and unreinforced walls were tested under laboratory conditions to study the different failure modes resulting from impact loading (Gilbert *et al.* 2002a, Chapter 5).

A simplified mechanism analysis tool was developed following the laboratory tests on unreinforced walls (Gilbert *et al.* 2002b). The method was able to identify a critical failure mode for a particular impact location and then predict the out-of-plane displacement-time response. However, the analysis method assumed that walls fail by forming a series of rigid panels separated by vertical fracture lines. In practice, diagonal fracture lines have been observed to form, with out-of-plane sliding displacements being accompanied by local rocking. Furthermore, the assumption that walls must fail as a series of rigid panels meant that the method could not predict whether or not individual masonry units were likely to be ejected from a wall.

Thus the aim of the present work has been to develop a finite element modelling strategy that will enable the response of unreinforced walls tested in the laboratory to be simulated. In particular, it was considered important to develop a strategy general enough both to be able to predict the formation of diagonal fracture lines and also loose block failure modes. Therefore, the remainder of the chapter is devoted to the development and subsequent application of a suitable numerical model.

4.2 Numerical modelling approaches for masonry

4.2.1 Introduction

Previous researchers have attempted to simulate the behaviour of masonry structures by using either a continuum model i.e. a smeared crack approach (Lee *et al.* 1998, Lourenço *et al.* 1998, 1996, Lofti & Shing 1991) or a discrete model i.e. a discrete crack approach (Giambanco & Di Gati 1997, Gilbert *et al.* 1998, Lourenço 1997, 1996, Lofti & Shing 1994) (Figure 4-1).

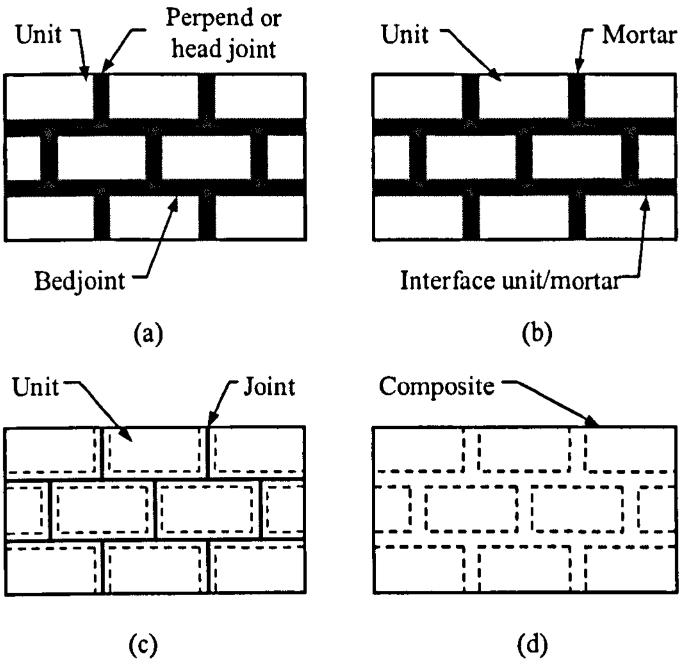

Figure 4-1 Modelling strategies for masonry: (a) masonry sample; (b) detailed micro-modelling (discrete-crack); (c) simplified micro-modelling (discrete-crack); (d) macro-modelling (smeared-crack) (Lourenço 1996)

Smeared crack models are often used to model the non-linear macro behaviour of large structures because they are comparatively computationally inexpensive and can often provide reasonably accurate results. Conversely, discrete crack models are often used to predict the micro behaviour of small structures (or parts of larger structures), particularly where it is important to be able to realistically model the actual interaction between adjacent elements.

4.2.2 Smeared-crack constitutive models

Many constitutive models have been developed to predict the in-plane quasi-static behaviour of masonry walls. However, models that are able to predict the out-of-plane behaviour are less well documented. The continuum model proposed by Lourenço (1998) was initially used to model the in-plane behaviour of masonry shear walls subject to quasi-static loads. The model was later extended to model the out-of-plane behaviour of masonry walls by considering all six components of the stress and strain tensor (Lourenço 2000).

Whilst the anisotropic smeared-crack model proposed by Lourenço was able to predict the out-of-plane quasi-static behaviour of masonry panels with reasonable accuracy, it would not be capable of predicting gross displacements and determining the likelihood of individual units being ejected from a wall. Therefore, the smeared-crack approach appears not to be suitable for modelling the laboratory impact tests.

Results from the laboratory tests showed that for brickwork and blockwork walls failure planes almost invariably coincide with the locations of mortar joints thus justifying a discrete model whereby failure can occur at the interfaces between units. Furthermore, it is now feasible to model large masonry structures using a discrete approach because of increases in available computational power.

4.3 Development of a discrete-crack dynamic modelling strategy

4.3.1 Introduction

A masonry specific discrete-crack model has been implemented in LS-DYNA, a non-linear explicit finite element code (Hallquist 1998). The explicit solution strategy (using a central difference time integration scheme) is particularly advantageous because it eliminates many of the numerical difficulties that arise when modelling crack propagation using implicit solvers. Furthermore, even though the required time step is small compared to that required when using an implicit solver, there are fewer calculations performed at each time step. Hence, the explicit solution strategy is well suited to modelling short duration events such as blasts or impacts.

The overall modelling strategy proposed here is similar to the simplified micro-model described by Rots (1997) who used an implicit solution strategy to model the quasi-static in-plane behaviour of masonry. However, it is important to note that a penalty stiffness contact algorithm has been used instead of explicit interface elements to model the behaviour of the joints. Also here the formulation is fully three-dimensional. Furthermore, it should be noted that no attempt was made to model explicitly the mortar between the bricks. Instead, solid elements were given composite brick-mortar properties and the specially formulated interface model assigned brick-mortar failure characteristics to the joints between geometrically expanded brick units. Key features of the joint interface model include:

(i) Mohr-Coulomb failure criterion with tension cap.
(ii) Post-peak softening branch following initial fracture.
(iii) Dilatant friction.

4.3.2 Penalty stiffness contact-impact formulation

As a starting point to the modelling work a penalty stiffness formulation is used to calculate the interface stresses (Hallquist 1998, 1985). Using this formulation, surfaces of adjacent bricks are defined with either 'slave' or 'master' properties. Before the onset of fracture, slave surface nodes are 'tied' to the master surface of an adjacent brick. This is achieved by applying a restoring force to a slave node that becomes displaced from its initial position on the master surface. Prior to fracture, the magnitude of the restoring force is proportional to the displacement of the slave node. The interface force F^n causing the displacement u at time step n is initially calculated from:

$$F^n = Du \tag{4-1}$$

Where $D=diag(k,k,k)$ and $u=(u_x,u_y,u_z)^T$ i.e. the elastic displacement between a given slave node and associated master surface. At the next time step i.e. n+1 the trial interface force is obtained from:

$$F_{trial}^{n+1} = F^n + D\Delta u \tag{4-2}$$

Where the stiffness of a contact segment in an interface, k, can be calculated from:

$$k = \frac{P_f A^2 K}{V_e} \tag{4-3}$$

Where P_f is a penalty factor, A is the area of the master segment, K is the bulk modulus of the master segment and V_e is the element volume. In order to restrict penetrations between adjacent bodies the interface stiffness has to be designed to be sufficiently high (this will be apparent later).

Use of excessively large penalty stiffnesses can result in an unstable oscillating solution (Huněk 1993). Conversely, small penalty stiffnesses can result in excessively large penetrations. Therefore, the question arises: what value should we use in the analysis? The default penalty factor P_f value of 0.1 has arisen partly through user experience and partly because it has been shown to give reasonable results. However, LS-DYNA was originally developed for the automotive and aerospace industries and only more recently has it been used to model quasi-brittle fracture.

Results from a parametric study carried out on a blockwork wall suggest that taking $P_f = 0.05$ is likely to give reasonable results. If a physical brick is meshed using 4×3×3 (L×B×W) solid elements then the contact segment stiffness k will be approximately 64000 N/mm. The influence of the choice of P_f on the results is considered in section 4.4.4.

Rots (1997) found that, when using a simplified micro-modelling strategy, the resulting quasi-static response of a masonry pier was too stiff if the interface stiffness was calculated according to:

$$k_n = \frac{E_{unit} E_{joint}}{h_{joint}(E_{unit} - E_{joint})} \tag{4-4}$$

$$k_t = \frac{G_{unit} G_{joint}}{h_{joint}(G_{unit} - G_{joint})} \tag{4-5}$$

Where k_n is the normal stiffness perpendicular to the interface, k_t is the shear stiffness along the boundary layer, h is the thickness of the joint, E is the elastic modulus and G

is the shear modulus. Hence, Rots was only able to justify the interface stiffness based on the overall performance of the model. Elsewhere, Rots has used interface stiffnesses in the range 10 N/mm^2 to 10^6 N/mm^2 but makes no attempt to explain the large variation.

4.3.3 Shear and normal stresses

Once the nodal forces are known, shear and normal interface stresses can be calculated from the contact area associated with each node. The interface stresses are then compared with a predefined failure surface which is described by a Mohr-Coulomb friction relationship (Figure 4-2).

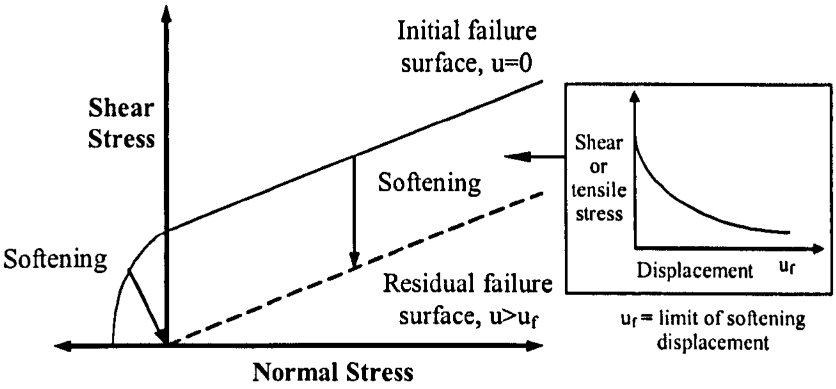

Figure 4-2 Failure envelope for a masonry joint

A hemispherical cap is also used to limit tensile stresses. These are combined in the following failure criterion:

$$1 \le f = \sqrt{\left(\frac{\{\tau_{trial} - \sigma^{c}_{trial}\tan\phi\}}{kc}\right)^2 + \left(\frac{\sigma^{t}_{trial}}{k\sigma^{t}_{f}}\right)^2} \quad \textbf{(4-6)}$$

Where {} are Macaulay brackets, τ_{trial} is the trial shear stress in the interface, c is the cohesion, $\tan\phi$ is the static coefficient of friction, k is a global softening parameter, σ^{t}_{f} is the limiting tensile stress and σ_{trial} is the trial normal stress at the interface:

$$\sigma^{t}_{trial} = \sigma_{trial},\ \sigma^{c}_{trial} = 0 \ when\ \sigma_{trial} \le 0$$

$$\sigma^{c}_{trial} = \sigma_{trial},\ \sigma^{t}_{trial} = 0 \ when\ \sigma_{trial} \ge 0$$

If the stress state lies outside the failure envelope the stresses are reduced so as to lie on the failure surface:

$$\sigma^{t} = \frac{\sigma^{t}_{trial}}{f} \tag{4-7}$$

$$\sigma^{c} = \sigma^{c}_{trial} \tag{4-8}$$

$$\tau = \frac{\left\{\tau_{trial} - \sigma^{c}_{trial}\tan\phi\right\}}{f} + \sigma^{c}_{trial}\tan\phi \tag{4-9}$$

At each subsequent time step the failure surface shrinks due to plastic deformation. This allows the interface between the bricks to soften and exhibit elastic unloading and reloading characteristics. The global softening parameter k controls the rate at which a surface can shrink, where:

$$k = k^{I} + k^{II} - 1 \tag{4-10}$$

and,

$$k^{I} = e^{\left\{\log_e(0.001)\frac{u^{p}_{t}}{u^{I}_{f}}\right\}} \tag{4-11}$$

$$k^{II} = e^{\left\{\log_e(0.001)\frac{u^{p}_{s}}{u^{II}_{f}}\right\}} \tag{4-12}$$

Where u^{p}_{t} and u^{p}_{s} are the 'plastic' deformations normal (tensile) and tangential to the interface respectively.

It can be seen from (4-13) and (4-14) that an exponential displacement softening relationship is used for tied nodes that fail in tension (mode I) or shear (mode II). The residual failure surface is for convenience deemed to have been reached when the separation is such that the exponential softening curve indicates that only 0.1% of the maximum (initial failure) shear/tensile bond stress can be transmitted. Thus, the residual displacements u_f required in (13) and (14) can be calculated from the mode I and mode II fracture energies and the shear and tensile joint failure stresses:

$$u_f^I = \frac{-\log_e(0.001)G_f^I}{\sigma_f^t} \tag{4-13}$$

$$u_f^{II} = \frac{-\log_e(0.001)G_f^{II}}{c} \tag{4-14}$$

Where G^I_f and G^{II}_f are respectively the mode I and mode II fracture energies. Gilbert *et al.* (2002b) and other researchers (e.g. Rots 1997) have taken the fracture energies associated with a joint built using medium strength mortar to be: G^I_f=0.01 N/mm and G^{II}_f=0.05 N/mm.

4.3.4 Dilatant friction

When masonry fails in shear, displacements which occur parallel to the joint may be accompanied by displacements perpendicular to the joint (respectively δu and δv) (Figure 4-3). The angle of dilatancy ϕ is $\tan^{-1}(\delta u/\delta v)$ and can be estimated from a plot of tangential displacement against normal displacement. Typical measured values of $\tan\phi$ are in the range 0.1 to 0.7 depending on the roughness of the unit surface (Rots 1997). Low confining stress tends to allow a high angle of dilatancy whilst high confining stress tends to give rise to a lower angle of dilatancy. As the joint slides the angle of dilatancy decreases to zero because the unit-mortar surfaces become smoother.

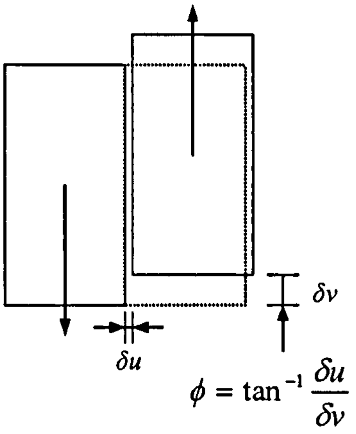

Figure 4-3 Displacement parallel and perpendicular to joint during shear failure

A bilinear model has been used to describe dilatant friction (Figure 4-4). Similar models have been proposed by Giambanco & Gati (1997). Each slave node is assumed to lie in a depression in the joint. Initial resistance to sliding is purely due to unit-mortar bond strength, Coulomb sliding and dilatant friction. When a slave node is displaced from its original position on the master surface it is constrained to move in a direction governed by the angle of dilatancy because movement purely parallel to the interface is interpreted as a penetration according to the penalty stiffness method.

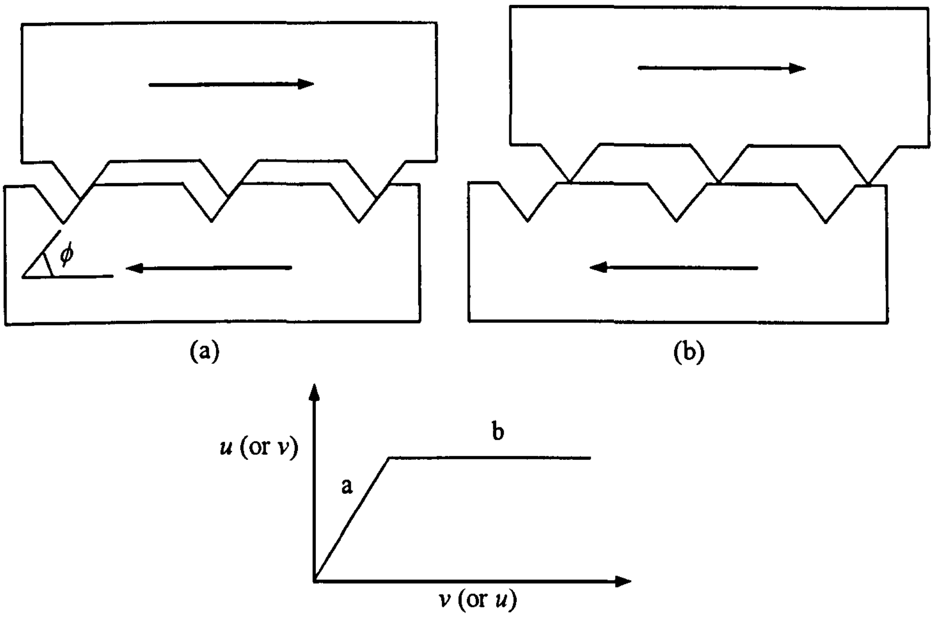

Figure 4-4 Bilinear model showing angle of dilatancy

4.3.5 Zero energy modes

Traditionally in explicit finite element analysis, single integration point elements are employed. These are computationally inexpensive and work well with penalty stiffness interface formulations, even if these are highly non-linear. However, when an element employs one-point integration, displacement modes (other than those corresponding to rigid body motions) may result in zero strain energy i.e. having only one integration point at the centre of the element can give a misleading indication of the global element state and zero energy modes are likely to arise (Figure 4-5).

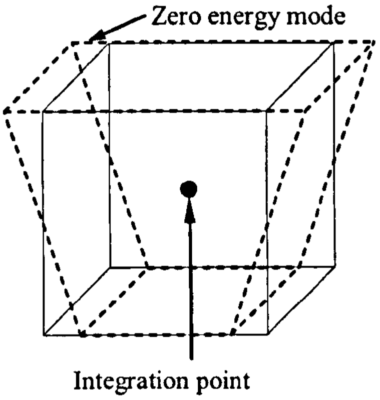

Figure 4-5 Zero energy mode for an 8-node brick element with 1 point integration

Zero energy modes can be resisted by employing more integration points. However, more integration points will increase the CPU time needed to process the model because a greater number of calculations need to be performed at each time step. Another approach to resisting these undesirable zero energy modes is to employ viscous damping or a small elastic stiffness. Additionally, in the present application, it is prudent to mesh each geometrically expanded brick with numerous finite elements.

4.3.6 Interface layout

Due to the modular format of masonry walls a specially devised model generation program was used to define the geometry and the location of the contact interfaces. In an earlier contact formulation the top and bottom surfaces of elements lying on a given bedding plane were assigned the same contact surface number, the upper surface, say, being assigned master properties. Slave nodes were then automatically attached to the adjacent master contact surface by the program LS-DYNA. For example, if slave node X is located at the interface between master surfaces A and B then the node could be attached to either surface (Figure 4-6).

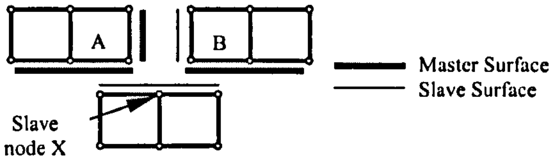

Figure 4-6 Erroneous interface formulation (exploded view)

At first, this may not seem too problematic but since the limiting force in the link connecting node X to its position on the master surface is calculated from an associated slave surface area it is clear that the lower unit will be linked artificially strongly to one or other of the two upper blocks.

This problem was overcome by instead specifying numerous separate contact surfaces per physical bedding plane (e.g. one separate contact surface under each quarter of a physical brick) (Figure 4-7). Using this approach, slave node X will be a member of two different contact surfaces, one with a master surface at the base of block A, the other with a master surface at the base of block B. This approach ensures that there is an equal limiting force in the links connecting the lower block to each of the two upper blocks.

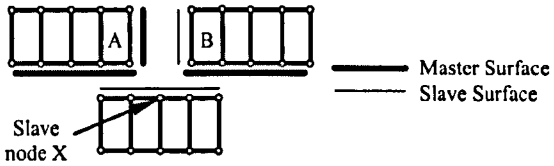

Figure 4-7 Interface formulation (exploded view)

Unfortunately this approach is only suitable when relative displacements between blocks are small, say, less than or equal to 5% of the side length of an element. The problem occurs because no contact surface is defined between blocks A and B′ and between B and C′ (shown in Figure 4-8). Hence, no friction or other forces are transmitted, as they should be in practice.

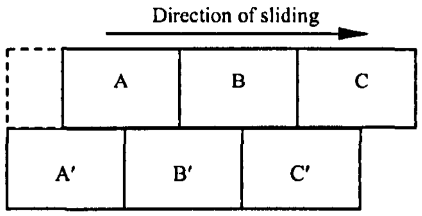

Figure 4-8 Cross section through two courses of a masonry wall showing relative movement between courses

This problem was overcome by implementing a two phase interface formulation, with new second phase (i.e. friction only) contact surfaces being defined between blocks A, B and C and blocks A′, B′ and C′. Therefore, when a tied node on contact segment A, B or C fails, it can subsequently slide across contact segments A′, B′ and C′, properly transferring friction and normal forces.

4.3.7 Applying gravity loading to the model

It is important when modelling masonry walls that gravity stresses are properly included. Gravity was applied to the model using the method of dynamic relaxation. The method involves damping out oscillations following initial application of the gravity base acceleration. Here, this process was assumed to be complete after 50 ms.

4.4 Validation of proposed modelling strategy

4.4.1 Small scale modelling: triplet specimens

The proposed modelling strategy was initially used to model the response of triplet specimens subject to dynamic load (Beattie 2003, Molyneaux & Gilbert 1997). Beattie (2003) investigated the influence of post-peak softening, angle of dilatancy and Mohr-Coulomb shear strength using the triplet model shown in Figure 4-9. Note that in both the modelling and experimental work the loading plates and steel supports were carefully positioned to minimise bending.

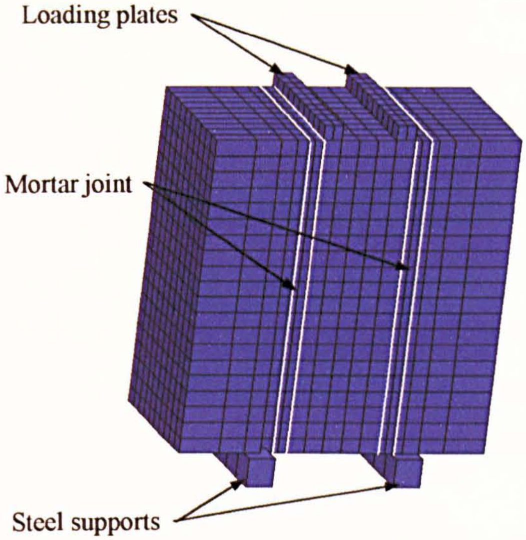

Figure 4-9 Triplet model used by Beattie (2003)

Each physical brick was modelled numerically using 8-noded brick elements and an elastic material model. The same properties were also assigned to the mortar joint. The loading plates and supports were modelled using 8-noded brick elements and an elastic material model. Single point integration was used with viscous hourglass control.

The masonry specific interface model described previously was used to model the brick-mortar interface. Elsewhere, the interfaces between the supports, loading plate and bricks were assumed to be purely frictional. The triplet was loaded by applying a prescribed motion of 60 mm/s to the loading plates.

Results showed that the inclusion of fracture energy and dilatancy significantly increased the apparent mean bond strength. This finding is particularly important because joints were observed to fail prematurely when the model was run with an unmodified version of LS-DYNA.

Beattie concluded that the triplet model could predict the peak failure stress and post-peak response with good accuracy (within 10%). However, when a specimen was subject to a precompression of 0.3 N/mm^2 the model was only able to predict the experimentally observed response to within 30%. In this case, Beattie (2003) believed that the response of the model could be improved by incorporating a relationship between dilatancy, fracture energy and precompression. At present, the model does not allow for variable joint dilatancy or increasing fracture energy with increasing precompression.

4.4.2 Large scale modelling: wall impact tests

The model was then applied to some of the full-scale wall impact tests described by Gilbert *et al.* (2002a). Details of the experimental test set-up are shown in Figure 4-10. For convenience, construction details are summarised in Table 4-1.

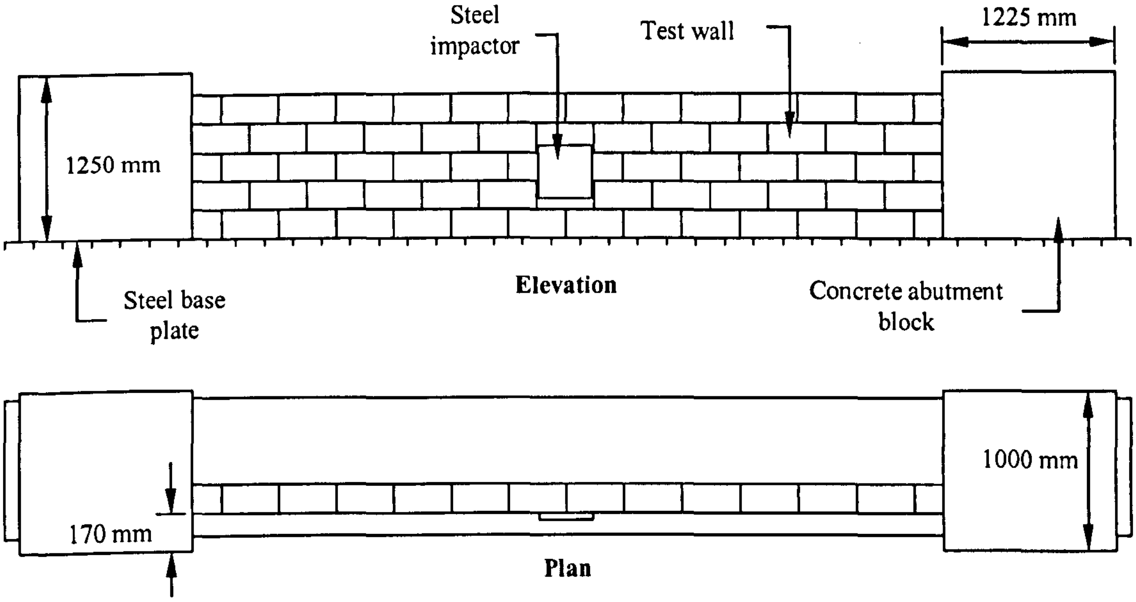

Figure 4-10 Test arrangement showing position and dimensions of concrete abutment blocks

Table 4-1 Details of test walls

Wall ref.	Units	Length (mm)	Breadth (mm)	Height (mm)	Abutment	Impact location	Full mortar bonding at base?	Remarks
C6	Strong block	9150	215	1130	2 × free	Central	Limited[A]	
C7	Strong block	9150	215	1130	2 × free	Central	Yes	
B1	Brick	9150	215	1070	2 × free	Central	Yes	
B2	Brick	9150	215	1030	None	Central	Yes	
B3	Brick	9150	330	1030	2 × free	Central	Yes	
B4	Brick	9150	330	1030	None	Central	Yes	
B5	Brick	9150	440	1030	2 × free	Central	Yes	
B6	Brick	9150	215	1030	2 × free	Central	Yes	Short duration impact
B7	Brick	20000	215	1030	None	Central	Yes	

[A] Base plate coated with release agent.

Brickwork walls were constructed using Marshalls' solid red smooth Accrington Nori clay engineering bricks (class B) with a class (iii) mortar to BS 5628(i) (1:1:6 cement:lime:sand). The walls were 13 courses high and English garden wall bond was used throughout. Blockwork walls were constructed from concrete blocks with a class (iii) mortar (1:1:6). The walls were 5 courses high and stretcher bond was used throughout. Testing took place at nominally 28 days.

Each wall was subject to an out-of-plane car-like impact at mid-length. Details of the applied loading are given in Table 4-2. A typical force-time history is shown in Figure 4-11.

Table 4-2 Details of applied load

Wall ref.	Drop height (m)	Mass (kg)	Approx. peak force (kN)	Applied impulse (kNs)[A]	Recorded /applied impulse	Remarks
C6	0.82	690	110	2.77	0.96	
C7	0.82	690	160	2.77	0.92	
B1	2.5	380	130	2.66	1.07	
B2	2.5	380	110	2.66	0.95	
B3	2.5	690	320	4.83	0.98	
B4	1.27	1010	180	5.04	1.03	
B5	2.00	1525	330	9.55	0.99	
B6	3.43	277	420	2.27	0.88	Short duration impact
B7	0.82	690	130	2.87	0.91	

[A] Assuming zero rebound and 100% of free fall velocity, to top of specimen. Mass of quadrant neglected.

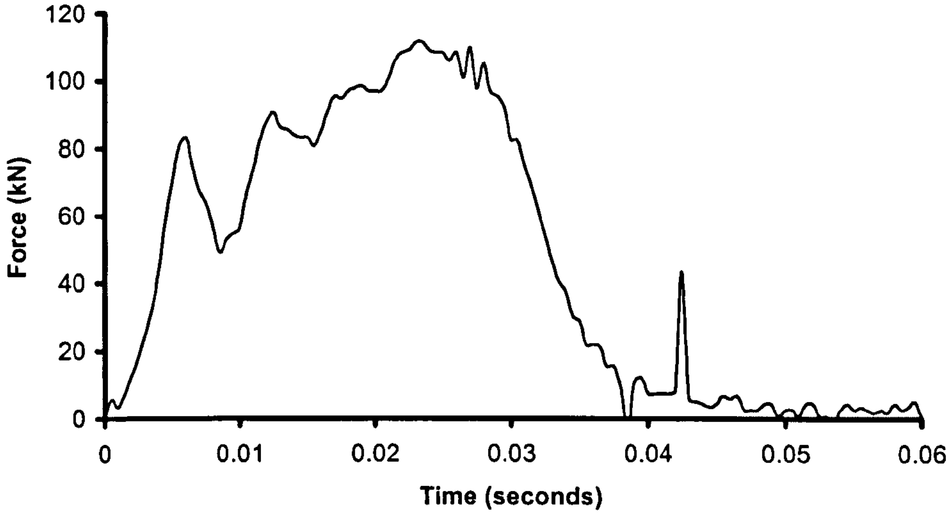

Figure 4-11 Typical force-time history applied to model (taken from wall C6)

4.4.3 Material and interface data

Most of the material and interface data has been obtained from an extensive small-scale test programme (Beattie 2003). The main aim was to determine the basic engineering properties of the constitutive materials used in the full-scale wall tests (Table 4-3 and Table 4-4).

Table 4-3 Properties of laboratory walls

Property	Value	Comment
Base-mortar interface		
Coefficient of sliding friction	0.725	Total base friction = 0.85 (sliding friction + dilatancy) (Gilbert *et al.* 2002a)
Shear strength	0.2 N/mm^2	Measured on steel base plate in laboratory (Gilbert *et al.* 2002a)
Tensile strength	0.143 N/mm^2	Estimate, based on measured steel base plate shear strength above.
Brick-mortar interface		
Shear strength	0.63 N/mm^2	Determined from 57 triplet tests (Beattie 2003)
Tensile strength	0.45 N/mm^2	Determined from 18 tension tests (Beattie 2003 & Chapter 3)
Mode II fracture energy	0.059 N/mm	Determined from 57 triplet tests (Beattie 2003)
Mode II ultimate displacement	0.65mm	Determined from 57 triplet tests (Beattie 2003)
Mode I fracture energy	0.01 N/mm	Value taken from experimental work by Rots (1997)
Mode I ultimate displacement	0.15mm	See below
Coefficient of dilatancy (tanϕ)	0.125	Determined from 4 shear tests (Beattie 2003)
Limit of dilatancy	0.8mm	Determined from 4 shear tests (Beattie 2003)
Coefficient of sliding friction	0.78	(Beattie 2003)
Brickwork composite		
Density	2200 kg/m^3	
Elastic modulus	20 kN/mm^2	
Poisson's ratio	0.3	
Blockwork composite		
Density	2295 kg/m^3	
Elastic modulus	20 kN/mm^2	
Poisson's ratio	0.3	

Table 4-4 Properties of impact plate, base pad and abutments

Property	Value
Steel impact plate	
Density	7800 kg/m^3
Elastic modulus	200 kN/mm^2
Poisson's ratio	0.3
Steel-brick interface	
Coefficient of friction	0.3
Concrete base pad and abutments	
Density	2400 kg/m^3
Elastic modulus	40 kN/mm^2
Poisson's ratio	0.3

4.4.4 Validation of model against numerical parameters

The influence of mesh size, interface stiffness and time-step has been investigated using wall C6 as a benchmark problem. For the mesh study, each (geometrically expanded) physical block was meshed variously using 4x3x3, 8x6x6 or 12x9x9 (LxBxH) solid elements. The model was loaded by applying a bilinear force-time history to the impact plate (Figure 4-12). Note that the peak force, impulse and duration are similar to the experimentally recorded impulse shown in Figure 4-11. The out-of-plane displacement-time history of a node located at a height of 580 mm above the base, 250 mm from the point of impact is shown in Figure 4-13.

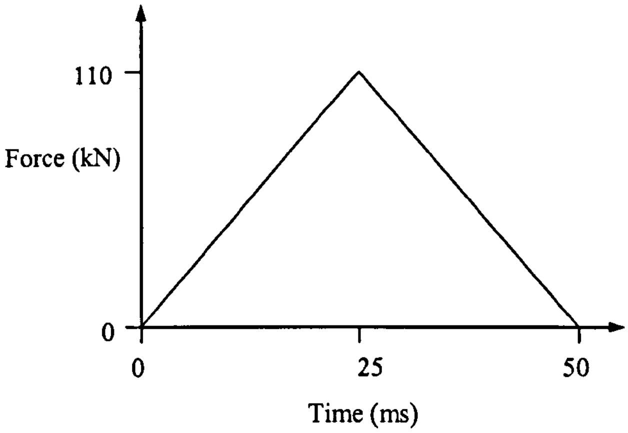

Figure 4-12 Bilinear impulse

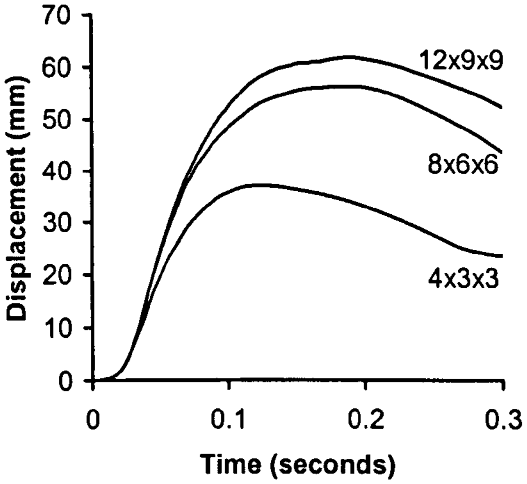

Figure 4-13 Influence of mesh discretisation of blocks (L×B×H)

Figure 4-13 shows that the blockwork model is moderately sensitive to mesh size but that the differences between the two finer mesh trends are relatively small. The relative dimensions of a brick imply that a brickwork model will also be comparatively mesh insensitive when a physical brick is meshed 4×3×3 (L×B×H).

The influence of time-step and interface stiffness was investigated using wall model C6 meshed using 8×6×6 (L×B×H) solid elements. The critical time-step (i.e. the time taken for an elastic wave to traverse the smallest element) was factored by 0.9 (the default value), 0.45 and 0.225. The interface stiffness was factored by 0.1, 0.05 and 0.025. Again, the model was loaded by applying a bilinear force-time history to the impact plate. The out-of-plane displacement-time history of a node located at a height of 580 mm above the base, 250 mm from the point of impact is shown in Figure 4-14.

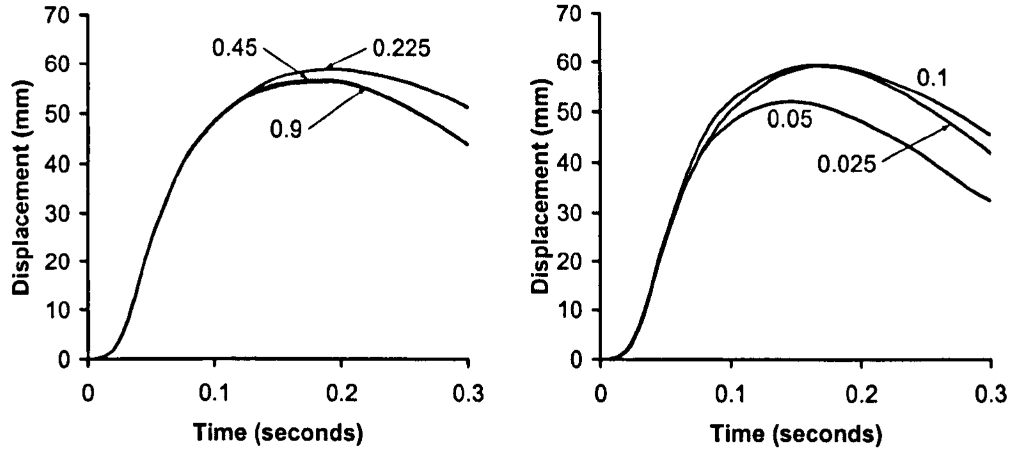

Figure 4-14 Influence of time-step (left) and penalty stiffness (right)

Figure 4-14 shows that the blockwork model is relatively insensitive to time-step and penalty stiffness.

4.4.5 Description of finite element models

Each physical brick in a given laboratory wall was modelled numerically using 4x3x3 (L×B×H) 8-noded solid elements and an elastic material model (Blockwork walls were modelled using 8×6×6 8-noded solid elements). The same properties were also assigned to the base pad and abutments. The impact plate was modelled as a rigid plate. Elsewhere single point integration was used with viscous hourglass control.

4.4.6 Validation of model against experimental results

The model was then applied to the laboratory walls. In all cases the experimentally recorded force-time histories were used in the numerical models, although because these were known to only be accurate to within approximately ±10%, 90% and 110% impulses were also used.

Predicted crack patterns are shown in Figures 4-15, 4-16 and 4-17. For all walls, these may usefully be compared with experimentally observed post-test crack patterns for brickwork and blockwork walls which are shown in Figure 4-18. Figure 4-19 and Figure 4-20 show the out-of-plane displacement-time response of the walls. Unless otherwise stated, displacements shown are those recorded by a gauge positioned at a height of 580 mm above the base, 250 mm from the centre of the applied load.

Table 4-5 gives details of the experimentally observed and predicted characteristic failure mode length and peak out-of-plane displacement. Peak displacements have been taken from the displacement-time data shown in Figure 4-19 and Figure 4-20. Note that values given for peak displacement and approximate length of failure mode were taken from models loaded with 100% of the impulse.

Table 4-5 Summary of test and model results

Wall	**Test: approximate length of failure mode (m)**	**Model: approximate length of failure mode (m)**	**Test: peak displacement (mm)**	**Model: peak displacement (mm)**	**Peak model displacement/ Peak test displacement (Impulse scaled, 90%:100%:110%)**
C6	1.9	2.3	75	99	0.93:1.32:1.51
C7	2.0	2.3	77	52	0.45:0.68:1.00
B1	2.6	2.5	62	64	0.85:1.03:0.97
B2	Varies	Varies	130	50	0.39:0.38:0.84
B3	2.3	2.6	71	44	0.49:0.62:0.85
B4	Varies	Varies	94	91	0.69:0.97:1.28
B5	4.5	4.5	122	172	1.07:1.41:1.78
B6	1.6	1.5	Not known	135	N/A
B7	2.6	2.4	62	51	0.52:0.82:Punched through

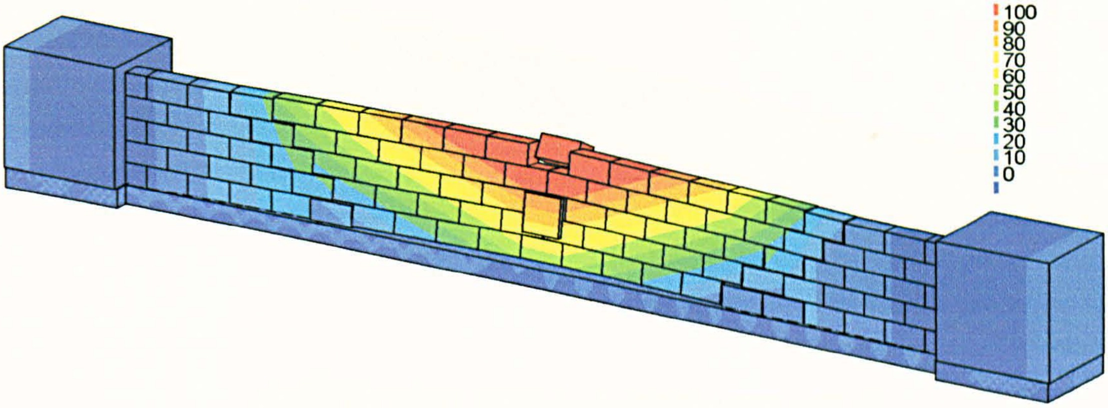

(a) Wall C6: Time = 0.21 seconds, Displacement scale ×2

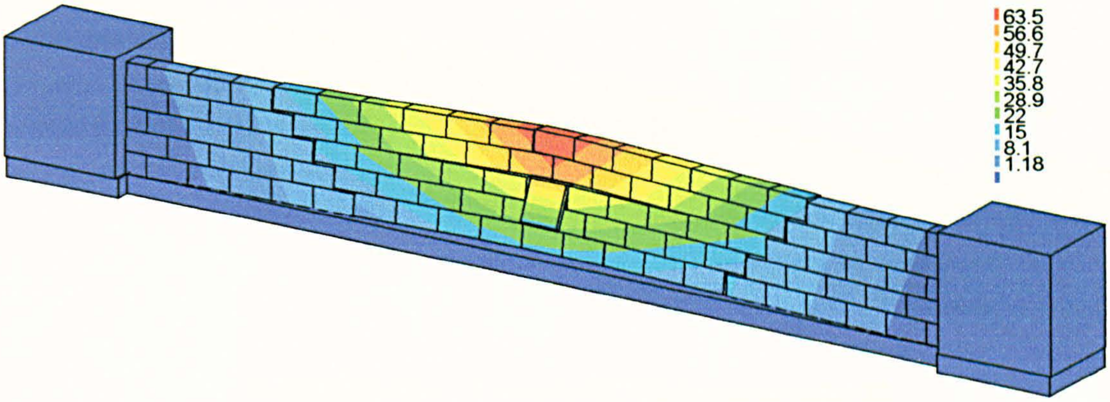

(b) Wall C7: Time = 0.15 seconds, Displacement scale ×5

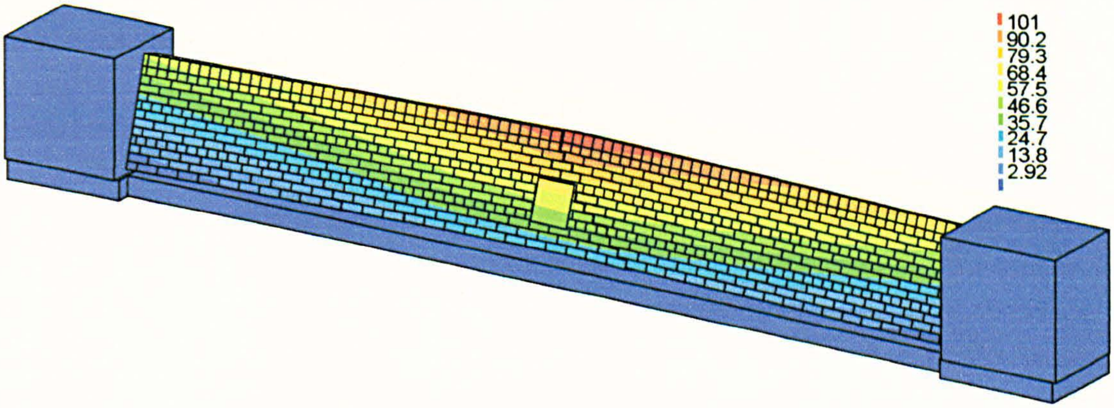

(c) Wall B1: Time = 0.3 seconds, Displacement scale ×5

Figure 4-15 Walls C6-B1 (100% impulse): Out-of-plane displacement (mm)

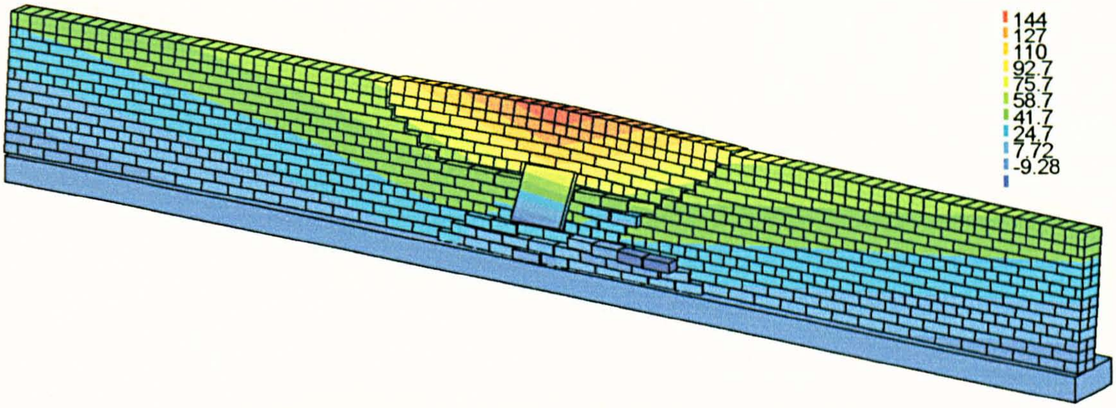

(a) Wall B2: Time = 0.27 seconds, Displacement scale ×2

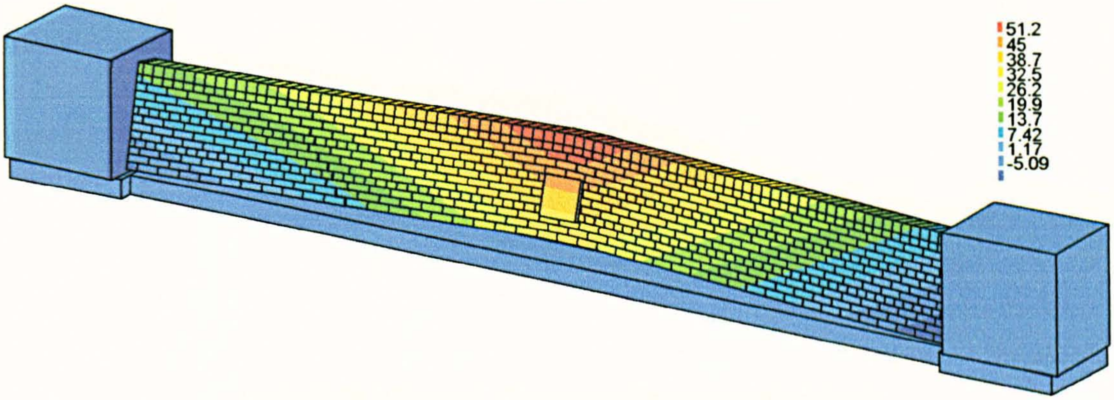

(b) Wall B3: Time = 0.15 seconds, Displacement scale ×10

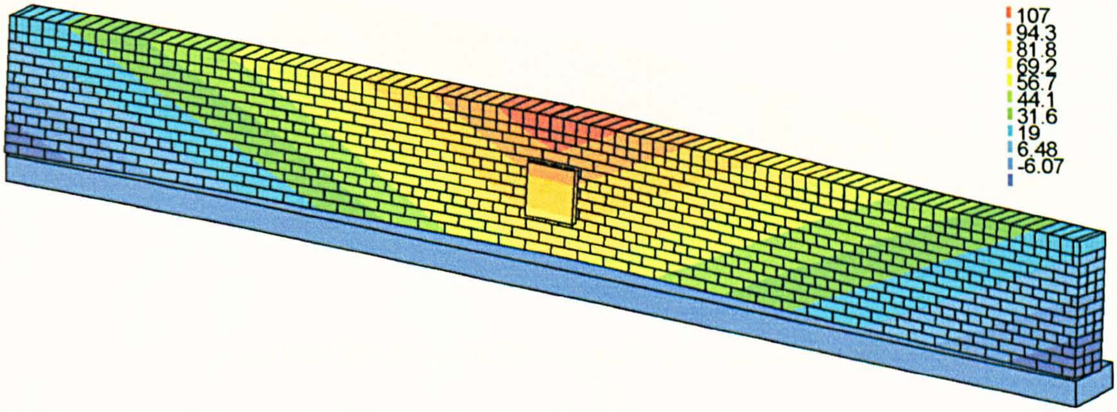

(c) Wall B4: Time = 0.21 seconds, Displacement scale ×2

Figure 4-16 Walls B2-B4 (100% impulse): Out-of-plane displacement (mm)

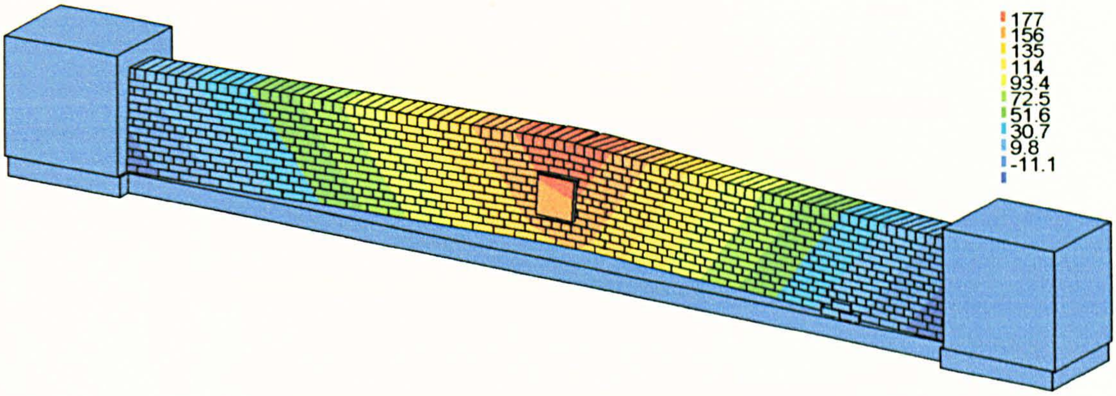

(a) Wall B5: Time = 0.24 seconds, Displacement scale ×2

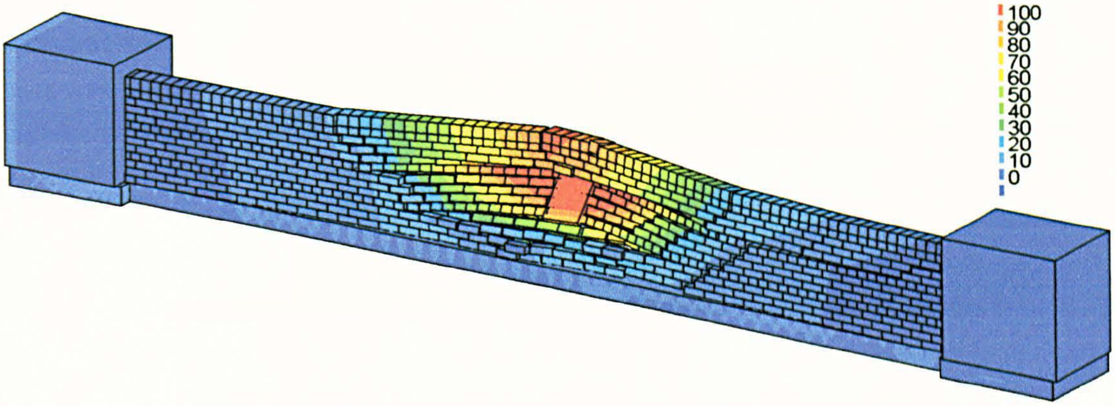

(b) Wall B6: Time = 0.12 seconds, Displacement scale ×5

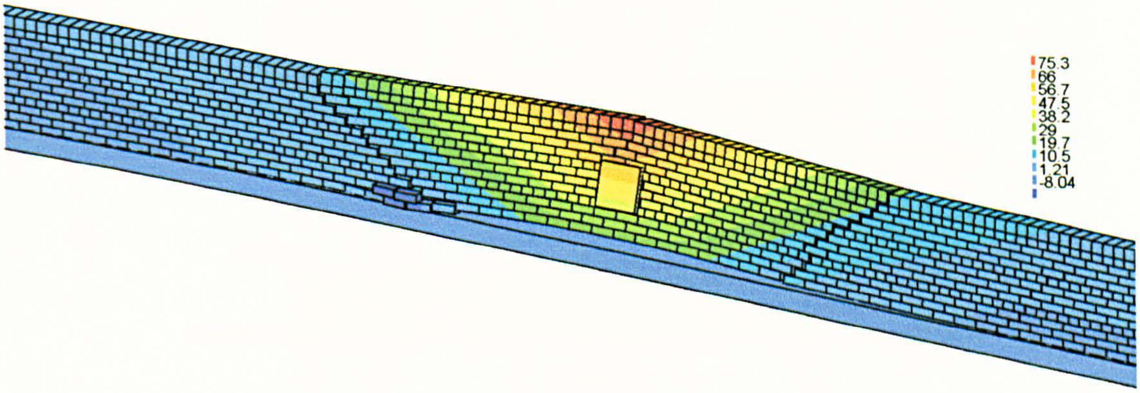

(c) Wall B7: Time = 0.18 seconds, Displacement scale ×5

Figure 4-17 Walls B5-B7 (100% impulse): Out-of-plane displacement (mm)

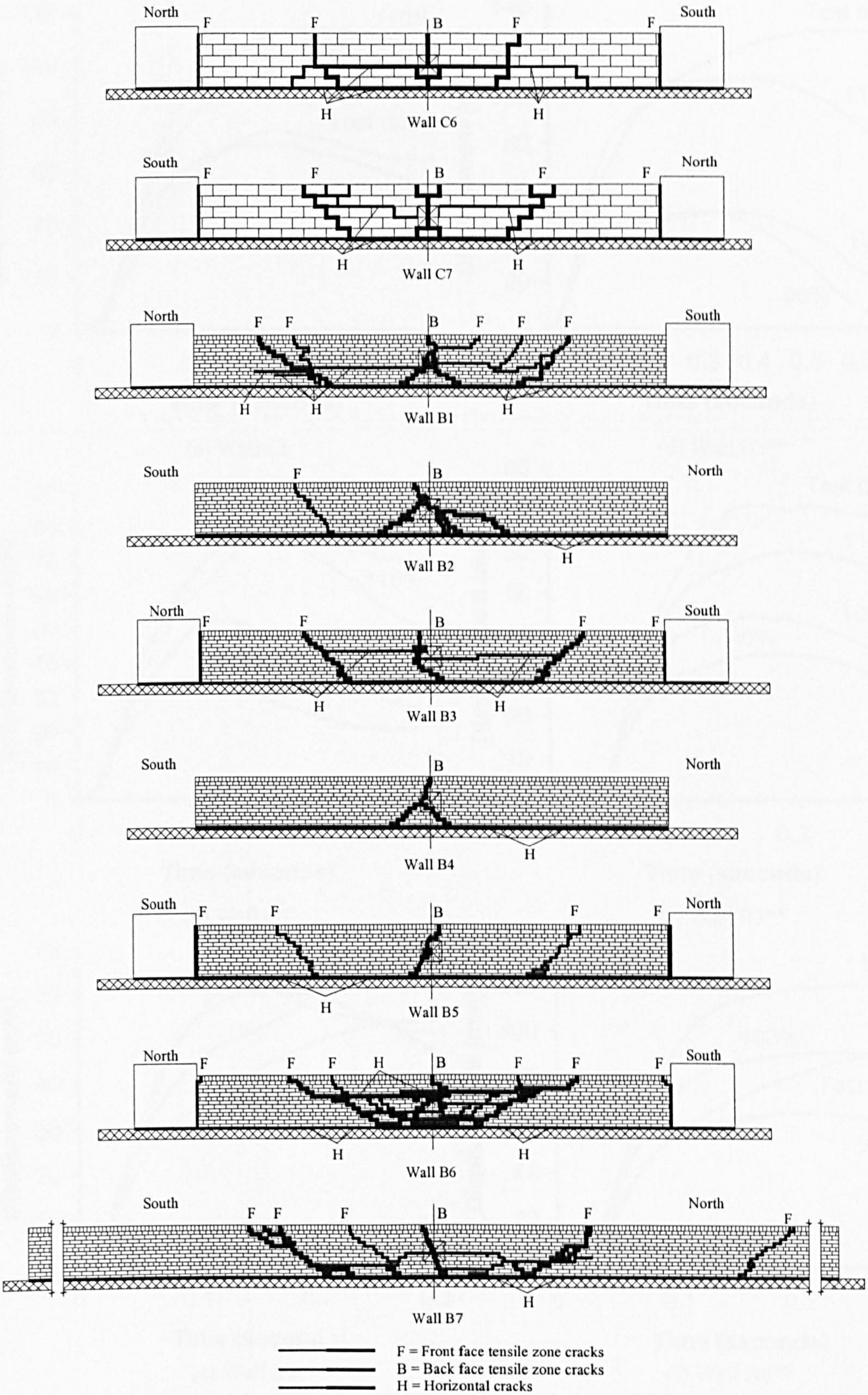

Figure 4-18 Observed post-test crack patterns

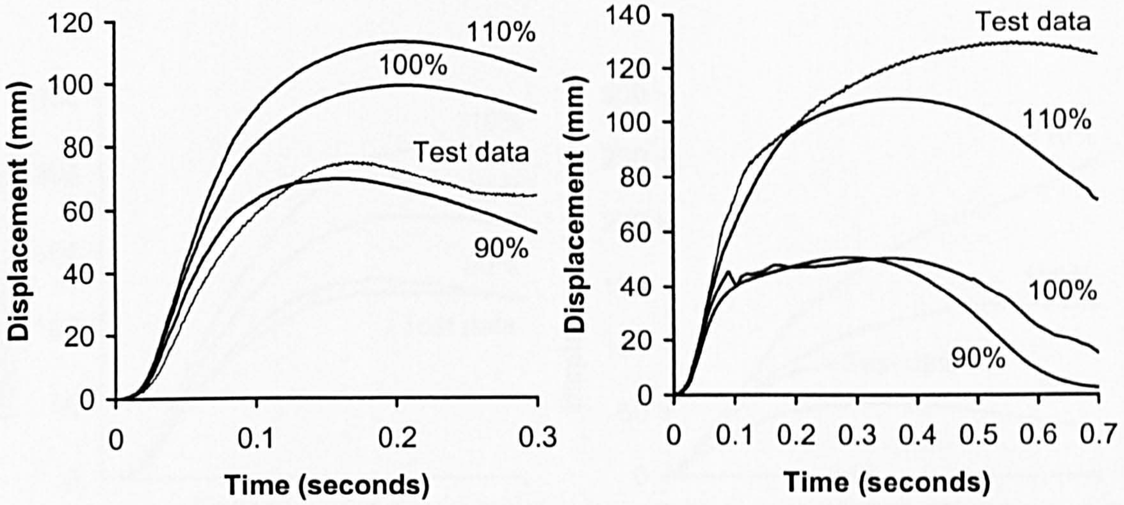

(a) Wall C6

(d) Wall B2**

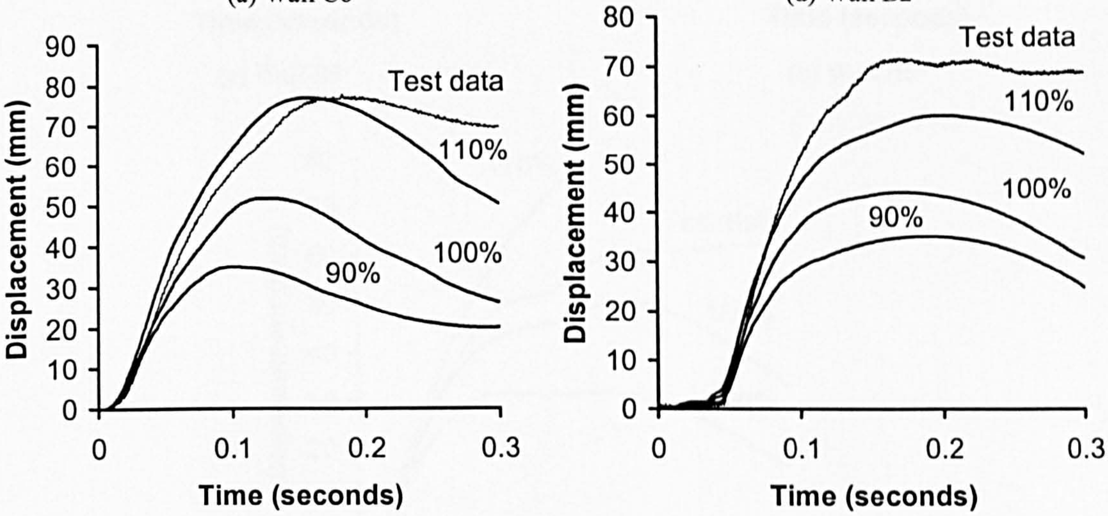

(b) Wall C7

(e) Wall B3**

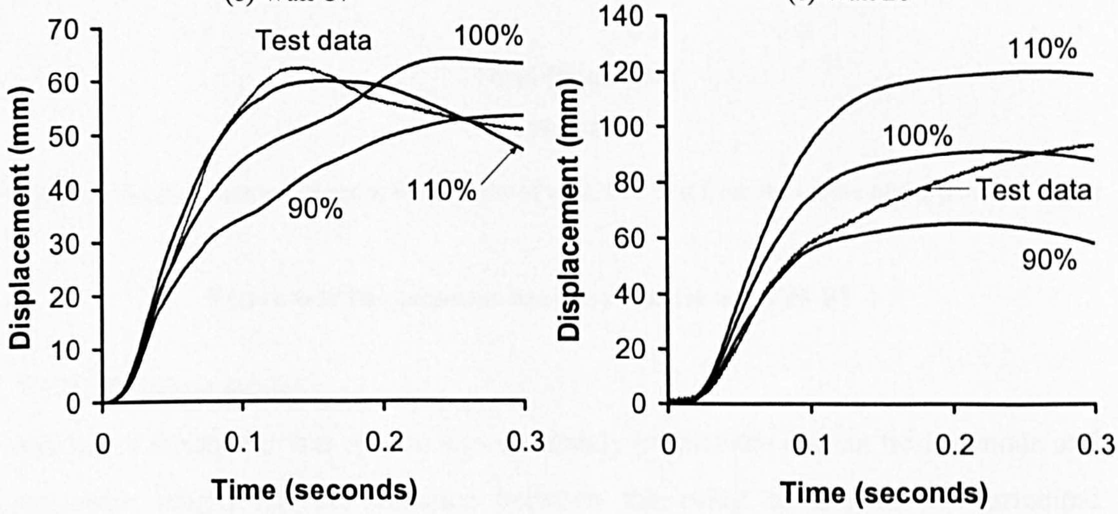

(c) Wall B1*

(f) Wall B4**

* Indicates displacement measured at mid-height of wall, 500 mm from the centre of the point of impact

** Indicates displacement measured 440 mm above base, 115 mm from the centre of the point of impact

Figure 4-19 Displacement-time response for walls C6-B4

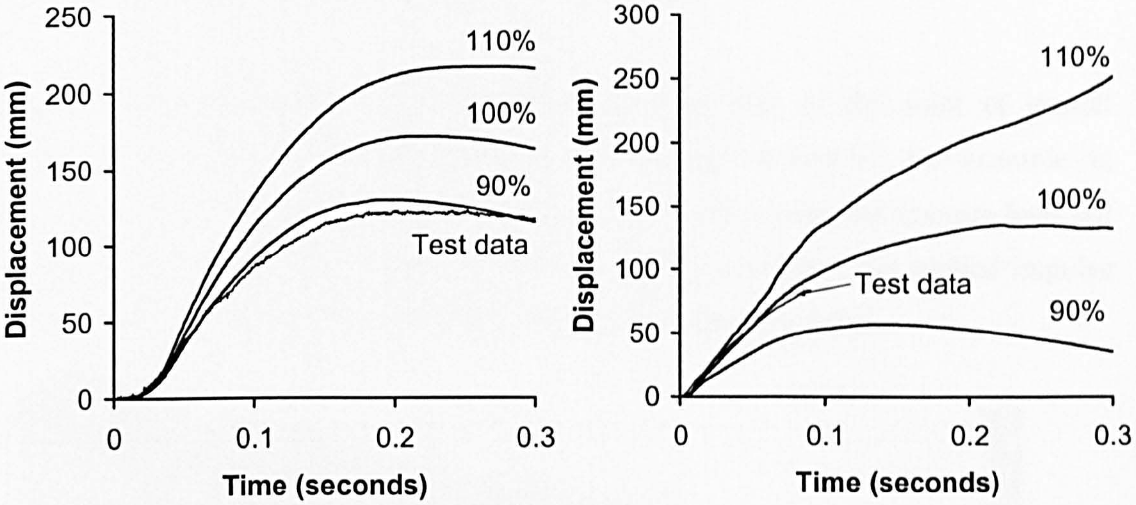

(a) Wall B5

(b) Wall B6*

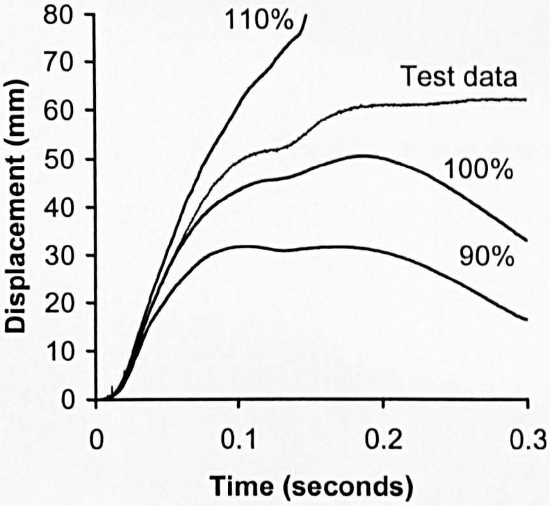

(c) Wall B7*

* Indicates displacement measured at mid-height of wall, 500 mm from the centre of the point of impact

Figure 4-20 Displacement-time response for walls B5-B7

4.4.7 Wall failure modes

In most cases the model was able to approximately predict the correct failure mode and characteristic length i.e. the distance between the point of impact and principal vertical/diagonal crack(s) (Table 4-5). In the case of C7 the model correctly predicted a horizontal and vertical crack to form behind point of impact (Figure 4-15b).

Furthermore, the model was also able to predict the formation of diagonal cracks, typically approximately 2.3 m from the point of impact.

Whether or not diagonal fracture lines formed either side of the point of impact appeared to be influenced by small variations in the applied impulse. For example, in the case of B3, decreasing the applied impulse by 10% led to diagonal fracture lines not forming (Figure 4-21a). Conversely, in the case of B4, increasing the applied impulse by 10% led to the formation of diagonal fracture lines (Figure 4-21b).

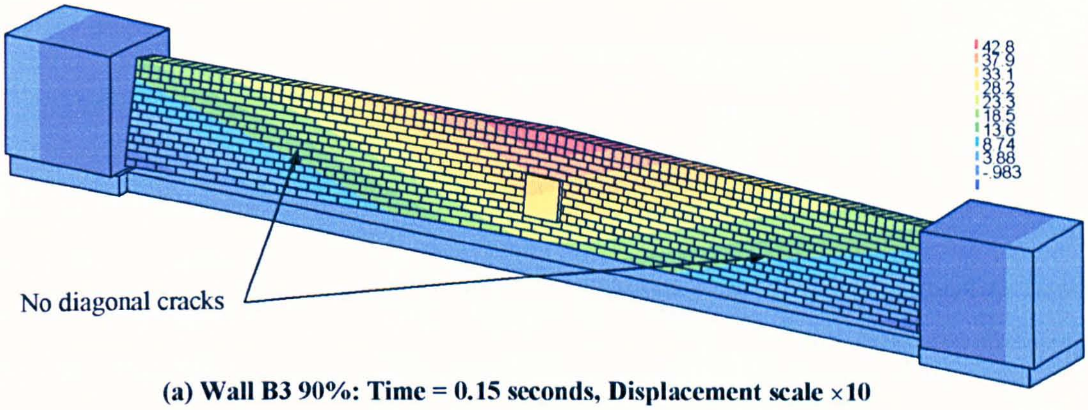

(a) Wall B3 90%: Time = 0.15 seconds, Displacement scale ×10

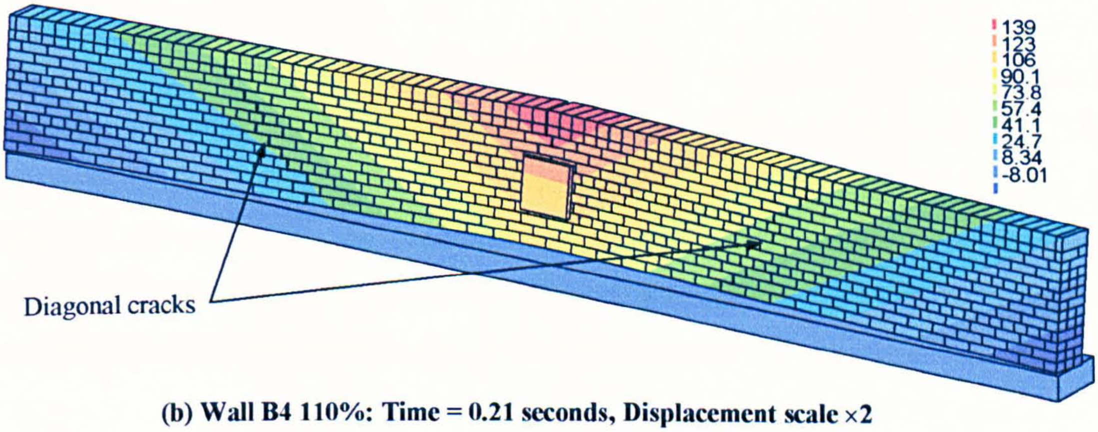

(b) Wall B4 110%: Time = 0.21 seconds, Displacement scale ×2

Figure 4-21 Walls B3 and B4: Out-of-plane displacement (mm) showing influence of impulse on diagonal fracture lines

In the case of B5 the model predicted secondary near vertical fracture lines to form either side of the point of impact (Figure 4-22) but in practice these were diagonal (Figure 4-18). However, the locations of the principal fracture lines, at the interface between the wall ends and abutment blocks, were correctly predicted.

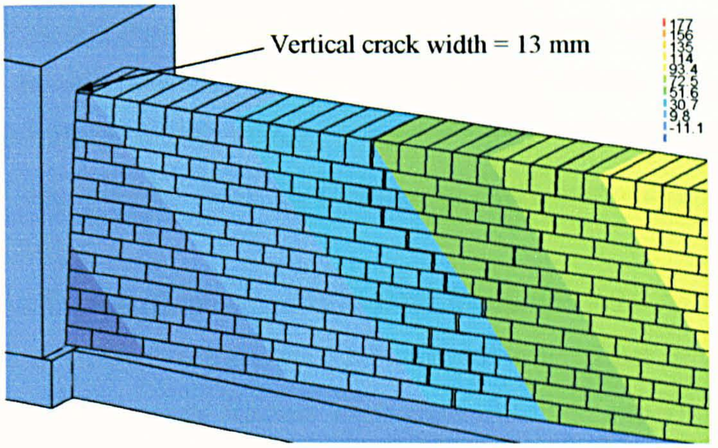

Figure 4-22 Wall B5: Near vertical cracks on impact side of wall (Time = 0.24 seconds, Displacement scale ×3)

4.4.8 Wall displacements

One of the main benefits of a three dimensional model is the ability to determine out-of-plane displacement-time response and predict whether bricks are likely to be ejected from a wall. Therefore, the experimentally recorded displacement-time responses have been compared with the model (Figure 4-19 and Figure 4-20).

As the experimentally recorded force-time histories were likely to be approximate (Gilbert *et al.* 2002b), the loading impulses have been scaled up or down by 10%. The ratio of predicted peak displacement to experimental peak displacement is given in Table 4-5. In most cases the experimentally observed displacement was within the upper and lower bound limits. However, the experimentally recorded displacement was not within the upper and lower bound limits in the case of:

(i) Wall B2 (wall displacements under predicted). The model over predicted the amount of damage behind the point of impact. This led to a more localised failure mode. Less damage was observed to occur experimentally and thus the whole wall was able to rock. The exact proportion of the impulse giving rise to rocking and sliding modes is difficult to predict but it will be demonstrated in the next section that a number of key parameters are highly influential.

(ii) Wall B3 (wall displacements under predicted). Gilbert *et al.* (2002a) reported that the performance of the load attenuator was unsatisfactory in the case of this test. Consequently, stress wave effects may have led to an erroneous force-time record. A similar under prediction occurred when the wall was analysed using the mechanism analysis tool described by Gilbert *et al.* (2002b).

(iii) Wall B5 (wall displacements slightly overpredicted). As noted earlier, near vertical fracture lines were predicted to form either side of the point of impact but diagonal fracture lines were observed experimentally. This may have caused the test wall to dissipate more energy by rocking. However, most of the experimental displacement was due to the opening of vertical fracture lines which were correctly predicted to form between the end of the wall and the abutment blocks.

4.4.9 Sensitivity study

A sensitivity study has been performed on wall B7 to investigate the influence of various parameters: base friction, fracture energy, joint failure stress, joint friction, limit of dilatancy and angle of dilatancy. Each parameter was scaled by 75%, 100% and 125% (100% was taken to be equal to the value given in Table 4-3). The experimentally recorded force-time history for wall B7 is used in this case.

Figure 4-23 shows the model displacement-time response is very sensitive to small changes in some of the key interface parameters. This is particularly true in the case of base friction, fracture energy, joint failure stress and angle of dilatancy. Conversely, the study also shows wall response is reasonably insensitive to joint friction and limit of dilatancy.

In the case of the parameter of base friction the response of the wall when friction is increased from 100% to 125% is particularly interesting. As the wall started to move out-of-plane, there was greater resistance to sliding at the base. Therefore, more horizontal cracks were observed to form in the bed-joints close to the point of impact. Furthermore, the mass of wall resisting the load was significantly reduced because diagonal fracture lines formed closer to the point of impact. This had the effect of increasing out-of-plane displacement.

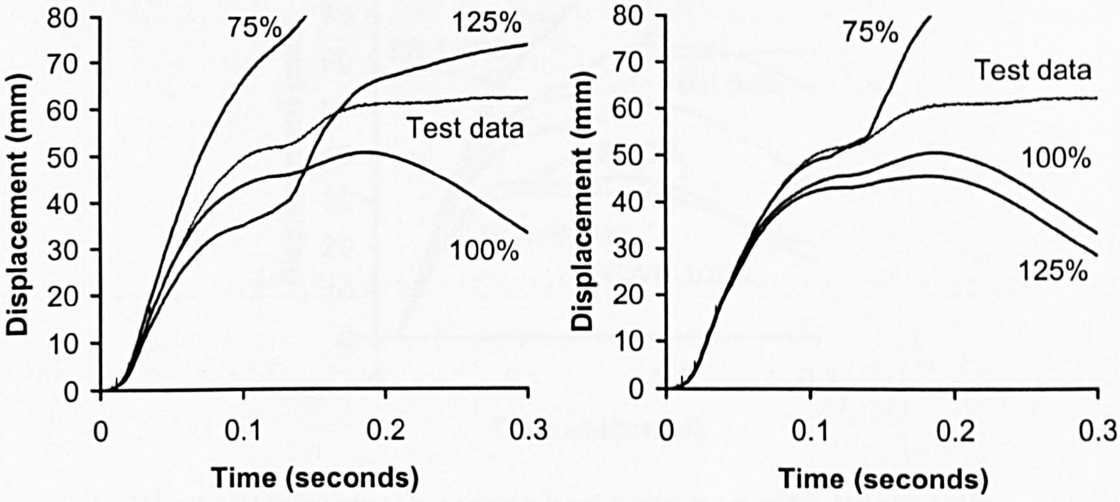

(a) Base friction

(c) Fracture energy

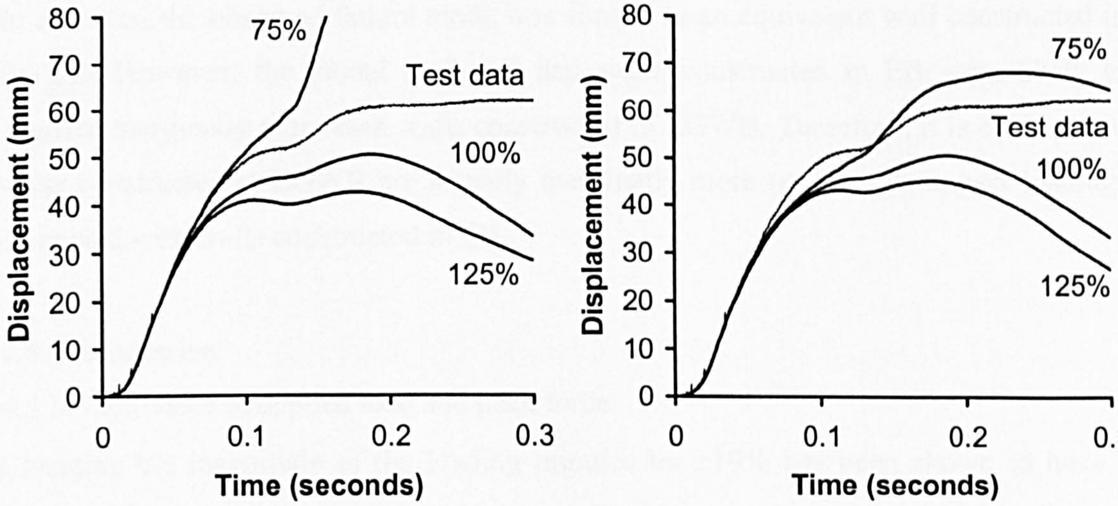

(b) Joint failure stress

(d) Angle of dilatancy

Figure 4-23 Sensitivity study showing influence of base friction, fracture energy, joint failure stress and angle of dilatancy

4.4.10 Influence of bond type

In the UK structural masonry walls and parapets are usually constructed in English Garden Wall Bond (EGWB). However, it is often thought that English Bond (EB) is stronger than EGWB because there is greater through thickness interlocking (headers).

However, there is little experimental or numerical evidence to support this theory. Therefore, in order to investigate the influence of bond type wall model B7 was reconstructed in EB. Results are shown in Figure 4-24.

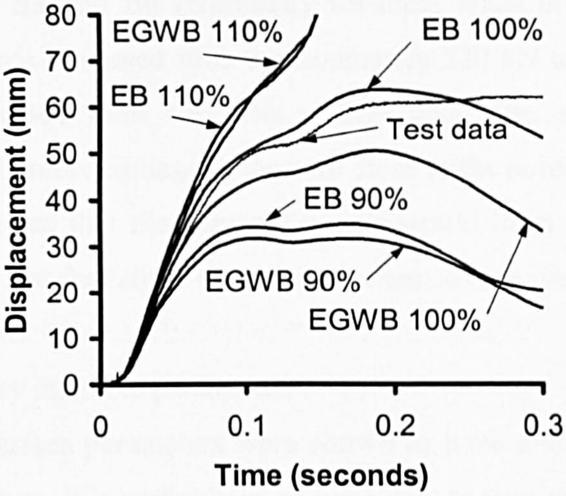

Figure 4-24 Influence of bond type when impulse is scaled 90, 100 and 110%

In all cases, the observed failure mode was similar to an equivalent wall constructed in EGWB. However, the model predicted that walls constructed in EB were likely to displace marginally more than walls constructed in EGWB. Therefore, it is evident that walls constructed in EGWB are actually marginally more resistant to impact loadings compared with walls constructed in EB.

4.5 Discussion

4.5.1 Influence of applied load and peak force

Changing the magnitude of the loading impulse by ±10% has been shown to have a significant influence on the failure mode and displacement-time response. In the case of wall B2 the experimentally observed failure mode appeared close to the transition point between the single and three fracture line mechanisms.

In the model, the diagonal front face cracks required for the three fracture line mechanism were frequently not observed to form when the wall was loaded with 90% of the impulse. However, when the impulse was increased to 100% diagonal cracks started to open up significantly. Increasing the impulse to 110% resulted in diagonal cracks forming closer to the point of impact and crack widths becoming larger. This suggests that the failure mechanism is highly sensitive to small changes in the impulse.

In the case of walls B3 and B6 (nominally identical walls but subject to different loadings) the peak force increased from approximately 320 kN to 420 kN but the total applied impulse decreased from 4.83 kNs to 2.27 kNs. The increase in peak force resulted in significantly more damage to the wall close to the point of impact. Again, the model correctly predicted that the diagonal cracks would form closer to the point of impact. This suggests that the failure mechanism is sensitive to changes in loading rate.

4.5.2 Influence of key interface parameters

A number of key interface parameters were shown to have a significant influence on wall behaviour. However, it is probably more important to note that a small variation in any one of these parameters has the potential to significantly alter the response of a wall.

In a laboratory environment it is possible to determine the interface and material properties with reasonable accuracy. However, it is not uncommon to find that interface parameters vary by 30% or more (Rots 1997). In the field, it is highly unlikely that precise masonry properties will be known for an existing wall or parapet. Furthermore, current field tests (e.g. bond wrench test) are not particularly accurate. Therefore, great care should be taken when attempting to model existing masonry walls and parapets.

4.5.3 Influence of numerical parameters

Mesh size, time step and penalty stiffness did not have a significant influence on the overall response of the model. However, it is important to note that the apparent sensitivity of the model increases dramatically close to the transition point between different failure mechanisms. For example, if a wall is perfectly balanced between rocking over completely and rocking back towards its original position, a small, say 1% change in any of the input parameters will appear to have a significant influence on the overall response. The same logic can be applied to the formation of fracture lines. Therefore, care should be taken when assessing the influence of numerical parameters.

4.6 Conclusions

(i) A masonry specific joint interface model has been successfully implemented in LS-DYNA.

(ii) In most cases, using the proposed modelling strategy allowed the dynamic response of a full-scale masonry wall to be predicted with reasonable accuracy.

(iii) A parametric study showed wall response was highly dependent on small changes in loading impulse, base friction, fracture energy, joint failure stress and angle of dilatancy.

(iv) If the adhesion between individual units is 'poor' then a loose block failure mode is likely. If the adhesion between individual units is 'good' then large panel formation is likely. In this case simple mechanism analysis may be used as a comparatively inexpensive alternative to finite element analysis. However, the finite element model developed is invaluable in finding the transition point between these states.

4.7 Acknowledgements

The support of EPSRC, under grant references GR/M43128, GR/M43135 and GR/M43142 is acknowledged. Also acknowledged is the support of Ove Arup and Partners, who provided LS-DYNA for development purposes during the project.

4.8 References

Beattie (2003); Joint fracture in reinforced and unreinforced masonry under quasi-static and dynamic loading; PhD thesis submitted to Liverpool University, UK.

BS 5628-1 (1992); Code of practice for use of masonry: Structural use of unreinforced masonry, BSI.

Giambanco G, Di Gati L (1997); A cohesive interface model for the structural mechanics of block masonry; Mechanics Research Communications, 24, 503-512.

Gilbert M, Hobbs B, Molyneaux TCK (2002a); The performance of unreinforced masonry walls subjected to low-velocity impacts: experiments; International Journal of Impact Engineering, 27, 231-251.

Gilbert M, Molyneaux TCK, Hobbs B (2002b); The performance of unreinforced masonry walls subjected to low-velocity impacts: mechanism analysis; International Journal of Impact Engineering, 27, 253-275.

Gilbert M, Molyneaux TCK, Hobbs B (1998); A dynamic finite element modelling approach for masonry structures; Proc. British Masonry Society, 8, 182-187.

Hallquist JO (1998); LS-DYNA User Manual; Livermore Software Technology Corporation.

Hallquist JO, Goudreau GL, Benson DJ (1985); Sliding Interfaces with Contact-Impact in Large Scale Langrangian Computations; Computer methods in applied mechanics and engineering, 51, 107-137.

Health and Safety Executive (2002); Obstruction of the railway by road vehicles; Report of the Working Group set up by the Health and Safety Commission, HMSO, ISBN 0717622940.

Huněk I (1993); On a penalty formulation for contact-impact problems; Computers and Structures, 48, 193-203.

Lee JS, Pande GN, Kralj B (1998); A Comparative Study on the Approximate Analysis of Masonry Structures; Materials and Structures, 31, 473-479.

Lofti HR, Shing PB (1994); Masonry Structures; Journal of Structural Engineering, 41, 63-80.

Lofti HR, Shing PB (1991); An Appraisal of Smeared Crack Models for Masonry Shear Wall Analysis; Computers and Structures, 41, 413-425.

Lourenço PB (2000); Aspects Related to the Out-of-Plane Numerical Modelling of Masonry; Masonry International, 14, 31-34.

Lourenço PB, Rots JG, Blaauwendraad J (1998); Continuum Model for Masonry: Parameter Estimation and Validation; Journal of Structural Engineering, 124, 642-652.

Lourenço PB, Rots JG (1997); Multisurface Interface Model for Analysis of Masonry Structures; Journal of Engineering Mechanics, 123, 660-668.

Lourenço PB (1996); Computational Strategies for Masonry Structures, Delft University Press, ISBN 90 407 1221 2.

Middleton WG (1994); Research Project into the Upgrading of Unreinforced Masonry Parapets; Bridge Assessment Management and Design; Ed. Barr, B.I.G. *et al.*, London, Elsevier, 229-234.

Molyneaux TCK, Gilbert M (1997); Modelling masonry joints under impact loading, Proc. Oasys DYNA3D Users Conf, London.

Rots JG (1997); Structural Masonry: An Experimental/Numerical Basis for Practical Design Rules; AA Balkema, Rotterdam, ISBN 90 5410 680 8.

Chapter Five

Reinforced masonry walls subject to out-of-plane car-like impacts: experiments and numerical modelling

Summary

Full-scale reinforced masonry walls were constructed in the laboratory and subjected to out-of-plane car-like impacts at mid-length. The main research objective was to develop novel reinforcement techniques for application to existing and new build masonry walls and parapets. Therefore, some laboratory walls were fitted with conventional bed-joint reinforcement whilst others were reinforced with a specially devised retrofit diagonal bar system.

A long wall containing bed-joint reinforcement failed prematurely as shear planes formed in the bed-joints containing reinforcement. Hence the final out-of-plane displacement was, in this case, greater than in the case of an equivalent unreinforced wall. However, the performance of walls retrofitted with the diagonal bar system was much more satisfactory. Diagonal bars increased interlock between masonry units and prevented bed-joint sliding.

The performance of the tested walls was investigated using a specially modified version of LS-DYNA, a three-dimensional non-linear explicit finite element program. Results showed that displacement-time response was heavily influenced by small changes in the applied load and support conditions.

5.1 Introduction

In the UK, there are tens of thousands of masonry bridge parapets. In recent years, there have been a growing number of high profile incidents involving vehicles impacting unreinforced masonry parapets. In some cases, this has led to bricks being ejected from a wall. This is particularly dangerous if a parapet is situated over a railway line or busy road.

The County Surveyors Society (CSS) in the UK funded a series of actual parapet impact tests on a range of unreinforced masonry walls (Middleton 1994). The tests showed that many walls were able to resist vehicle impact loading at speeds up to 70 mph but there was a high risk of bricks being ejected from the wall.

In addition to the work carried out by the CSS a number of unreinforced walls were tested under laboratory conditions to study the different failure modes resulting from impact loading (Gilbert *et al.* 2002a). Results showed that failure was resisted by the mass of the wall (inertial forces), friction forces acting at the base of the wall and gravity acting to prevent the wall from overturning. It was found that whilst many existing unreinforced walls were likely to be capable of resisting car impacts, others were not. Hence attention turned to identifying methods of upgrading parapet walls by introducing reinforcement.

In previous studies the performance of reinforced masonry has largely focussed on small-scale panels that have been subjected to quasi-static or seismic loads. In recent years many workers have attempted to increase the flexural strength of masonry by bonding fibre reinforced composite materials to the tensile face of a wall or panel (e.g. Hamoush *et al.* 2001). From a purely structural viewpoint, the short term performance of these reinforcing techniques has proved quite successful. However, the long term performance is still unknown.

So far, little consideration has been given to the aesthetic appearance of retrofit reinforcement systems. In many cases, the historic importance of a structure means that reinforcement cannot be simply bonded onto any available surface. In the case of masonry bridge parapets, externally bonded reinforcement systems make a bridge look unsightly and may prove difficult to install if access is restricted. Hence there is a need to develop new reinforcement strategies.

This chapter describes a series of laboratory tests on full-scale reinforced masonry walls that were subjected to out-of-plane car-like impacts at mid-length. The main research objective was to develop novel reinforcement techniques that could be used to reinforce existing masonry walls and parapets. An additional aim of the work was to develop the finite element strategy described in Chapter 4 such that it could also be used to predict the behaviour of reinforced masonry walls.

5.2 Experimental arrangement

5.2.1 Details of test setup and instrumentation

Reinforced brickwork walls were constructed in a laboratory on a 12 mm thick steel plate bolted to a strong floor (Figure 5-1). The surface of the plate was coated with epoxy and sharp sand to provide a rough surface. The walls ranged in length from approximately 9 m to 20 m but thickness and height remained constant at nominally 330 mm and 1090 mm respectively.

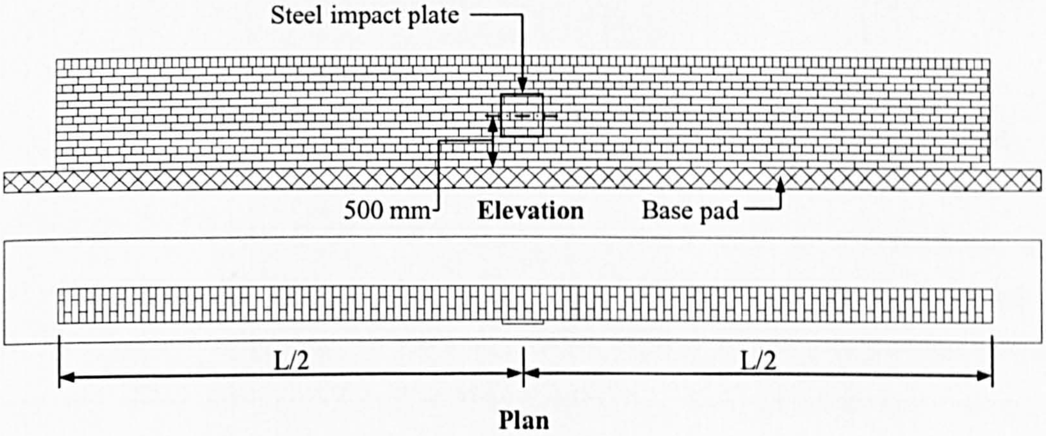

Figure 5-1 Test arrangement showing position of steel impact plate

An out-of-plane car-like impact was applied to each wall at mid-length by using a purpose built impact rig. Full details of the impact rig are given by Gilbert *et al.* (2002a). The impulse characteristics (i.e. duration and peak force) were designed to simulate a 1500 kg car impacting a wall at 20° at speeds in excess of 50 mph. Thus the loading impulse applied to the walls varied from 5 kNs to 8 kNs, with durations in the range 40 ms to 80 ms. A typical loading impulse is shown in Figure 5-2.

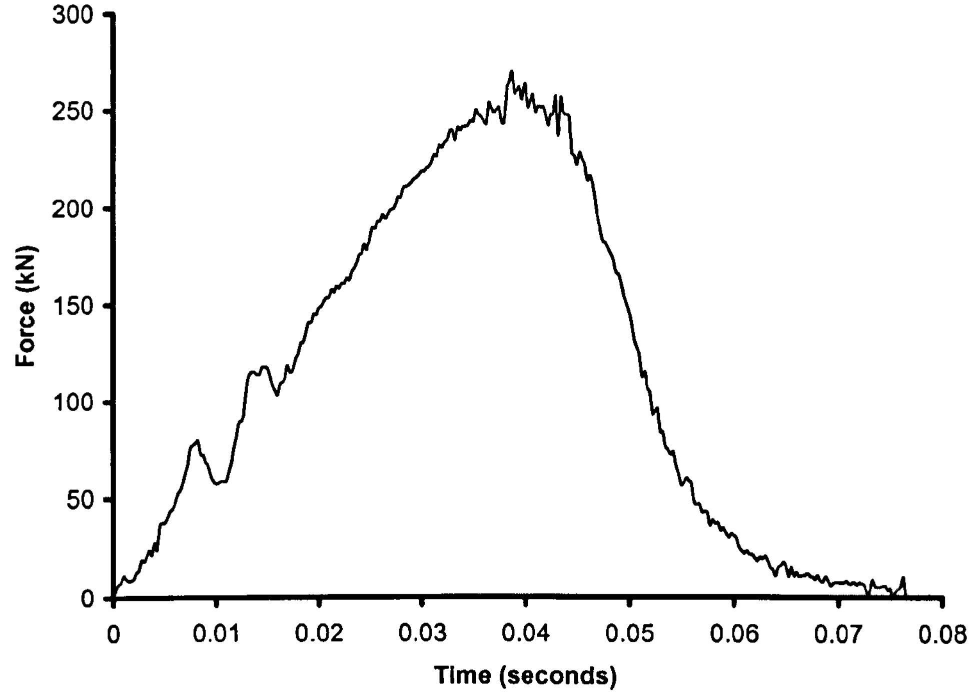

Figure 5-2 Typical experimentally recorded force-time history (taken from wall B8)

Out-of-plane wall displacements were recorded by a series of displacement gauges positioned at 1 m intervals along the impact face of each wall. Most gauges were positioned to record displacements at mid-height although some gauges were positioned at the top of the wall close to the point of impact. Additional displacement gauges were positioned at the ends of the wall to record in-plane movements. The applied impulse was measured by a load cell positioned between the impact rig and loading plate. All instrumentation was monitored by a high speed PC-based data acquisition system with a minimum sampling rate of 4 kHz.

5.2.2 Details of test walls

The walls were constructed using Marshalls' solid red smooth Accrington Nori clay engineering bricks (class B) with either a class (iii) mortar to BS 5628(i) (1:1:6 cement:lime:sand) or a class (iv) mortar (1:2:9). The walls were 13 courses high with a brick on edge capping layer. English garden wall bond was used throughout and impact testing took place at nominally 28 days. Construction details are summarised in Table 5-1.

Table 5-1 Details of test walls

Wall ref:	Mortar	Length (mm)	Breadth (mm)	Height (mm)	End Condition	Rein-forcement	Remarks
B8	Class (iii) (1:1:6)	19540	330	1090	2 × free	None	
RB8	Class (iii) (1:1:6)	19540	330	1090	2 × free	6mm Stainless, each face, top of courses 1, 3, 5, 7, 9, 11, & 13	
RB9	Class (iii) (1:1:6)	9600	330	1090	2 × simple supports	6mm Stainless, each face, top of courses 1, 3, 5, 7, 9, 11, & 13	
RB10	Class (iii) (1:1:6)	9120	330	1090	2 × free	6mm Stainless, each face, top of courses 1, 3, 5, 7, 9, 11, & 13	
RB11	Class (iii) (1:1:6)	9600	330	1090	2 × simple supports	2 x 6 mm stainless each face, top of courses 1, 2, 3, 4, 5, 6, 7, 8, 9, 10, 11, 12 & 13	4 × RB9 reinforcement
RB13	Class (iii) (1:1:6)	19540	330	1090	2 × free	See Figure 5-3	
RB14	Class (iii) (1:1:6)	19540	330	1090	2 × free	See Figure 5-3	
RB15	Class (iv) (1:2:9)	19540	330	1090	2 × free	See Figure 5-3	Weak mortar
B15	Class (iv) (1:2:9)	19540	330	1090	2 × free	None	Weak mortar

Walls B8 and B15 were unreinforced in order to act as a reference for the reinforced walls. Walls RB15 and B15 were constructed using a weak mortar in an attempt to simulate the response of an existing wall or parapet that had either been constructed using a weak mortar or had been weakened by environmental conditions.

Bed-joint reinforcement was used to reinforce walls RB8, RB9, RB10 and RB11. The reinforcement consisted of 6 mm diameter deformed stainless steel bars (460 grade to BS 6744). The bars were positioned along two centre lines, 50 mm in from the front and back face of the wall.

RB13 and RB15 were reinforced using a specially designed diagonal bar reinforcement system (Figure 5-3). A total of 46 No. high yield steel bars (20 mm diameter) were inserted into pre-drilled holes inclined at 45°. The deformed bars were fixed in position using a proprietary (Hilti) epoxy resin based grout. RB14 was reinforced with the same diagonal bar system but the 20 mm diameter high yield steel bars were replaced by 22 mm diameter Fibregrip Polyester bars (manufactured by Fibreforce).

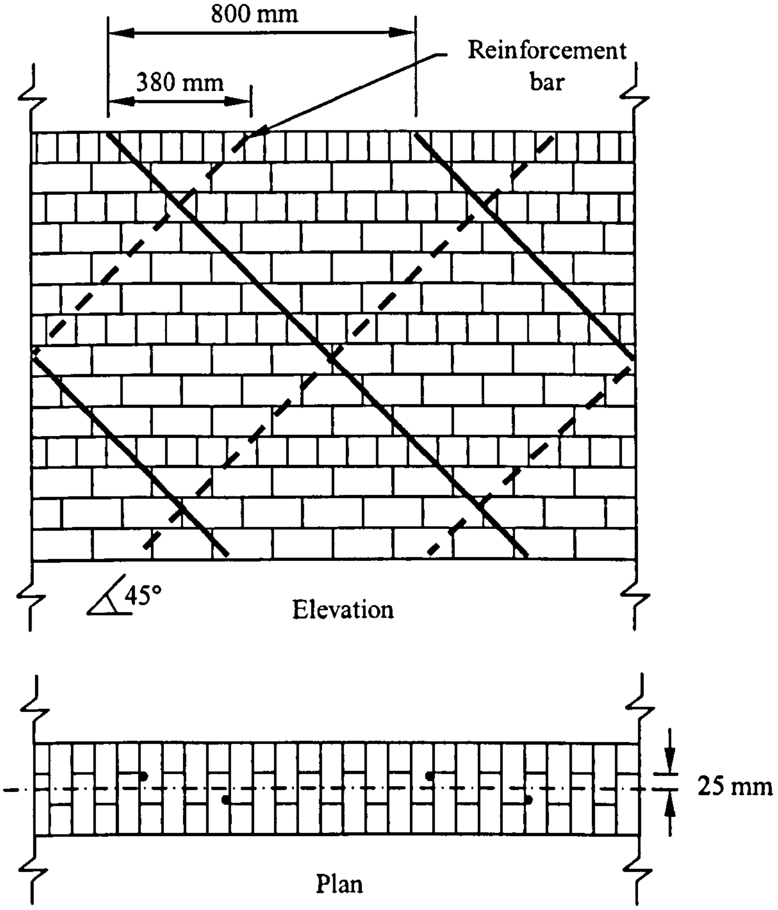

Figure 5-3 Detail showing diagonal bar reinforcement system

Previous experimental work by Gilbert *et al.* (2002a) showed that rocking dissipated a large proportion of the applied energy. The influence of rocking has been studied in the current work by adding vertical simple supports to walls RB9 and RB11. The supports were constructed from steel box sections bolted to the strong floor.

5.3 Experimental results

Details of the loading applied to each wall are shown in Table 5-2.

Figure 5-4 shows post-test shear and tensile crack patterns recorded on the impact side of the wall. The total recorded impulse was generally similar to the theoretical applied impulse. However, in the case of wall B8 the recorded impulse was 17% greater than the estimated applied impulse. In this case, the force-time history may have been incorrectly recorded. In the case of walls RB9, RB10 and RB14 a small secondary impact was observed, approximately 100 ms after the main impact.

Table 5-2 Details of applied loading and failure mode type

Wall ref:	Drop height (m)	Mass (kg)	Appox. Peak force (kN)	Applied impulse^A (kNs)	Recorded/applied impulse
B8	1.27	1500	256	7.49	1.17
RB8	1.27	1500	228	7.49	0.88
RB9	1.27	1220	251	6.09	1.33
RB10	1.00	1220	228	5.40	1.17
RB11	1.27	1220	236	6.09	1.01
RB13	1.27	1500	225	7.49	1.00
RB14	1.27	1500	225	7.49	1.10
RB15	1.27	1500	233	7.49	1.00
B15	1.27	1500	B	7.49	B

A Assuming zero rebound and 100% of free fall velocity, to top of specimen. Mass of quadrant neglected.
B Data lost

Wall B8

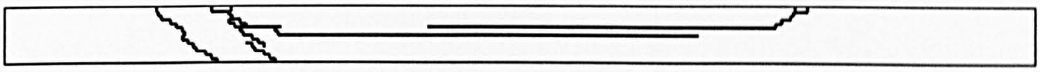

Wall RB8

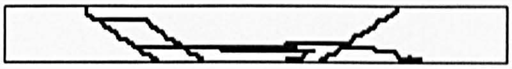

Wall RB9

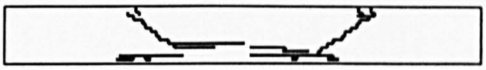

Wall RB10

Wall RB11

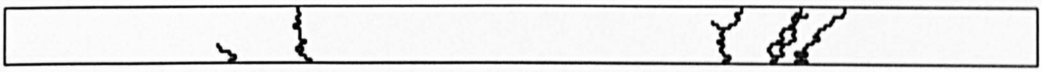

Wall RB13

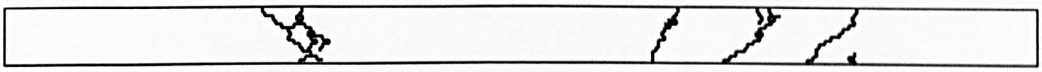

Wall RB14

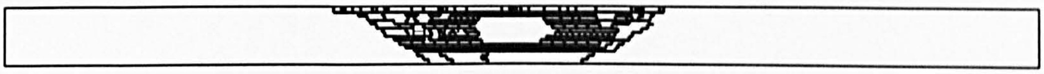

Wall B15

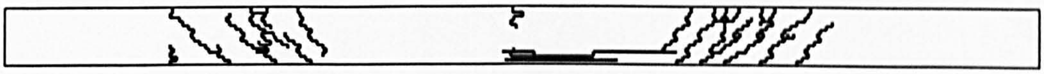

Wall RB15

Figure 5-4 Observed post-test front face crack patterns (All walls were impacted at mid-length, 500 mm above the base)

5.4 Analysis of results

5.4.1 Introduction to finite element modelling

The test walls were modelled using a commercially available finite element code with the addition of a masonry specific joint interface model. Full details of the numerical modelling strategy described are given in Chapter 4 and only a brief description is presented here.

A masonry specific discrete-crack type model has been implemented in LS-DYNA, a non-linear explicit finite element code. The overall modelling strategy is similar to that described by Rots (1997) who used an implicit solution strategy to model the quasi-static in-plane behaviour of masonry. However, it is important to note that a penalty stiffness contact algorithm has been used here instead of explicit interface elements, to model the joints. Additionally, the formulation is fully three-dimensional.

No attempt has been made to model explicitly the mortar between the bricks. Instead, geometrically expanded masonry units were meshed with solid elements which were given composite brick-mortar properties. Key features of the joint interface model include:

(i) Mohr-Coulomb failure criterion and tension cap.
(ii) Post-peak softening branch following initial fracture.
(iii) Dilatant friction.

5.4.2 Interface parameters

As a starting point to the modelling work a penalty stiffness formulation is used to calculate the interface stresses (Hallquist 1998, Hallquist *et al.* 1985). Using this formulation, surfaces of adjacent bricks are defined with either ‘slave’ or ‘master’ properties. Before the onset of fracture, slave surface nodes are tied to the master surface of an adjacent brick. This is achieved by applying a restoring force or penalty stiffness to a slave node that becomes displaced from its initial position on the master surface. In order to restrict penetrations between adjacent bodies the penalty stiffness has to be sufficiently high. Results from a parametric study carried out on an unreinforced wall suggest that a penalty stiffness value of 64000 N/mm is likely to give reasonable results.

Once the penalty formulation has calculated the nodal forces, shear and normal interface stresses can then be determined from the contact area associated with each node. The interface stresses are then compared with a predefined failure surface which is described by a Mohr-Coulomb friction relationship (Figure 5-5).

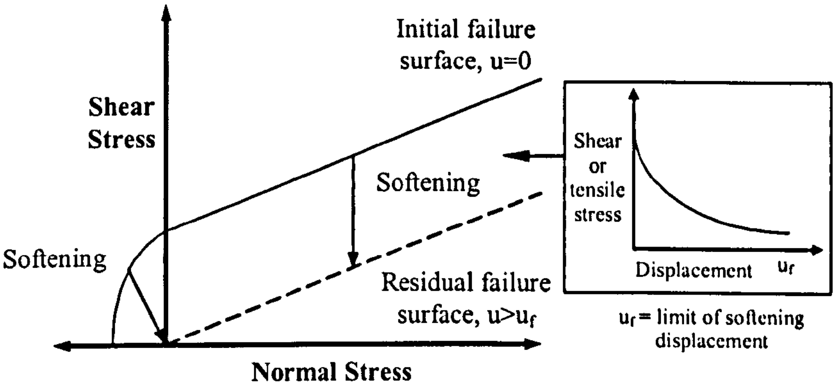

Figure 5-5 Failure envelope for a masonry joint

An exponential displacement softening relationship is used for tied nodes that fail in tension (mode I) or shear (mode II). The residual failure surface is for convenience deemed to have been reached when the separation is such that the exponential softening curve indicates only 0.1% of the maximum (initial failure) shear/tensile stress can be transmitted. Thus, the tensile and shear residual displacements u_f can be calculated from the mode I and mode II fracture energies and the shear and tensile joint failure stresses.

When masonry fails in shear, displacements which occur parallel to the joint may be accompanied by displacements perpendicular to the joint respectively δu and δv (Figure 5-6). The angle of dilatancy ϕ is $\tan^{-1}(\delta u/\delta v)$ and can be estimated from a plot of tangential displacement against normal displacement. Typical measured values of $\tan\phi$ are in the range 0.1 to 0.7 depending on the roughness of the unit surface (Rots 1997). Low confining stress tends to allow a high angle of dilatancy whilst high confining stress tends to give rise to a low value of dilatancy. As the joint slides the angle of dilatancy decreases to zero because the unit surface becomes smoother.

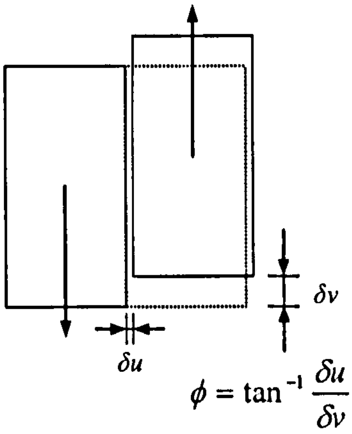

Figure 5-6 Displacement parallel and perpendicular to joint during shear failure

A bilinear model has been used to describe dilatant friction (Figure 5-7). Similar models have been proposed by Giambanco & Gati (1997). Each slave node is assumed to lie in a depression in the joint. Initial resistance to sliding is purely due to unit-mortar bond strength, Coulomb sliding and dilatant friction. When a slave node is displaced from its original position on the master surface it is constrained to move in a direction governed by the angle of dilatancy because movement purely parallel to the interface is interpreted as a penetration according to the penalty stiffness method.

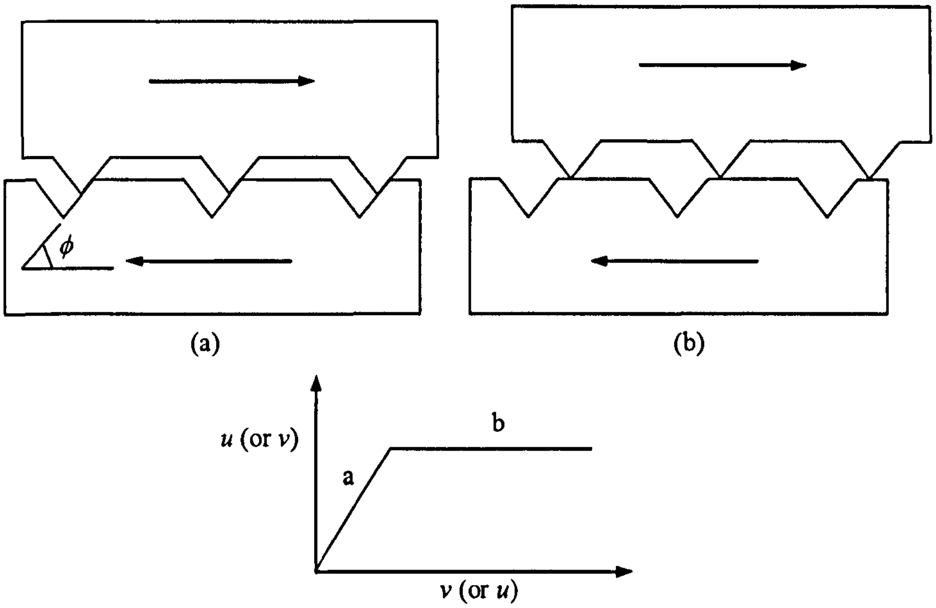

Figure 5-7 Bilinear model showing angle of dilatancy

5.4.3 Validation of proposed modelling strategy

Chapter 4 showed that the proposed modelled strategy could be used to predict the response of full-scale unreinforced masonry walls with reasonable accuracy. In many cases the fracture lines predicted by the model were remarkably similar to those observed experimentally. Furthermore, it was also shown that results from the model were not greatly influenced by numerical parameters such as mesh size, time-step or penalty stiffness.

The model described previously will now be applied to the reinforced walls tested in the laboratory. Each physical brick unit in a given laboratory wall was modelled numerically using 4x3x3 (LxBxH) 8-noded solid elements with an elastic material model. Single point integration was used with viscous hourglass control. Gravity was applied to the model using the method of dynamic relaxation.

Horizontal bed-joint reinforcement (in the case of wall models RB8, RB9, RB10 and RB11) was modelled using thin shell elements with an elastic-plastic material model.

The shell elements were positioned in the bed-joints between masonry courses. The centreline of the shell elements was designed to coincide with the actual positions of the reinforcement whilst the width of the elements was taken to be equal to the circumference of the bars. Only one side of the shell elements was attached to the surfaces of the solid elements making up the masonry units.

Diagonal bar reinforcement (wall models RB13, RB14 and RB15) was modelled using Hughes-Liu beam elements and either an elastic-plastic or rigid material model. Figure 5-8 shows the position of five beam elements at a horizontal interface between four bricks. Elements 1-2 and 5-6 are connected to the interface by elements 2-3 and 4-5. For clarity, elements 2-3 and 4-5 are shown offset from element 2-5. However, in the model they were coincident with element 2-5. The length of elements 2-3 and 4-5 was set at 5 mm.

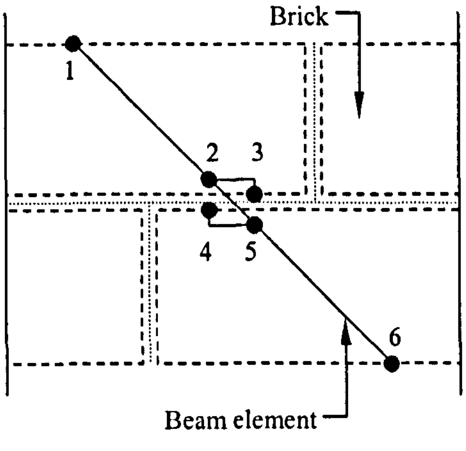

Figure 5-8 Location of beam elements at an interface between four bricks (exploded view)

The impact plate and vertical supports (wall models RB9 and RB11) were modelled using 8-noded solid elements and a rigid material model. The base pad has been modelled using 8-noded solid elements and an elastic material model.

5.4.4 Material and interface data used in numerical models

Some of the material and interface data used in the models has been obtained from an extensive small-scale test programme (Beattie 2003). The main aim was to determine the basic engineering properties of the constitutive materials used in the full-scale wall tests (Table 5-3).

Table 5-3 Properties of laboratory walls

Property	Value	Comment
Base-mortar interface		
Coefficient of sliding friction	0.725	Total base friction = 0.85 (sliding friction + dilatancy) (Gilbert *et al.* 2002a)
Shear strength	0.2 N/mm^2	Measured on steel base plate in laboratory (Gilbert *et al.* 2002a)
Tensile strength	0.143 N/mm^2	Estimate, based on measured steel base plate shear strength above.
Brick-mortar interface		
Shear strength	0.63 N/mm^2	Determined from 57 triplet tests (Beattie 2003)
Tensile strength	0.45 N/mm^2	Determined from 18 tension tests (Beattie 2003 & Chapter 3)
Mode II fracture energy	0.059 N/mm	Determined from 57 triplet tests (Beattie 2003)
Mode II ultimate displacement	0.65 mm	Determined from 57 triplet tests (Beattie 2003)
Mode I fracture energy	0.01 N/mm	Value taken from experimental work by Rots (1997)
Mode I ultimate displacement	0.15 mm	See below
Coefficient of dilatancy (tanϕ)	0.125	Determined from 4 shear tests (Beattie 2003)
Limit of dilatancy	0.8 mm	Determined from 4 shear tests (Beattie 2003)
Coefficient of sliding friction	0.78	(Beattie 2003)
Brickwork composite		
Density	2200 kg/m^3	
Elastic modulus	20 kN/mm^2	
Poisson's ratio	0.3	
Blockwork composite		
Density	2295 kg/m^3	
Elastic modulus	20 kN/mm^2	
Poisson's ratio	0.3	

Most of the additional material data on the reinforcement bars was supplied by a manufacturer. However, further laboratory tests were required to determine the yield stress, elastic modulus and hardening modulus of the steel bars. This data are reported in Table 5-4.

Table 5-4 Properties of bed-joint reinforcement used in models RB8, RB9, RB10 and RB11

Property	Value
Steel reinforcement bar	
Density	7800 kg/m^3
Elastic modulus	160 kN/mm^2
Hardening modulus	22 kN/mm^2
Poisson's ratio	0.3
Yield stress	330 N/mm^2
Reinforcement-mortar interface	
Shear strength	2.08 N/mm^2

Wall models for B8, RB8, RB9, RB10 and RB11 used the same material and interface data reported in Table 5-3 and Table 5-4. Wall models B15 and RB15 were constructed with a weak mortar that was assumed to have a shear and tensile failure stress equal to 75% of the values reported in Table 5-3 (no physical tests on specimens built using the class iv mortar were conducted).

In the case of models of walls RB13, RB14 and RB15 it was found that use of reinforcement material data reported in Table 5-4 would lead to a very small model time step, governed by the beam elements. Therefore, initially the reinforcement was modelled at two extremes: (i) a rigid material and (ii) an elastic-plastic material with modulus 80 times lower than the actual modulus. In addition, to ensure the failure strain was consistent with the real failure strain the yield stress was also scaled down by a factor of 80. Clearly these are extremes and the properties of the reinforcement will lie somewhere in between. Revised material properties are given in Table 5-5. Note that the rigid material model requires data for elastic modulus and Poisson's ratio in order to calculate sliding interface parameters.

Table 5-5 Properties of diagonal bar reinforcement used in models RB13, RB14 and RB15

Property	**Value**	
	Rigid	**Modified elastic**
Steel reinforcement bar		
Density	7800 kg/m^3	7800 kg/m^3
Elastic modulus	160 kN/mm^2	2 kN/mm^2
Poisson's ratio	0.3	0.3
Yield stress	N/A	4.13 N/mm^2
Hardening modulus	N/A	275 N/mm^2
Fibregrip reinforcement bar		
Density	1500 kg/m^3	1500 kg/m^3
Elastic modulus	47 kN/mm^2	0.47 kN/mm^2
Poisson's ratio	0.3	0.3
Yield stress	N/A	8.5 N/mm^2
Hardening modulus	N/A	1 N/mm^2
Reinforcement-brick interface		
Shear strength	2.08 N/mm^2	

Properties for the impact plate, vertical supports (wall models RB10 and RB11) and base pad are given in Table 5-6.

Table 5-6 Properties of impact plate, vertical supports and base pad

Property	Value
Steel impact plate and vertical supports	
Density	7800 kg/m^3
Elastic modulus	200 kN/mm^2
Poisson's ratio	0.3
Steel-brick interface	
Coefficient of friction	0.3
Concrete base pad	
Density	2371 kg/m^3
Elastic modulus	40 kN/mm^2
Poisson's ratio	0.3

5.4.5 Validation of numerical model against experimental results

Predicted crack patterns are shown in Figures 5-9, 5-10 and 5-11. For all walls, these may usefully be compared with experimentally observed post-test crack patterns for brickwork and blockwork walls which are shown in Figure 5-4. Figure 5-12 and Figure 5-13 show the out-of-plane displacement-time response of the walls. Unless otherwise stated, displacements shown are those recorded by a gauge positioned at mid-height of wall, 360 mm from the centre of the loading plate.

Table 5-7 gives details of the experimentally observed and predicted characteristic failure length for a given mode and peak out-of-plane displacement. The characteristic failure length is defined by the distance between the point of impact and principal vertical/diagonal crack(s). Peak displacements have been taken from the displacement-time data shown in Figure 5-12 and Figure 5-13.

Table 5-7 Summary of test and model results

Wall ref:	**Test: approximate length of failure mode (m)**	**Model: approximate length of failure mode (m)**	**Test: peak displacement (mm)**	**Model: peak displacement (mm)**	**Peak model displacement/ Peak test displacement (Impulse scaled, 90%:100%:110%)**
B8	3.1	2.9	162	235	1.01:1.45:Punched through
RB8	5.3	4.0	174	80	0.36:0.46:0.56
RB9	2.6	Dispersed cracks	63	81	1.03:1.29:1.63
RB10	1.9	Dispersed cracks	184	102	0.43:0.55:0.72
RB11	Varies	Dispersed cracks	43	62	1.26:1.44:1.84
RB13	0.5-6.6		90	130 (134)	1.04:1.44 (1.49):1.73
RB14	4.0-6.6		115	139 (148)	0.90:1.21 (1.29):1.52
RB15	3.8-6.2		127	162 (163)	0.87:1.28 (1.28):1.91
B15	2.4	2.6	Punched through	Punched through	N/A

Figures in brackets indicate rigid material model used for reinforcement

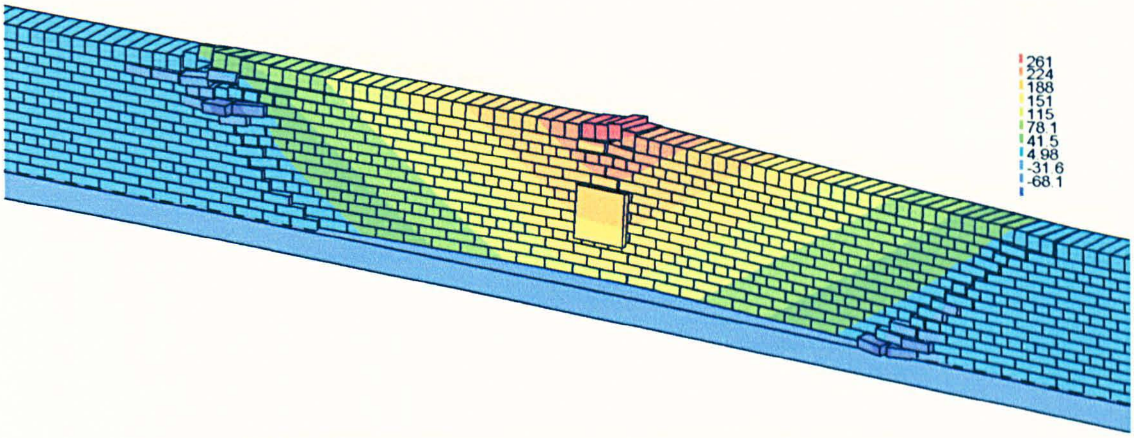

(a) **Wall B8: Time = 0.27 seconds, Displacement scale ×1**

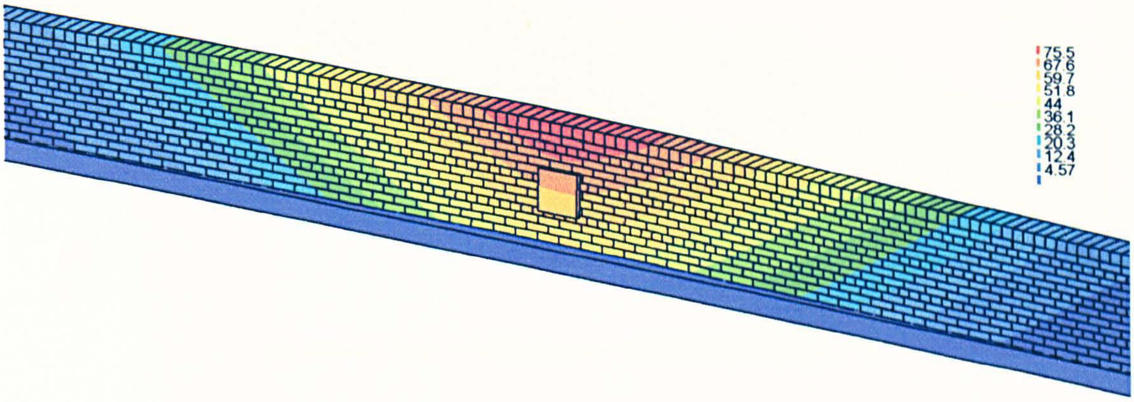

(b) **Wall RB8: Time = 0.12 seconds, Displacement scale ×2**

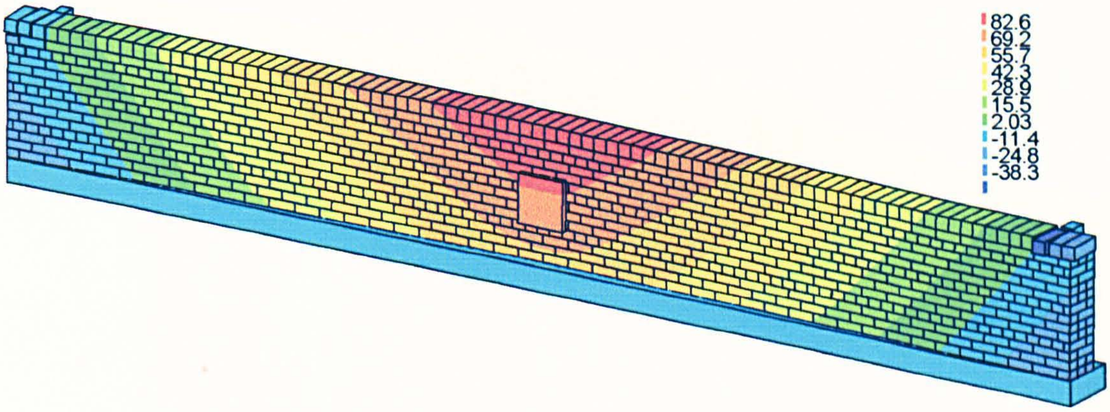

(c) **Wall RB9: Time = 0.21 seconds, Displacement scale ×1**

Figure 5-9 Walls B8-RB9 (100% impulse): Out-of-plane displacement (mm)

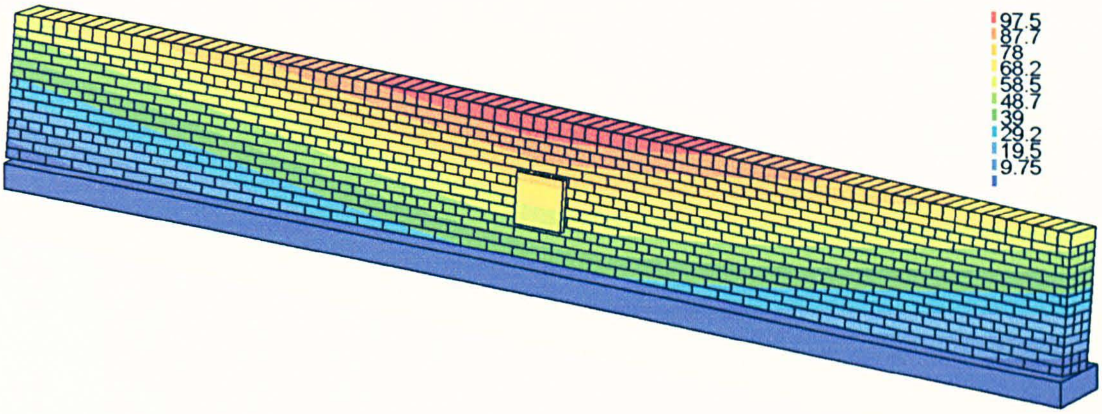

(a) Wall RB10: Time = 0.3 seconds, Displacement scale ×2

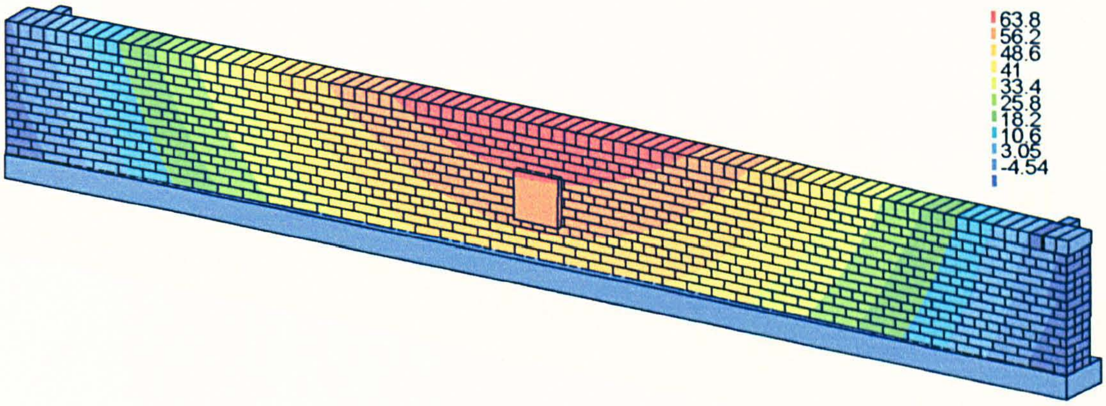

(b) RB11: Time = 0.12 seconds, Displacement scale ×1

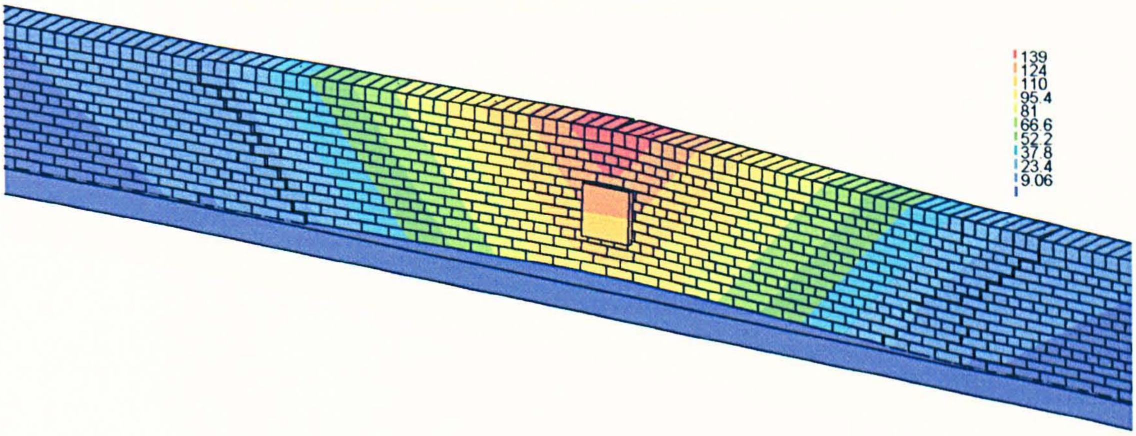

(c) Wall RB13: Time = 0.18 seconds, Displacement scale ×2

Figure 5-10 Walls RB10-RB13 (100% impulse): Out-of-plane displacement (mm)

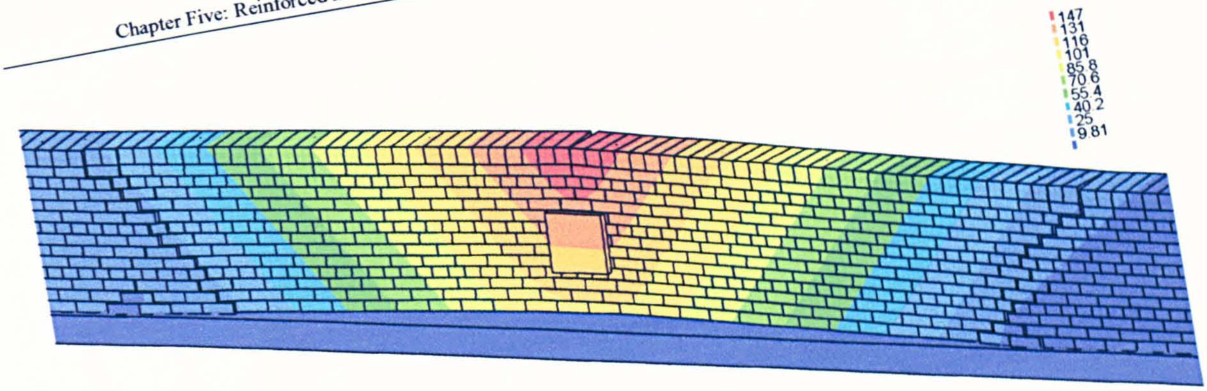

(a) Wall RB14: Time = 0.21 seconds, Displacement scale ×2

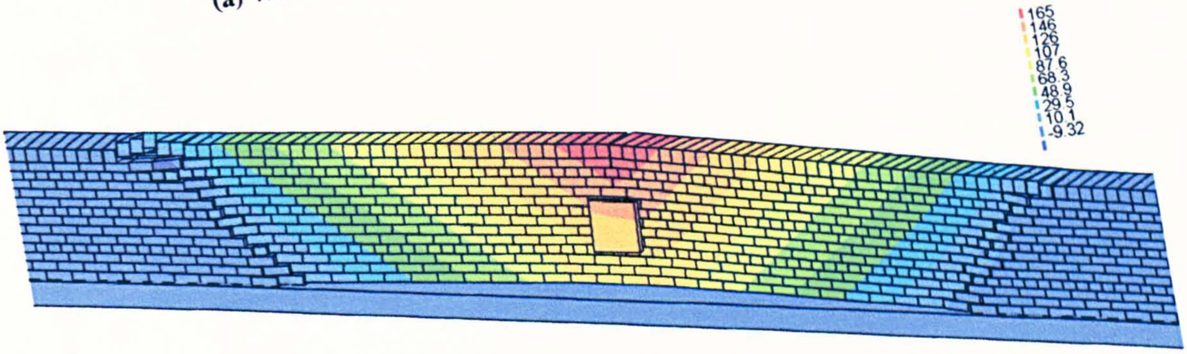

(b) Wall RB15: Time = 0.21 seconds, Displacement scale ×2

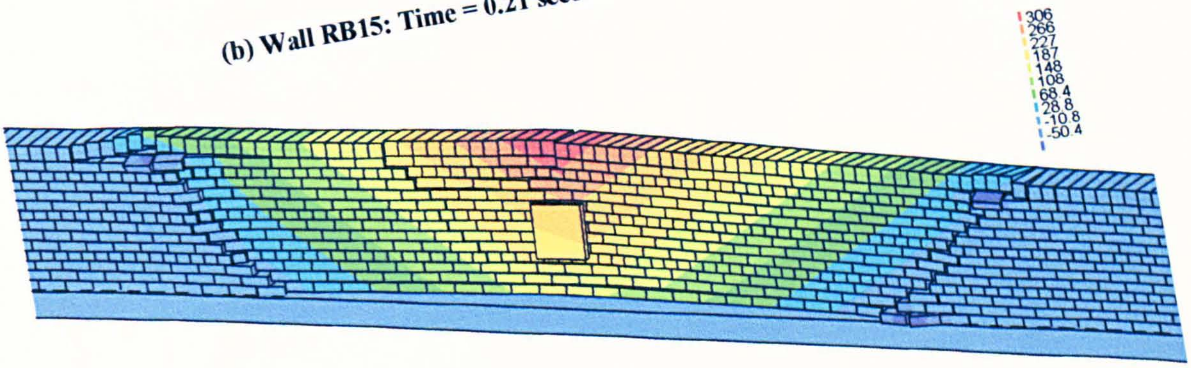

(c) Wall B15: Time = 0.21 seconds, Displacement scale ×1

Figure 5-11 Walls RB14-B15 (100% impulse): Out-of-plane displacement (mm)

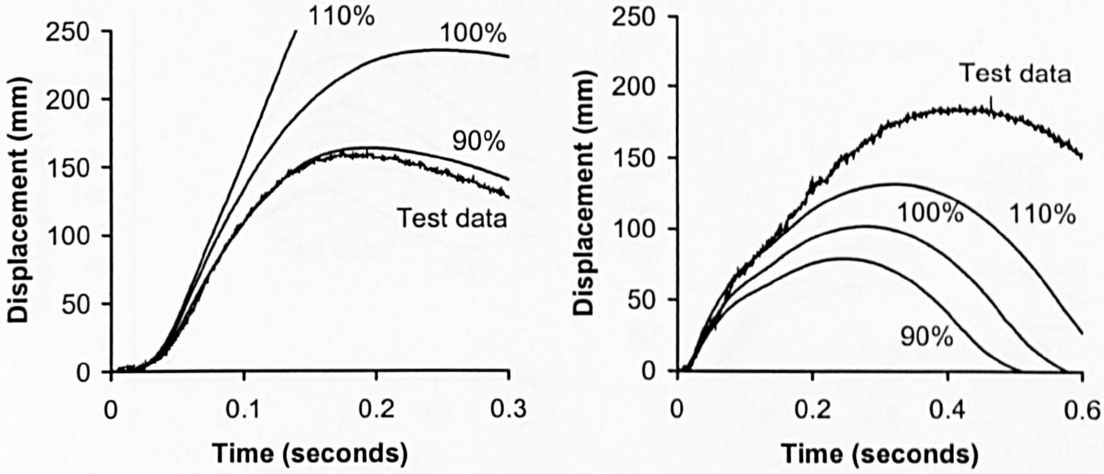

(a) Wall B8* (d) Wall RB10*

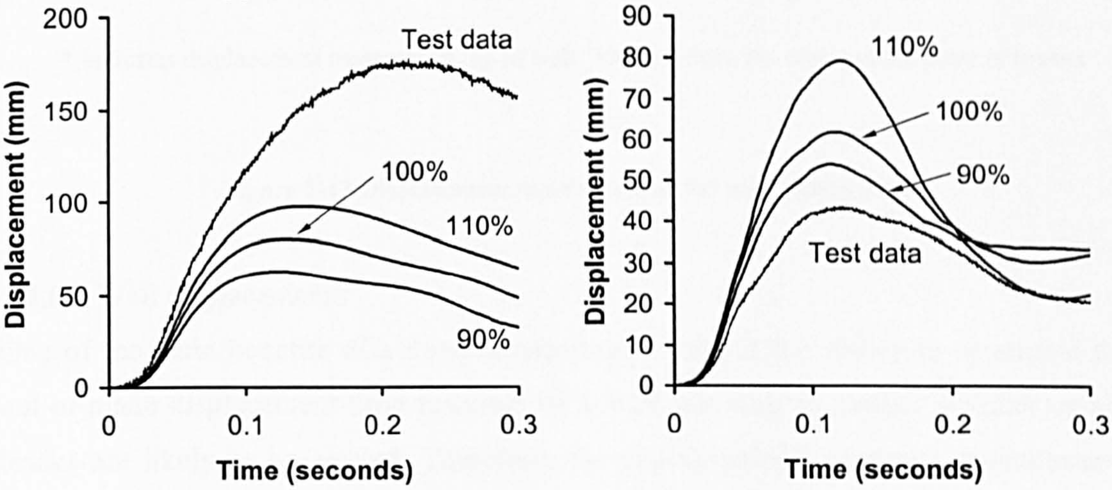

(b) Wall RB8* (e) Wall RB11

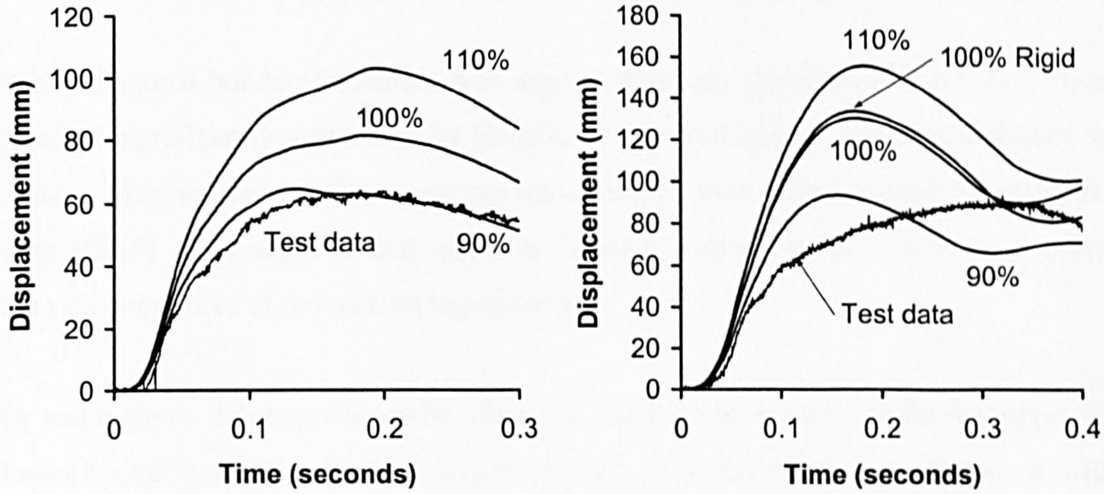

(c) Wall RB9 (f) Wall RB13*

* Indicates displacement measured at top of wall, 360 mm from the centre of the point of impact

Figure 5-12 Displacement-time response for walls B8-RB13

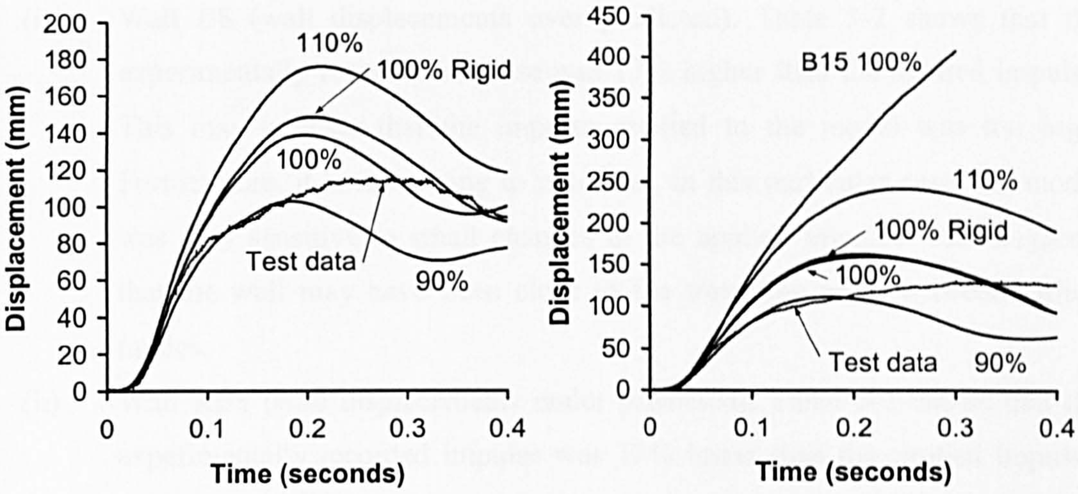

(a) Wall RB14*

(b) Wall RB15*

* Indicates displacement measured at top of wall, 360 mm from the centre of the point of impact

Figure 5-13 Displacement-time response for walls RB14-B15

5.4.6 Wall displacements

One of the main benefits of a three dimensional model is the ability to determine the out-of-plane displacement-time response of a wall and also to predict whether or not bricks are likely to be ejected. Therefore, the experimentally recorded displacement-time response has been compared with the model (Figure 5-12 and Figure 5-13).

When diagonal bar reinforcement was used surprisingly the displacement-time history was not significantly influenced by the chosen material model. Whichever model was chosen, diagonal bar reinforcement prevented bricks from being ejected (compare B15 with RB15). This suggests that interlock between individual units is more important than the properties of the reinforcing material.

In some cases the experimentally observed displacement was within the upper and lower bound limits. However, the experimentally recorded displacement was not within the upper and lower bound limits in the case of:

(i) Wall B8 (wall displacements over predicted). Table 5-2 shows that the experimentally recorded impulse was 17% higher than the applied impulse. This may indicate that the impulse applied to the model was too high. Furthermore, it is interesting to note that, in this particular case, the model was very sensitive to small changes in the applied impulse. This suggests that the wall may have been close to the transition point between failure modes.

(ii) Wall RB8 (wall displacements under predicted). Table 5-2 shows that the experimentally recorded impulse was 12% lower than the applied impulse. This may indicate that the impulse applied to the model was too low. Furthermore, horizontal shear planes were observed to form experimentally but this did not happen in the model.

(iii) Wall RB9 and RB11 (wall displacements over predicted). It is clear that the inclusion of vertical supports has a significant influence on wall response. The model assumption - that the supports were completely rigid - is probably unrealistic.

(iv) Wall RB10 (wall displacements grossly under predicted). Most of the impulse was dissipated by rocking. The exact proportion of the impulse giving rise to rocking and sliding modes is difficult to predict but it was shown in Chapter 4 that a number of key parameters are highly influential.

In the case of walls RB13, RB14 and RB15 the experimentally recorded displacement lay broadly between the upper and lower bound limits but the form of predicted displacement was different to that recorded experimentally. In all cases, the peak model displacement occurred before the experimentally recorded peak displacement.

5.4.7 Wall failure modes

Figure 5-4 shows experimentally observed and predicted crack patterns. Approximate characteristic failure lengths are summarised in Table 5-7. In some cases the model was able to predict the correct failure mode and characteristic length.

In the case of B8 the model predicted that diagonal fracture lines would form approximately 2.9 m from the point of impact. This compares with 3.1 m observed in the test. It is interesting to note that decreasing the impulse by 10% resulted in diagonal fracture lines forming 5.3 m from the point of impact (Figure 5-14). Conversely, when the impulse was increased by 10% the model predicted significant damage behind the point of impact (Figure 5-15).

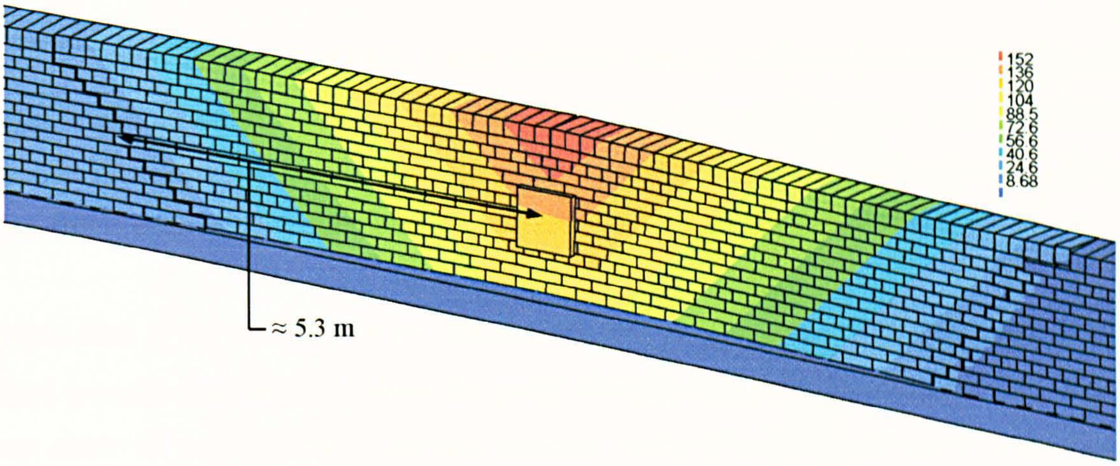

Wall B8 (90%): Time = 0.27 seconds, Displacement scale ×1

Figure 5-14 Wall B8: Out-of-plane displacement (mm)

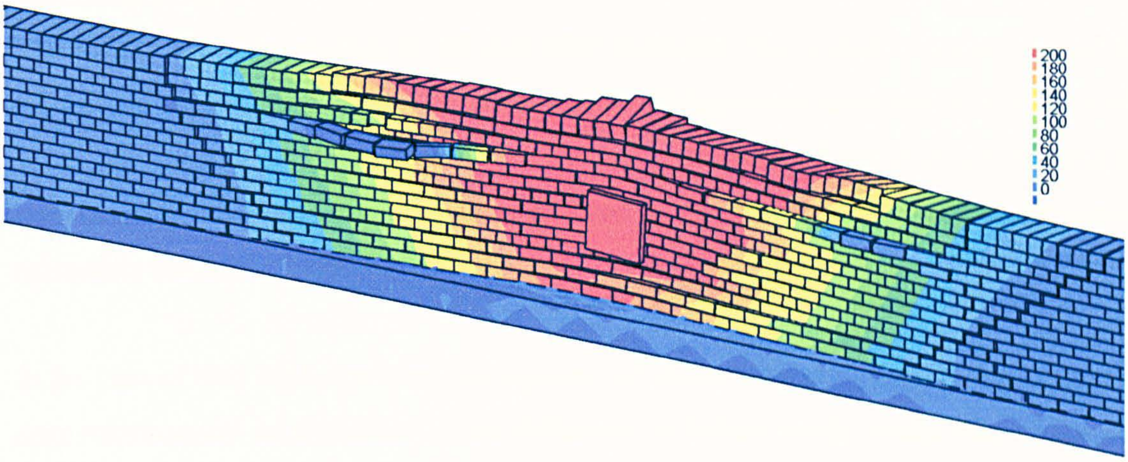

Wall B8 (110%): Time = 0.18 seconds, Displacement scale ×1

Figure 5-15 Wall B8: Out-of-plane displacement (mm)

In the case of the model of RB8, it was predicted that the wall would fracture behind the load with diagonal fracture lines also forming either side of the impact plate. A similar failure mode was observed experimentally but horizontal shear planes also formed in bed-joints containing reinforcement. This led to a much higher peak displacement.

In the case of the models of RB9, RB10 and RB11 it was predicted that the wall would form a single fracture line behind the point of impact. However, this failure mode was not observed experimentally. Instead, diagonal fracture lines formed either side of the point of impact and horizontal shear planes formed in bed-joints containing reinforcement.

In the case of models of RB13, RB14 and RB15 it was predicted that diagonal fracture lines would form either side of the point of impact. However, the diagonal cracks observed experimentally were more dispersed and occurred further away from the point of impact. In the case of B15 the model predicted that the wall would punch through behind the point of impact. This failure mode was observed experimentally.

5.5 Discussion

The results from the models of B8 and RB9 indicated that a small change in applied load could have a significant influence on the displacement-time response of a wall. When the models of B8 and RB9 were loaded with 90% of the impulse reasonable correlation between experimental and predicted displacements was obtained. However, increasing the applied load to 100% or 110% resulted in a large over prediction.

In the case of wall RB8, the large discrepancy between the model and test displacement-time response can be explained by the difference in failure mode. In the case of the test wall, horizontal shear planes formed in bed-joints containing reinforcement (Figure 5-16). This failure mode was not observed in the model (Figure 5-9b), which instead predicted the formation diagonal fracture lines either side of a central fracture line in the impact zone. Consequently, the model under predicted the magnitude of the ultimate displacement of the wall close to the load.

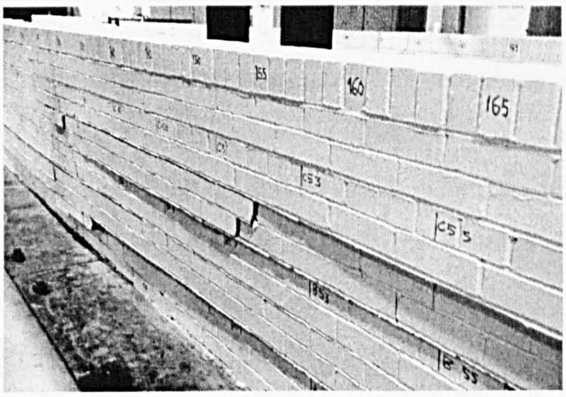

Figure 5-16 19.54 m reinforced wall (RB8) at mid-length behind the point of impact showing bed-joint sliding

Comparing the responses of walls RB9, RB10 and RB11 it is clear that the inclusion of vertical supports has a significant influence on wall response. The model assumption - that the supports were completely rigid - is probably unrealistic, and it seems quite likely that a closer match between the model and experimental responses could be obtained if the true support characteristics were used in the model.

Walls RB13, RB14 and RB15 showed that diagonal bar reinforcement prevented the formation of horizontal shear planes and increased moment resistance and ductility in the longitudinal direction. The models of these walls were able to approximately predict peak displacements and failure modes.

Walls RB15 and B15 showed that diagonal bar reinforcement significantly improved the performance of a weakly mortared wall. In the case of B15, there was substantial damage behind the point impact and bricks were ejected from the wall. In contrast, RB15 showed that diagonal bar reinforcement was effective in preventing individual bricks from being ejected.

5.6 Conclusions

(i) The extensive bed-joint cracking observed experimentally indicates that bed-joint reinforcement may not be particularly effective in improving the out-of-plane response of unreinforced walls.

(ii) From comparing the responses of walls RB9 and RB10 it is clear that the inclusion of vertical supports has a significant influence on wall response.

(iii) RB14 showed that the performance of FRP bars was comparable to high yield steel. However, FRP is likely to be more durable in the long term.

(iv) Diagonal bar reinforcement prevented the formation of horizontal shear planes and increased moment resistance and ductility in the longitudinal direction. Furthermore, diagonal bar reinforcement significantly improved the performance of weak mortared walls.

(v) Finite element models were able to predict the correct failure mode and approximate peak displacement for some but not all of the walls. Furthermore, in the case of B15 and RB15 the model correctly predicted that the inclusion of diagonal bar reinforcement prevented the wall from punching through behind the point of impact.

5.7 Acknowledgements

The support of EPSRC, under grant references GR/M43128, GR/M43135 and GR/M43142 is acknowledged. Also acknowledged is the support of Ove Arup and Partners, who provided LS-DYNA for development purposes during the project.

5.8 References

Beattie (2003); Joint fracture in reinforced and unreinforced masonry under quasi-static and dynamic loading; PhD thesis submitted to Liverpool University, UK.

BS 5628-1 (1992); Code of practice for use of masonry: Structural use of unreinforced masonry, BSI.

Giambanco G, Di Gati L (1997); A cohesive interface model for the structural mechanics of block masonry; Mechanics Research Communications, 24, 503-512.

Gilbert M, Hobbs B, Molyneaux TCK (2002a); The performance of unreinforced masonry walls subjected to low-velocity impacts: experiments; International Journal of Impact Engineering, 27, 231-251.

Gilbert M, Hobbs B, Molyneaux TCK (2002b); The performance of unreinforced masonry walls subjected to low-velocity impacts: mechanism analysis; International Journal of Impact Engineering, 27, 253-275.

Hallquist JO (1998); LS-DYNA User Manual; Livermore Software Technology Corporation.

Hallquist JO, Goudreau GL, Benson DJ (1985); Sliding Interfaces with Contact-Impact in Large Scale Langrangian Computations; Computer methods in applied mechanics and engineering, 51, 107-137.

Hamoush SA, McGinley MW, Mlakar P, Scott D, Murray K (2001); Out-of-plane strengthening of masonry walls with reinforced composites; Journal of Composites for Construction, Aug, 139-145.

Middleton WG (1994); Research Project into the Upgrading of Unreinforced Masonry Parapets; Bridge Assessment Management and Design; Ed. Barr, B.I.G. *et al.*, London, Elsevier, 229-234.

Rots JG (1997); Structural Masonry: An Experimental/Numerical Basis for Practical Design Rules; AA Balkema, Rotterdam, ISBN 90 5410 680 8.

Chapter Six

Discussion, conclusions and recommendations

6.1 Introduction

The aim of this chapter is to draw together work presented elsewhere in the thesis and to suggest how it may be used in future to benefit researchers and engineers alike. The first part of the chapter contains a general discussion of the work presented in Chapters Three, Four and Five. The second part of the chapter summarises the most important findings and the final part of the chapter contains specific recommendations for future work.

6.2 General discussion and application of results

6.2.1 Materials characterisation: performance of test rig

At the start of the project, it was decided to design and build a Split Hopkinson Pressure Bar (SHPB) to investigate the response of masonry joints subject dynamic tensile load. The Hopkinson Bar apparatus was chosen because it has been widely used to characterise materials at impact rates of strain and is generally accepted as a standard technique for dynamic testing.

The SHPB developed for use in the current project is similar to existing rigs but there are a few notable exceptions:

(i) Most SHPBs usually have a diameter between 20-50 mm compared with a diameter of 101.6 mm used here. The large bar diameter was particularly important in the current work because it enabled the rig to test specimens with variable cross-sectional properties. This is a relatively new research area because the SHPB apparatus was originally used to investigate the dynamic response of specimens with nominally uniform cross-sectional properties.

(ii) The overall length of the Sheffield SHPB is longer than most existing test rigs. Use of extended input and output bars allowed the rig to test specimens over a much longer duration say, 1 ms. This capability is relatively uncommon because the SHPB is typically used to test specimens over 200 μs or less.

In general, the overall performance of the test rig and data acquisition system was more than satisfactory. However, the hydraulic clamp mechanism needs to be improved such to enable it to release a wave with a much shorter rise time and higher peak stress. This will enable the rig to test specimens at both more constant and higher rates of strain. Even though there is room for some improvement, careful planning at the design stage allows the future performance of the rig to be extended to cover dynamic shear and compression testing. This means that the Sheffield rig has enormous potential for testing materials, subject to many different stress states, over durations that were previously unattainable using existing SHPBs.

6.2.2 Materials characterisation: results

Previous work carried out at Liverpool University and Sheffield University highlighted a lack of knowledge on the dynamic properties of masonry materials. Therefore, one of the main aims of the current collaborative project was to investigate the mechanical properties and rate sensitivity of the unit-mortar bond.

During the first collaborative project, a limited number of triplet specimens were tested at Liverpool University to investigate the shear properties of masonry joints. Results showed that, under dynamic loading conditions, shear bond strength could increase by a factor of 3 compared with the quasi-static value. These findings were confirmed by a much larger number of triplet specimens tested during the current collaborative project and should now form the basis of future work on masonry joints subject to dynamic shear load. One assertion is that the dynamic performance of triplet specimens is quite complex and a more accurate assessment of shear properties can be made using a SHPB.

For masonry joints subject to dynamic tensile loading no experimental work was carried out as part of the first collaborative project. Therefore, to the author's knowledge, the only test data in existence is that obtained from the SHPB work described in Chapter Three. Results showed that, under dynamic loading conditions, tensile bond strength could increase by a factor of 3 compared with the quasi-static value. Again, these findings should now form the basis of future work on masonry joints subject to dynamic tensile load

Chapter Three showed that the apparent dynamic enhancement of bond strength is probably caused by the inherent variability of the unit-mortar bond, and may not be a genuine material characteristic *per se*. This finding is particularly relevant in a dynamic masonry problem because the force required to fail a joint appears to be influenced by bond distribution. However, it is important to define what is meant by the term 'dynamic'. Many loading regimes are considered to be dynamic but it is the strain rate (or crack opening velocity) that is most important.

In the case of masonry parapets, a numerical model showed that the dynamic and quasi-static crack opening velocities were very similar. This implied that the joint interface model presented in Chapter Four could assume quasi-static failure properties and uniform bond stress. Even though it was not appropriate to use enhanced failure properties in the current work, results from the SHPB work are likely to be of interest to parties concerned with modelling masonry subject to blast loading. In this case, it is not uncommon to find that strain rates regularly exceed 1 s^{-1} i.e. the loading regime is similar to that used in the present SHPB tests.

The materials characterisation work carried out at Sheffield University and Liverpool University has made a major contribution to masonry research in general, but in particular, the field of masonry dynamics. Prior to work being carried out by the two universities, no evidence of published data on the dynamic properties of masonry joints could be found. This means that it is very difficult to make direct comparisons with other masonry research. However, data from quasi-static tests on masonry joints (Rots

1997, Pluijm 1997) and dynamic tests on concrete (Rossi & Toutlemonde 1996) suggest that findings presented here are a logical extension to current knowledge.

6.2.3 Material variability

It is well known that masonry is an extremely variable structural material. Thus, the question arises: is it possible to model a masonry structure using mean material properties? Chapter Four showed that reasonable results could be obtained using mean values of shear and tensile failure stress with a coefficient of variation of 27% or more. Therefore, the simple answer to the question appears to be yes. However, use of mean material properties is probably only appropriate when modelling large structures. The main reasoning behind this argument is that overall failure will result from the individual failure of large numbers of joints. This means that in a real masonry structure fracture lines are likely to form where the average applied stress exceeds the average failure stress in a group of joints i.e. micro-scale material variability becomes less important.

Material variability may be considered more important when planes of weakness are not predefined or when the applied stress is almost uniform. In practice, this may occur when modelling crack propagation in a homogeneous material (e.g. mortar) or modelling the overall response of a structure subject to shrinkage. For these cases, it is sometimes necessary to distribute strength and softening properties over a mesh using a standard normal or Weibull distribution (Rots 1997, Zhou & Molinari 2004). However, it is not usually necessary to apply a full scatter since one or two imperfections are likely to be sufficient (Rots 1997). Furthermore, it is worth noting that as soon as a change in geometry gives rise to a stress concentration, scatter and material imperfections become less important.

6.2.4 Modelling strategy: use of a masonry specific joint interface model

During the original collaborative project masonry parapets were modelled using an unmodified version of LS-DYNA which required use of artificially enhanced values of the limiting tensile and shear failure stresses. However, the standard interface model (Figure 6-1a) did not include joint dilatancy or fracture energy, which has been shown to significantly increase strength (Lourenço 1996). Therefore, one of the main aims of the work described in this thesis was to develop a masonry specific joint interface (i.e. include parameters such as dilatancy, fracture energy, Mohr-Coulomb shear criterion etc) which could be implemented in LS-DYNA (Figure 6-1b).

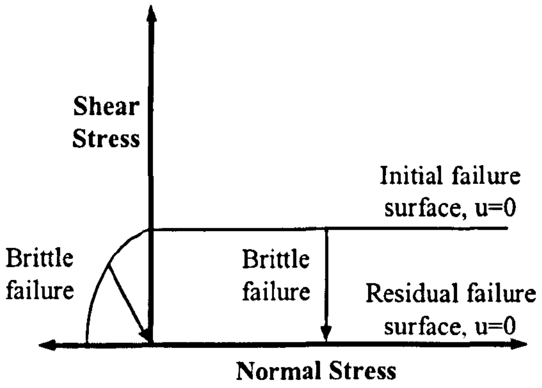

(a) Standard interface

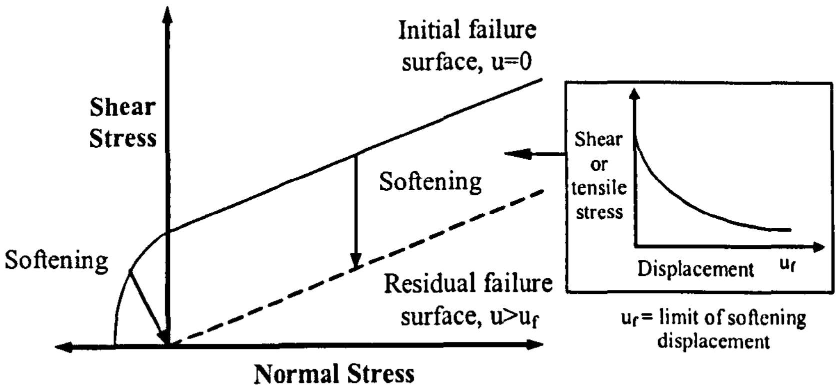

(b) Modified interface

Figure 6-1 Failure envelope for a masonry joint

The overall modelling strategy proposed in Chapter Four is similar to the simplified micro-model described by Rots (1997) who used an implicit solution strategy to model the quasi-static in-plane behaviour of masonry. However, it is important to note that the proposed joint interface model is implemented in an explicit finite element code and a penalty stiffness contact algorithm is used instead of explicit interface elements to model the behaviour of the joints.

To the author's knowledge, this is the first masonry specific interface model to be implemented in an explicit finite element code and therefore the first model that is able to predict the behaviour of masonry subject to impact loading. However, in the case of masonry parapets tested in the laboratory, it is probably more useful to note that reasonable results can be obtained using the proposed joint interface model with quasi-static interface properties. This is likely to be of particular interest to practicing engineers and other researchers because it means that in many cases it is possible to predict the dynamic behaviour of masonry structures without the need to carry out additional materials characterisation work at increased rates of strain.

6.2.5 Modelling strategy: results

Chapter Four showed the proposed modelling strategy was in general able to predict the dynamic response of full-scale unreinforced masonry walls with reasonable accuracy. However, a parametric study showed wall response was highly dependent on small changes in loading impulse, base friction, fracture energy, joint failure stress and angle of dilatancy.

If the results from the parametric study are applied to a model of an actual masonry parapet great care must be taken because the impact angle is likely to be much shallower say, 20°. This means that a greater proportion of the impact energy is resisted by: (i) the mass of the parapet and (ii) masonry joints acting in compression. Therefore, it is highly likely that out-of-plane response would become less sensitive to key masonry joint parameters.

Results from the parametric study also showed that the precise form of the applied impulse was highly influential. Therefore, a small change in the makeup of a vehicle could significantly affect the response of a parapet. For example, the applied impulse generated by a vehicle with its engine at the front is likely to be very different from a vehicle with its engine at the rear (because hard parts of a car, e.g. engine block, cause a sharp rise in the force-time history). This means that, in an actual vehicle impact, small variations in the type of vehicle may become more influential than key masonry joint parameters when assessing the performance of a wall or parapet.

Chapter Five showed that steel reinforcement improved the performance of a wall even when the bond between individual units was extremely weak. This suggests that a reinforced wall is not particularly sensitive to small changes in key interface parameters. Therefore, if the modelling strategy used to simulate reinforcement is improved, it should be possible to predict the behaviour of reinforced walls with greater consistency than unreinforced walls.

6.2.6 Application of modelling strategy to existing masonry structures

In the last 50 years, very few researchers have successfully studied the mechanical properties of masonry in-situ. Instead, much research has focused on laboratory testing of small-scale specimens and, more recently, the development of numerical models to predict the quasi-static and dynamic behaviour of structural masonry. However, it is important to note that the accuracy of any numerical model is highly dependent on the input parameters. This is especially true for masonry where it was demonstrated in Chapter Four that a small change in any one of four key input parameters has the potential to have a large influence on overall behaviour.

In many 'real world' engineering situations, a numerical model is used to predict the behaviour of a structure prior to construction. However, it is very uncommon for a new bridge or parapet to be constructed from masonry. Therefore, the main practical use of the numerical modelling work presented in this thesis is likely to be in assessing the structural integrity of existing masonry structures. At present, there are limitations in using a numerical model to assess existing masonry structures because it is extremely difficult to determine the exact mechanical properties of the unit-mortar bond in-situ. This is primarily due to the wide scatter of results obtained from a bond wrench test and the lack of non-destructive test methods.

If it can be shown that a numerical model of a masonry structure is not particularly sensitive to the input parameters (which may be the case for an actual vehicle impact) it might be possible to make a reasonably accurate structural assessment. However, if the laboratory impact test was repeated on an existing masonry parapet it is highly likely that there would be a large difference between the predicted and actual response due to the uncertainty of the unit-mortar properties. Therefore, it is essential that more research is undertaken to develop methods of assessing the mechanical properties of existing masonry structures in-situ.

6.3 Specific application of results

6.3.1 Materials characterisation

Materials characterisation work described in Chapter Three showed that masonry specimens exhibited an apparent dynamic increase factor of 3.1 when loaded at strain rates of approximately 1 s^{-1}. To the author's knowledge this is the first dynamic increase factor reported for masonry tensile test specimens. However, it is probably more important to note that the dynamic increase factor is likely to be influenced by non-uniform bond distribution. Therefore, when modelling the response of masonry joints at strain rates of approximately 1 s^{-1} or higher it is important to consider the influence of net bond area.

6.3.2 Numerical modelling: benefits to practicing engineers

At the end of a previous EPSRC collaborative research project, 'Impact resistance of masonry walls', the work was disseminated in the form of conference and journal papers, seminars etc. However, there was no direct input into BS 6779 pt 4: Highway parapets for bridges and other structures.

Most of the guidance given in BS 6779 pt 4 has been derived from a series of actual vehicle impact tests on full-scale masonry walls (Middleton 1994). In addition to the experimental work, numerical modelling was used to develop a range of vehicle containment charts. However, it is important to note that the modelling work was carried out using an unmodified version of LS-DYNA which required use of artificially enhanced values of the limiting tensile and shear failure stresses.

When BS 6779 pt 4 was published use of enhanced failure stresses were justified on the basis that an enhancement was observed experimentally when triplet specimens were loaded in less than 10 ms. However, the loading rate used in the triplet tests was higher than the loading rate used in the full-scale wall impact tests. Furthermore, another reason for having to use high strengths in the model was to compensate for the fully brittle constitutive model used at the joints. In light of work presented in this thesis and work by Beattie (2003), the use of numerical models with enhanced dynamic properties to simulate the performance of masonry bridge parapets is clearly inappropriate.

For the modelling work described in this thesis to be useful to a practicing bridge engineer it is essential to validate the proposed modelling strategy (incorporating fracture energy and dilatancy) against the full-scale wall impact tests carried out by the CSS as this may lead to the vehicle containment charts being revised. This is particularly important because a practicing engineer is unlikely to have the skills or time to construct a finite element model of a masonry wall or parapet.

6.3.3 Numerical modelling: benefits to other researchers

The modelling strategy described in Chapters Four and Five will be of major significance to other masonry researchers in the field of blast and impact engineering. Until now, researchers had to use rather crude 'enhanced' failure stresses to take account of post-peak softening behaviour in order to simulate the dynamic response of masonry structures. Incorporating fracture energy, dilatancy and a Mohr-Coulomb failure criterion into a masonry specific interface model means that this is no longer the case.

6.4 Conclusions

The work described in this thesis can be divided into two separate areas: materials characterisation and numerical modelling. For convenience, conclusions relating to each area have been grouped separately.

6.4.1 Materials characterisation

(i) A large diameter stored energy SHPB rig has been developed specially for use with masonry joints and other low strength quasi-brittle materials.

(ii) Brick specimens tested in tension at strain-rates of approximately 1 s^{-1} indicated an apparent dynamic enhancement of bond strength (DIF = 3.1). However, finite element modelling studies showed this effect is probably caused by the inherent variability at the unit-mortar bond, and is not a genuine material characteristic *per se*.

(iii) The form of the recorded post-peak softening branch was shown to be influenced by the dimensions of the specimen used when a SHPB is employed. Furthermore, a numerical model showed that the magnitude of the oscillations overwriting the softening branch was influenced by the rate at which a specimen failed.

6.4.2 Numerical modelling

(i) A masonry specific joint interface model has been successfully implemented in LS-DYNA.

(ii) In most cases, using the proposed modelling strategy allowed the dynamic response of a full-scale unreinforced masonry wall to be predicted with reasonable accuracy. In the case of reinforced walls, the proposed modelling strategy was able to predict that the inclusion of diagonal bar reinforcement would prevent punching failure. This finding is particularly important because one of the main objectives of the modelling work was to be able to predict if bricks were likely to be ejected from a wall.

(iii) A parametric study showed wall response was highly dependent on small changes in loading impulse, base friction, fracture energy, joint failure stress and angle of dilatancy.

6.4.3 General conclusions

(i) Numerical models showed that the overall response of an unreinforced masonry wall is highly dependent on small changes in key interface parameters. In a laboratory environment it is possible to determine the interface and material properties with reasonable accuracy. However, it is not uncommon to find that interface parameters vary by 30% or more (Rots 1997). In the field, it is highly unlikely that precise masonry properties will be known for an existing wall or parapet. Furthermore, current field tests (e.g. bond wrench test) are not particularly accurate. Therefore, great care should be taken when attempting to model existing masonry walls and parapets.

(ii) The apparent sensitivity of the model increases dramatically close to the transition point between different failure mechanisms. For example, if a wall is perfectly balanced between rocking over completely and rocking back towards its original position a small, say 1% change in any of the input parameters will appear to have a significant influence on the overall response. The same logic can be applied to the formation of fracture lines. Therefore, care should be taken when assessing the influence of both the numerical and experimentally derived input parameters.

6.5 Recommendations for future work

Whilst much of the work presented in this thesis has been successful, in some areas the author believes that the work could be improved or extended. For convenience, recommendations have been grouped according to the area of work:

6.5.1 Materials characterisation

(i) Improve the rise time and shape of the loading pulse by firstly constructing a numerical model of the clamp mechanism.

(ii) Develop the rig such that it can also be used to subject specimens to dynamic shear stresses.

(iii) Test specimens at strain rates above 1 s^{-1} to investigate whether or not the dynamic increase factor increases.

(iv) Investigate experimentally the influence of variable bond failure stress at the unit-mortar interface (numerical work suggested that bond area had a significant influence on the dynamic increase factor).

(v) Test masonry specimens with much smaller thicknesses (e.g. <10 mm). This will increase strain rate at peak failure and increase the frequency of the post-peak oscillations overwriting the softening branch. If the frequency of the oscillations increases it will be easier to filter out unwanted frequency components from the underlying trend.

6.5.2 Numerical modelling

(i) Validate the proposed modelling strategy against actual vehicle impact tests carried out by the CSS. This is important in order to improve the vehicle containment charts proposed in BS 6779 pt 4.

(ii) Improve the interface model to allow for variable joint dilatancy and increased fracture energy with increasing normal compression.

(iii) At present, the post-peak softening response of the reinforcement-brick interface is assumed to be the same as the brick-mortar interface. Therefore, the model response may be improved by allocating separate post-peak failure parameters to the reinforcement-brick interface.

(iv) In the proposed modelling strategy physical bricks are assumed to be elastic and 'plastic' deformation is confined to the masonry specific joint interface. The interface formulation may therefore be improved by allowing for joint crushing in the interface.

6.6 References

Beattie (2003); Joint fracture in reinforced and unreinforced masonry under quasi-static and dynamic loading; PhD thesis submitted to Liverpool University, UK.

BS 6779 pt 4 (1999); Highway parapets for bridges and other structures: specification for parapets of reinforced and unreinforced masonry construction, BSI, ISBN 0580282910.

Lourenço PB (1996); Computational Strategies for Masonry Structures, Delft University Press, ISBN 90 407 1221 2.

Middleton WG (1994); Research project into the upgrading of unreinforced masonry parapets; Bridge Assessment Management and Design; Ed. Barr, B.I.G. *et al.*, London, Elsevier, 229-234.

Rossi P, Toutlemonde F (1996); Effect of loading rate on the tensile behaviour of concrete: description of the physical mechanisms; Materials and Structures, 29, 116-118.

Rots JG (1997); Structural Masonry: An experimental/numerical basis for practical design rules; AA Balkema, Rotterdam, ISBN 90 5410 680 8.

Zhou F, Molinari JF (2004); Dynamic crack propagation with cohesive elements: a methodology to address mesh dependency; International Journal for Numerical Methods in Engineering, 59, 1-24.